

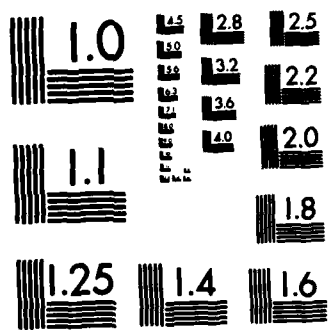
CERAMIC MICROSTRUCTURE DEVELOPMENT(U) OHIO STATE UNIV  
COLUMBUS DEPT OF CERAMIC ENGINEERING D W READEY AUG 84  
N00014-80-C-0523

1/2

F/G 11/2

NL

A 10x10 grid of 100 squares. The grid is mostly black, with some white squares and small white rectangular marks scattered throughout. The marks are located at various positions, including (row, column) coordinates: (1, 1), (1, 4), (1, 9), (2, 1), (2, 5), (2, 9), (3, 7), (4, 2), (4, 8), (5, 9), (6, 9), (7, 4), (8, 9), (9, 5), and (9, 9). The marks are small white rectangles of varying sizes and orientations.



MICROCOPY RESOLUTION TEST CHART

12

AD-A145 753

RF Project 762134/712823  
Final Report

CERAMIC MICROSTRUCTURE DEVELOPMENT

D. W. Readey  
Department of Ceramic Engineering

For the Period  
April 1, 1980 - December 31, 1982

DEPARTMENT OF THE NAVY  
Office of Naval Research  
Arlington, Virginia 22217

Contract No. N00014-80-C-0523

DTIC  
ELECTE  
SEP 21 1984  
B

August, 1984

**DISTRIBUTION STATEMENT A**

Approved for public release  
Distribution Unlimited

Reproduction in whole or in part is permitted for any purpose by  
the United States Government.

OSU

**The Ohio State University  
Research Foundation**  
1314 Kinnear Road  
Columbus, Ohio 43212

DTIC FILE COPY

84 9 18 266

REPORT DOCUMENTATION PAGE		READ INSTRUCTIONS BEFORE COMPLETING FORM
1. REPORT NUMBER	2. GOVT ACCESSION NO. <i>AD-A145753</i>	3. RECIPIENT'S CATALOG NUMBER
4. TITLE (and Subtitle)  CERAMIC MICROSTRUCTURE DEVELOPMENT		5. TYPE OF REPORT & PERIOD COVERED Final Report 4/1/80-12/31/82
7. AUTHOR(s)  Dennis W. Readey		6. PERFORMING ORG. REPORT NUMBER 762134/712823
9. PERFORMING ORGANIZATION NAME AND ADDRESS The Ohio State University Research Foundation, 1314 Kinnear Road Columbus, Ohio 43212		8. CONTRACT OR GRANT NUMBER(s)  N00014-80-C-0523
11. CONTROLLING OFFICE NAME AND ADDRESS Department of the Navy Office of Naval Research Arlington, Virginia 22217		10. PROGRAM ELEMENT, PROJECT, TASK AREA & WORK UNIT NUMBERS  NR032-602/3-2480 471
14. MONITORING AGENCY NAME & ADDRESS (if different from Controlling Office)		12. REPORT DATE August 1984
		13. NUMBER OF PAGES 138
		15. SECURITY CLASS. (of this report) Unclassified
		15a. DECLASSIFICATION/DOWNGRADING SCHEDULE
16. DISTRIBUTION STATEMENT (of this Report)  Approved for public release; distribution unlimited.		
17. DISTRIBUTION STATEMENT (of the abstract entered in Block 20, if different from Report)		
18. SUPPLEMENTARY NOTES		
19. KEY WORDS (Continue on reverse side if necessary and identify by block number)  ceramics, processing, sintering, grain growth, vapor transport  <i>↳ This research sought</i>		
20. ABSTRACT (Continue on reverse side if necessary and identify by block number) The goal of this research was to gain some fundamental understanding about the preparation, consolidation, and sintering of ceramic powder compacts. <sup>(1)</sup> Specifically, the research covered preparation of powders by vapor phase hydrolysis, molten salt oxidation and decomposition, and controlled precipitation from urea solutions. Consolidation by centrifugal casting was investigated. The major work entailed the investigation of vapor (continued)		

Block 20 (Abstract) - Continued

transport on microstructure development in porous powder compacts.

→ Nickel oxide powders were prepared by vapor phase hydrolysis of nickel chloride. The process is controlled by nucleation and growth of the powder particles in the gas phase and results in small, about one micrometer, nonagglomerated powders with narrow size distributions.

The oxidation and decomposition of molten salts were investigated briefly as alternative methods of producing binary oxide powders. Nickel chloride dissolved in alkali chloride melts was oxidized and nickel nitrate in alkali nitrate melts was decomposed. In both cases, agglomerated oxide powders were produced largely due to the fact that the reaction occurred either at the atmosphere-melt or melt-crucible interface.

Nickel oxide powders were prepared by precipitation of nickel hydroxide by slow decomposition of urea solutions. This resulted in small, largely nonagglomerated, spherical hydroxide particles which could be calcined to less than one micrometer oxide particles. The solution concentrations and temperature of precipitation mainly affected the morphology of the precipitate particles and not the particle size or the particle size distribution.

Centrifugal casting of silica, alumina, zinc oxide, and tin oxide was investigated. In general, it was found that centrifugal casting did not result in a higher green density as reported in the literature and there was little correlation with the degree of deflocculation of the suspensions and the packing density. These results were presented in an earlier report and are not presented again in this report.

(HCP)  
The major part of the research was focused on the effect of vapor transport on microstructure development in porous powder compacts. The sintering of  $\text{Fe}_2\text{O}_3$  in  $\text{HCl}$ , and  $\text{ZnO}$ ,  $\text{CdO}$ , and  $\text{SnO}_2$  in hydrogen was studied. These systems were chosen because of the high vapor pressures of the product gases which could be achieved. In all cases, sintering was retarded even to the point of zero densification as predicted from sintering models. However, the main microstructural feature produced by enhanced vapor transport is coarsening of the microstructure in general. It was concluded that in most cases, grain boundary motion controlled particle coarsening. This is an important result in that it implies that grain growth must be controlled during all stages of densification and not merely during the final stage in order to control microstructure development.

**CERAMIC MICROSTRUCTURE DEVELOPMENT**

**Department of Ceramic Engineering  
The Ohio State University  
Columbus, Ohio 43210**

**Final Report  
on  
Contract  
N00014-80-C-0523**

**April 1, 1980 to December 31, 1982**

**D. W. Readey  
Principal Investigator**

**August, 1984**



Accession For	
NTIS GRA&I	<input checked="checked" type="checkbox"/>
DTIC TAB	<input type="checkbox"/>
Unannounced	<input type="checkbox"/>
Justification	
By _____	
Distribution/	
Availability Codes	
Dist	Avail and/or Special
A-1	

## TABLE OF CONTENTS

	<u>PAGE</u>
1. INTRODUCTION	1-1
1.1 Processing, Structure, and Properties	1-1
1.2 Ceramic Versus Metal Processing	1-2
1.3 Powder Processing of Ceramics	1-3
1.4 Scope of This Research	1-6
1.5 References	1-7
2. NICKEL OXIDE POWDERS BY VAPOR PHASE HYDROLYSIS OF NICKEL CHLORIDE	2-1
2.1 Introduction	2-1
2.2 Vapor Phase Hydrolysis	2-1
2.3 Experimental	2-4
2.3.1 Apparatus	2-4
2.3.2 Nickel chloride preparation	2-6
2.3.3 Powder characterization	2-6
2.4 Results	2-7
2.5 Discussion and Conclusions	2-9
2.6 References	2-14
3. PREPARATION OF NICKEL OXIDE POWDERS BY REACTIONS IN MOLTEN SALTS	3-1
3.1 Introduction	3-1
3.2 Other Potential Molten Salt Powder Preparation Methods	3-3
3.3 Experimental	3-4
3.4 Results and Discussion	3-5
3.5 Conclusions	3-7
3.6 References	3-7
4. CONTROLLED PRECIPITATION OF NICKEL OXIDE POWDERS	4-1
4.1 Introduction	4-1
4.2 Experimental	4-3
4.3 Results and Discussion	4-3
4.3.1 Precipitate morphologies	4-3
4.3.2 Particle size	4-8
4.3.3 Calcining	4-8
4.3.4 X-ray data	4-8
4.4 Conclusions	4-14
4.5 References	4-14
5.0 VAPOR TRANSPORT AND SINTERING OF CERAMICS: THEORY	5-1
5.1 Introduction	5-1
5.2 Vapor Transport and Densification	5-1
5.2.1 Observations and importance	5-1
5.2.2 Vapor transport and sintering models	5-3
5.2.3 Vapor transport and volume diffusion	5-6

5.2.4	Vapor transport and atmospheres	5-8
5.2.5	Impurities and vapor transport	5-10
5.2.6	Vapor transport and particle coarsening	5-11
5.3	Vapor Transport in Multicomponent Systems	5-11
5.3.1	Introduction	5-11
5.3.2	Solid solution	5-12
5.3.3	Multiphase system	5-13
5.4	Vapor Transport and Third Stage Grain Growth	5-16
5.5	References	5-21
6.0	MICROSTRUCTURE DEVELOPMENT OF $\text{Fe}_2\text{O}_3$ IN HCL VAPOR	6-1
6.1	Introduction	6-1
6.2	Experimental	6-2
6.3	Results and Discussion	6-4
6.3.1	Early stage microstructure development	6-4
6.3.2	Final stage sintering	6-11
6.4	Summary and Conclusions	6-15
6.5	References	6-16
7.0	MICROSTRUCTURE DEVELOPMENT OF ZnO IN HYDROGEN	7-1
7.1	Introduction	7-1
7.2	Experimental	7-2
7.2.1	Powder preparation	7-2
7.2.2	Sample preparation	7-5
7.2.3	Sintering and microstructure analysis	7-6
7.3	Results and Discussion	7-6
7.3.1	General	7-6
7.3.2	Rate of particle growth	7-7
7.3.3	Grain growth in dense zinc oxide in air	7-13
7.3.4	Effect of alumina on coarsening	7-18
7.4	Conclusions	7-21
7.5	References	7-27
8.0	MICROSTRUCTURE EVOLUTION IN $\text{SnO}_2$ AND CdO IN REDUCING ATMOSPHERES	8-1
8.1	Introduction	8-1
8.2	Experimental	8-1
8.3	Results and Discussion	8-2
8.3.1	Cadmium oxide	8-2
8.3.2	Tin oxide	8-8
8.4	Conclusions	8-10
8.5	References	8-12



## SUMMARY

This report summarizes the research performed over a about a two and one half year period on the powder processing of oxide ceramics. The immediate goal of this research was not to produce powders or sintering techniques which would lead immediately to improved densification of crystalline ceramic powders. Rather, the goal was to gain some fundamental understanding about the preparation, consolidation, and sintering of ceramic powder compacts. Specifically, the research covered preparation of powders by vapor phase hydrolysis, molten salt oxidation and decomposition, and controlled precipitation from urea solutions. Consolidation by centrifugal casting was investigated. The major part of this work entailed the investigation of vapor phase transport on microstructure development in porous powder compacts. The most significant results are described briefly below and discussed in detail in the body of the report.

Nickel oxide powders were prepared by vapor phase hydrolysis of nickel chloride. The process is controlled by nucleation and growth of the powder particles in the gas phase and results in small, about one micrometer, nonagglomerated powders with narrow size distributions. These results suggest that vapor phase reactions such as this are ideal for the formation of binary oxide and other ceramic powders in a form most desirable for subsequent consolidation and densification.

The oxidation and decomposition of molten salts were investigated briefly as alternative methods of producing binary oxide powders. Nickel chloride dissolved in alkali chloride melts was oxidized and nickel nitrate in alkali nitrate melts was decomposed. In both cases, agglomerated oxide powders were produced largely due to the fact that the reaction occurred either at the atmosphere-melt or melt-crucible interface. As a result, the study of molten salt preparation was terminated when the results of the vapor phase hydrolysis appeared more promising in that the process was more amenable to control and analysis.

Nickel oxide powders were prepared by precipitation of nickel hydroxide by slow decomposition of urea solutions. This resulted in small, largely nonagglomerated, spherical hydroxide particles which could be calcined to less than one micrometer oxide particles. The solution concentrations and temperature of precipitation mainly affected the morphology of the precipitate particles and not the particle size or the particle size distribution.

Centrifugal casting of silica, alumina, zinc oxide, and tin oxide was investigated. In general, it was found that centrifugal casting did not result in a higher green density as reported in the literature and there was little correlation with the degree of deflocculation of the suspensions and the packing density. These results were presented in an earlier report and are not presented again in this report.

The major part of the research was focused on the effect of vapor transport on microstructure development in porous powder compacts. The sintering of  $\text{Fe}_2\text{O}_3$  in  $\text{HCl}$ , and  $\text{ZnO}$ ,  $\text{CdO}$ , and  $\text{SnO}_2$  in hydrogen was studied. These systems were chosen because of the high vapor pressures of the product gases which could be achieved. In all cases, sintering was retarded even to the point of zero densification as predicted from sintering models. However, the main microstructural feature produced by enhanced vapor transport is coarsening of the microstructure in general. This coarsening follows a one third time dependence as predicted by classical theories of coarsening by diffusion in the surrounding fluid phase. However, the temperature dependence and the particle size distributions usually observed did not fit the theoretical coarsening models. It was concluded that in most cases, grain boundary motion controlled particle coarsening. In fact, in zinc oxide doped with  $\text{ZnAl}_2\text{O}_4$  second phase particles, the rate of coarsening was decreased as would be expected from the impeding of grain boundaries by the second phase. This is an important result in that it implies that grain growth must be controlled during all stages of densification and not merely during the final stage in order to control microstructure development.

## 1. INTRODUCTION

### 1.1 Processing, Structure, and Properties

The goal of materials science research is the development of a scientific understanding of the processes and properties of materials so that they may be tailored to satisfy a particular application or need. Properties are determined not only by the structure on an atomic and crystal lattice scale, but also by the microstructure, the realization and understanding of which has lead to the development and improvement of so many materials during this century. The interrelationships between the processing, structure (atomic, crystal, and micro), and properties is central to materials science. Over the last twenty years a great deal of emphasis has been placed on, and great deal of progress has been made in, understanding the relation between the structure and properties of materials. This is particularly true for ceramics. However, one of the main limitations to the more widespread application of ceramics has been their lack of reproducible properties. Admittedly, the properties of ceramics are far less well understood than those of metals. Nevertheless, comparatively speaking, the relations between structure and properties of ceramics are far better understood than the processes that control microstructure development and the variables affecting them. Given a specific ceramic material, one cannot design a series of processing steps that will guarantee the desired microstructure and resulting properties. We simply

do not understand the fundamental processes sufficiently well to provide this degree of material predictability.

## 1.2 Ceramic Versus Metal Processing

There is also a significant difference in the important processing steps between metals and ceramics. Most of the microstructure development and control which are used to vary properties in metallic systems occur during post-consolidation thermal and mechanical treatments such as recrystallization and precipitation. The fact that such treatments have not been utilized as widely with ceramic materials partly reflects the fact that ceramics, being more brittle, do not lend themselves to mechanical treatments and, to a lesser degree, the more limited solid solution in ceramic systems. The main reason however, is that such treatments are of little utility if the property-determining microstructure is developed during the consolidation process as is usually the case in ceramics. For example, a great deal of effort is underway in trying to increase the work of fracture of ceramics by transformational toughening<sup>1</sup> and microcracking<sup>2</sup>. Nevertheless, if the fracture strength of such materials is determined by large random processing flaws, even though the average strength is increased by toughening, the sample to sample variation will still make the systems designer reluctant to utilize the material. Therefore, an improved understanding of ceramic microstructure development is the most critical area which will lead to new, improved, and more widespread use of high technology ceramics.

Powder technology is the traditional method of ceramic materials production and will continue to be in the future because of the wide variety of materials which can be fabricated and the control that exists over microstructure development. Therefore, powder processing is far more important for fabricating ceramics than metals since only a small fraction of metals are fabricated by powder metallurgical techniques. This then emphasizes the interest by ceramists in powder and particulate science and the understanding of mass transport and chemical effects during sintering. They are central to ceramic microstructure development but only of limited specialized interest to metallurgists. Therefore, the ceramist cannot simply transfer a vast body of knowledge and expertise from the metallurgists for powder processing as has been done for the understanding of mechanical properties. In the area of powder processing and microstructure development through sintering, ceramic science must lead.

### 1.3 Powder Processing of Ceramics

The goal of the ceramic engineer, given the task of producing a specific ceramic material, is to be able to start with a powder such as shown in Figure 1.1, and sinter to essentially theoretical density with a controlled grain size as shown in Figure 1.2. If he or she can do this, than intermediate densities and microstructures are possible. This research focusses on microstructure development in single phase materials such as

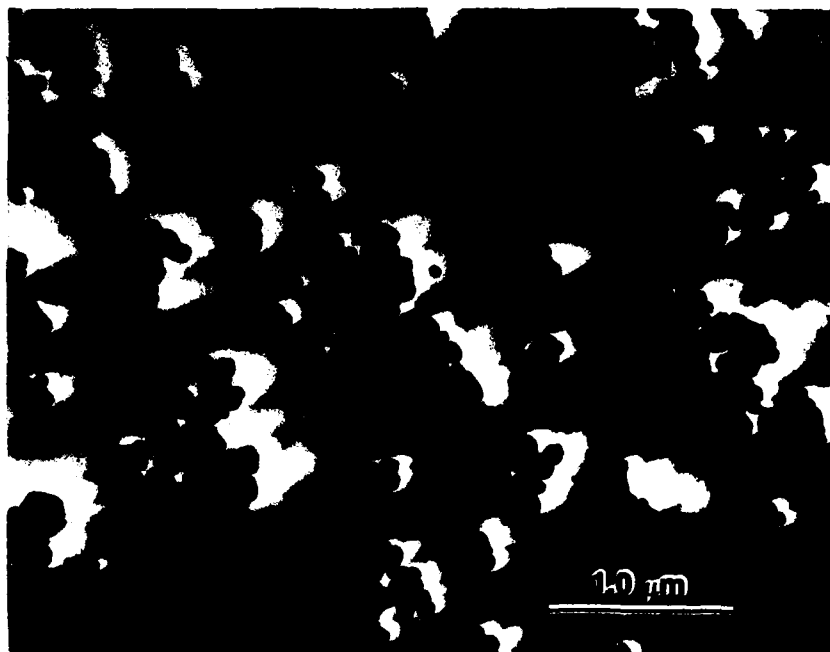


Figure 1.1 Typical ceramic starting powder. Commercial titanium dioxide,  $\text{TiO}_2$ .

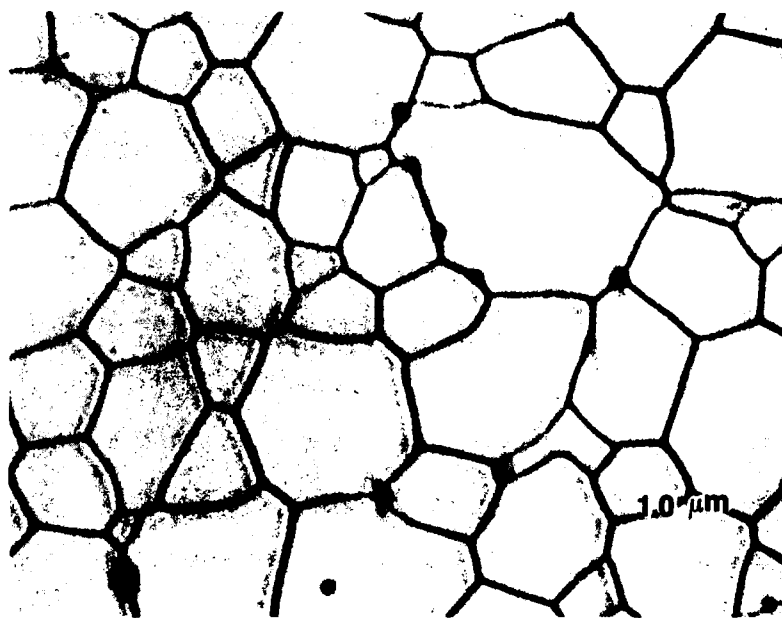


Figure 1.2 High density sintered yttrium iron garnet, thermally etched.

shown in Figure 1.2 in which densification was produced entirely by solid state diffusion processes. In other words, multiphase materials, liquid phase sintering, and vitrification were not considered. Many of the high technology ceramic materials are of this type.

The current understanding of ceramic powder processing has led to the following description of the desired powder and transport processes which lead to high density<sup>3</sup>:

1. small, nonagglomerated, monodispersed spherical powders;
2. uniform, dense(close-packed) packing of powder;
3. mass transport during sintering by volume or grain boundary diffusion, no transport by surface diffusion or vaporization and condensation;
4. fire in an atmosphere of rapidly diffusing gas such as hydrogen or oxygen and avoid nitrogen, argon, etc.

Usually, one and frequently all of these requirements are not satisfied in practice. There is a great deal of research in progress today attempting to produce ideal powders by many processes<sup>4-10</sup>. Unfortunately, many ceramic engineers are placing false hopes on new powders expecting their development and availability to solve all of their processing problems. That simply is not the case! Poor materials can and will be made with ideal powders just as many excellent materials such as illustrated by the magnetic garnet material in Figure 1.2 have been made for years with presumably poor powders. There are many important processing steps and variables which must be controlled



between the powder preparation step and the final fired microstructure.

#### 1.4 Scope of This Research

In order to develop a complete understanding of microstructure development it is critically important to investigate and understand the role each stage of the processing has on ensuing steps to ensure that the principles are being followed. The plea for characterization of ceramic powders is frequently heard and is certainly valid. However, characterization without a clear correlation between the variables characterized and microstructure developed is simply a waste of time. Since densification behavior is the best test of powder characteristics, packing, and morphology evolution<sup>11</sup>, studies of ceramic processing from particle preparation, characterization, and packing up through the final stages of sintering and grain growth should be performed. It was the purpose of this research program to investigate certain aspects of all the steps in ceramic processing. The specific intent was to not attempt to optimize the processing for a specific material nor to develop commercially-viable techniques. Rather, the purpose was to investigate certain powder preparation processes, to investigate powder packing by centrifugal casting, and to investigate processes thought to inhibit densification. This latter somewhat negative approach is justified on the basis that since we do not completely understand those factors which inhibit

microstructure development it is hard to eliminate them. Part of the goal of the research then was to delineate the importance of the deviation from the ideal on microstructure development.

Specifically the research included:

1. powder preparation by molten salt hydrolysis, vapor phase hydrolysis, and by controlled precipitation;
2. investigation of centrifugal casting as a consolidation technique (the results of this research were presented in an earlier report<sup>12</sup> and will not be reported on here);
3. the effect of vapor transport on densification kinetics and microstructure development of ceramic powder compacts.

#### 1.5 References

1. D. L. Porter and A. H. Heuer, J. Am. Ceram. Soc. 62 298 (1979).
2. D. J. Green, J. Am. Ceram. Soc. 65 610 (1982).
3. R. L. Coble and R. M. Cannon, p. 291 in Vol. 11 of Materials Science Research Processing of Crystalline Ceramics, (Plenum, N. Y.), 1978.
4. S. P. Mukherjee, Non-Crystalline Solids 42 477 (1980).
5. Eric A. Barringer and H. Kent Bowen, J. Am. Ceram. Soc. 65 C-199 (1982).
6. T. Yamaguchi, et al., J. Mat. Sci. 15 1491 (1980).
7. V. Suyama and A. Kato, J. Am. Ceram. Soc. 59 146 (1976).
8. V. Suyama, T. Mizobe, and A. Kato, Ceram. Int. 3 141 (1977).

9. Y. Ando and R. Uijeda, J. Am Ceram. Soc. 64 C-12 (1981).
10. Y. Suzawa, et al., Ceram. Int. 5 84 (1980).
11. W. D. Kingery, p. 291 of Ceramic Processing Before Firing, G. Y. Onoda, Jr., and L. L. Hench, eds., (John Wiley and Sons, N. Y.), 1978.
12. G. W. Shaffer and D. W. Readey, "Packing of Oxide Ceramic Powders by Centrifugal Casting," Report No. 76134/712823 on Contract No. N00014-80-C-0523, Sept. 1982.

## 2. NICKEL OXIDE POWDERS BY VAPOR PHASE HYDROLYSIS OF NICKEL CHLORIDE

### 2.1 Introduction

Powder characteristics profoundly affect the microstructure developed in ceramics. This is especially true in traditional powder processing involving solid state reactions of precursor materials to produce the desired oxide or nonoxide powders. During the calcination process the individual crystallites sinter together forming hard agglomerates as shown in Figure 2.1. Ball milling or some other comminution process is commonly employed to break up these large agglomerates. However, agglomerates frequently remain and a wide particle size distribution results. During later consolidation processes the agglomerate structure is retained, resulting in large and irregular pores which are difficult if not impossible to remove. In addition, the agglomerates themselves may densify during sintering resulting in discontinuous grain growth or large lenticular voids caused by the agglomerates pulling away from the matrix<sup>1</sup>. Therefore, the elimination of agglomerates by utilizing powder preparation methods that produce agglomerate-free powders can improve the final microstructure of ceramic materials.

### 2.2 Vapor Phase Hydrolysis

Vapor phase reactions have been employed in the production of fine powders in the past. There are many techniques employing vapor phase reactions such as arc vaporization<sup>2</sup>, electron beam

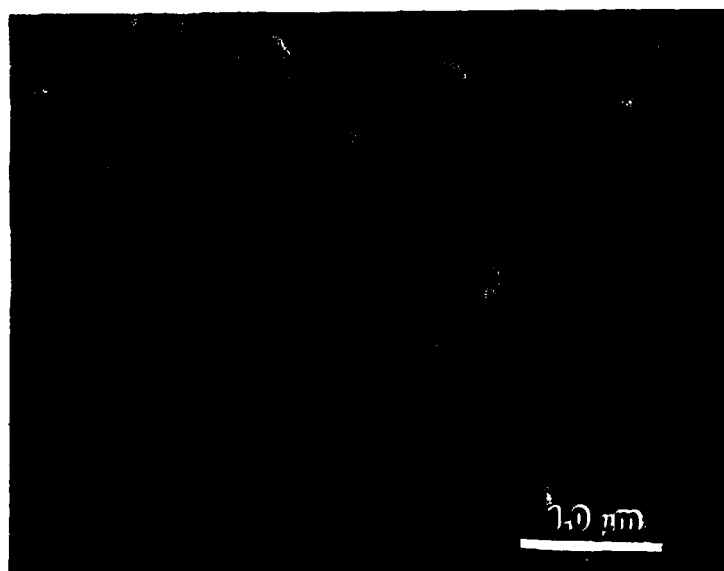


Figure 2.1 Hard agglomerates of NiO produced by calcination of nickel sulphate.

evaporation<sup>3</sup>, plasma evaporation<sup>4</sup>, flame hydrolysis<sup>5</sup>, and conventional vapor phase reactions. Most of these processes result in particle sizes less than 0.1 micrometers. There are many patents on the manufacture of titanium dioxide and silica utilizing a vapor phase reaction. Although the thermodynamics involved in producing powders by vapor phase reactions are simple, the kinetics of the process are not well understood. The effects of reactant and product gas partial pressures, supersaturation, and reaction temperature on particle morphology are not well documented or understood as well. Kato and coworkers have studied titanium dioxide produced by the oxygenolysis of titanium tetrachloride<sup>6</sup>. The resulting powders were predominately square or polyhedral. Average particle sizes ranged from 0.05 to 0.75 micrometers. It is interesting to note that titanium dioxide powders described in various patents are reputed to be spherical. The powders produced by Kato in the oxygenolysis of zirconium tetrachloride range from spherical to plate-like to polyhedral<sup>7</sup>. The average particle size ranged from 0.1 to 0.5 micrometers. Both particle size and morphology varied depending upon the reaction temperature and concentration of reacting gases. Similar results are also reported by Kato on the formation of silica by the oxygenolysis of silicon tetrachloride<sup>8</sup> and the formation of alumina by the oxygenolysis of aluminum tribromide<sup>9</sup>.

It is difficult to adequately quantify the effects individual gas partial pressures, supersaturation, and reaction

temperature have on growth rates, nucleation rates or morphology. This is due to the fact that by changing the concentration of any individual gas species, the supersaturation is simultaneously changed. Also, there is no model to predict the change in nucleation rate or growth rate with changes in individual gas concentrations. It is the purpose of this research: to investigate the vapor phase hydrolysis of a metal chloride gas to form oxide powders; to characterize those powders in terms of their particle size, size distribution, and morphology or habit; to determine the effects that the experimental variables have on the powder characteristics; and to attempt to develop a model of the process. Nickel chloride hydrolysis to nickel oxide by water vapor was the system studied since nickel oxide is a frequently used model oxide and the temperatures and partial pressures are in an easily accessible range. Specifically, the reaction studied is:



and the variables are the chloride and water vapor pressures, the reaction temperature, and the gas flow rate.

## 2.3 Experimental

### 2.3.1 Apparatus

The experimental apparatus consists of a tubular furnace with two independently controlled hot zones as sketched in Figure 2.2. One hot zone is used for the generation of the desired

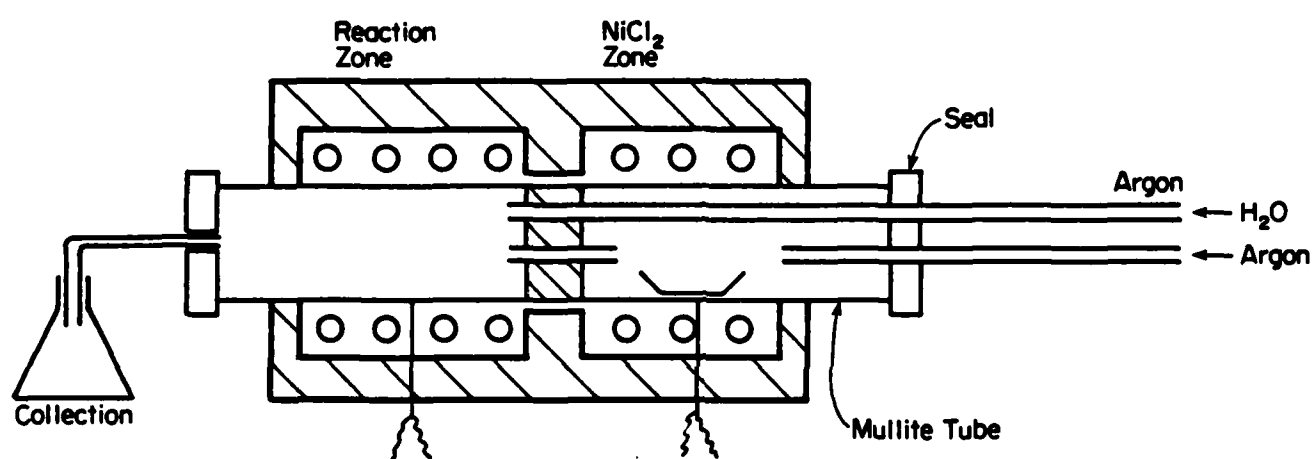


Figure 2.2 Schematic diagram of the reaction furnace.



partial pressure of nickel chloride. The other hot zone is the reaction zone. The sublimed nickel chloride is carried by argon gas and mixed with  $H_2O$  vapor in the reaction zone. The argon carrier gas is passed through a drying column before entering the nickel chloride generator. The desired partial pressure of  $H_2O$  is generated by passing argon gas through water at a prescribed temperature. Flow meters are used to control the velocity of gases through the furnace. The product powders are collected in a flask filled with water at the exit end of the furnace.

### 2.3.2 Nickel chloride preparation

Baker reagent grade nickel chloride hexahydrate was dehydrated for use in the production of nickel chloride gas. A differential thermal analysis was performed on the hydrated material to find the minimum temperature required to drive off all of the chemical water. The DTA run indicated that the chemical water was driven off in multiple stages with the last remnants of water leaving at  $265^{\circ}C$ . The dehydration was performed in pyrex crucibles at the prescribed temperature. The anhydrous nickel chloride was then stored in a dessicator until needed.

### 2.3.3 Powder characterization

The nickel oxide powders collected from each run were repeatedly washed with double distilled deionized water. The final washing cycle was done in methanol. For each washing cycle the nickel oxide powder was ultrasonically dispersed and then centrifuged. The supernatant liquid was then decanted and the washing cycle repeated. Five washing cycles were performed on

each powder.

A small amount of the washed powder was withdrawn and further dilluted with methanol until a slightly cloudy suspension was evident. The suspensions were ultrasonically dispersed for two minutes. One drop of the suspension was withdrawn with an eyedropper and deposited on an aluminum sample stub for scanning electron microscope analysis. Another drop of the suspension was also withdrawn and placed on a carbon-coated support grid for transmission electron microscope analysis.

Electron micrographs were made at various magnifications depending on the particle size. All magnifications were 700x, 1000x, or 2000x. Three or four micrographs were taken of each sample for later particle size distribution analysis. The electron micrographs were enlarged by a factor of three or four for the actual distribution measurements. The particle size distributions were obtained from the micrographs with a Zeiss "Videoplan". Actual particle size distributions were determined by measuring 300 to 900 particles from each sample.

#### 2.4 Results

Figure 2.3 shows some typical powder produced by vapor phase hydrolysis. The technique does produce nonagglomerated single crystal particles whose morphologies range from cubes, to octahedra, to what appear to be hexagonal plates as seen in Figure 2.4. Octahedral habit was the most commonly observed.



Figure 2.3 Powder produced at 900°C; nickel chloride pressure =  $4 \times 10^{-4}$  atm.; H<sub>2</sub>O pressure = 0.122 atm; flow rate = 3.3 l/min. Average particle size = 3.2 micrometers.

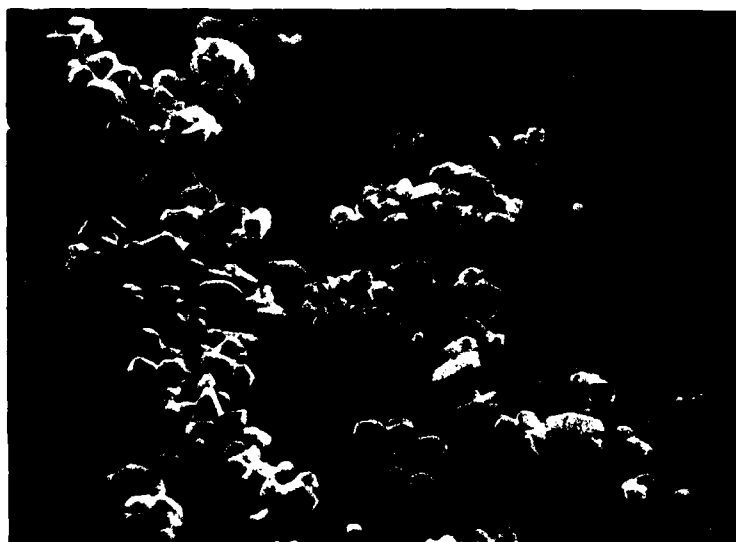


Figure 2.4 Hexagonal plate particles produced at 800°C; NiCl<sub>2</sub> pressure =  $4 \times 10^{-3}$  atm.; H<sub>2</sub>O pressure = 0.122 atm.; flow rate = 3.3 l/min; average particle size = 2.9 micrometers.

Figure 2.5 illustrates some of the actual particle size distribution data as obtained from the Videoplan output. Clearly, the particle size distributions are lognormal and this was found to be universally true. Note that all the particles are within an order of magnitude and that about eighty percent of the particles are within a factor of five. Figure 2.6 gives particle size distributions from two runs under identical conditions and demonstrates the reproducibility of the system and the process. Note that not only are the average particle sizes virtually identical but the distributions are as well. Figures 2.7 and 2.8 show the effect of increasing the reactant gas partial pressure. In both cases, the average particle size decreases as the supersaturation increases and there is a tendency for the size distribution to become broader. The cumulative distributions are plotted in order to separate the data and show the effects of the variables more clearly. Figure 2.9 shows the effect of reaction temperature. The data indicate that the average particle size first increases with temperature and may then decrease. Figure 2.10 shows the effect of carrier gas flow rate on particle residence time in the hot zone.

## 2.5 Discussion and Conclusions

These results are clearly encouraging. Equiaxed, nonagglomerated powders have been produced by vapor phase hydrolysis. The particle size distributions are, perhaps surprisingly, lognormal. However, the distributions are

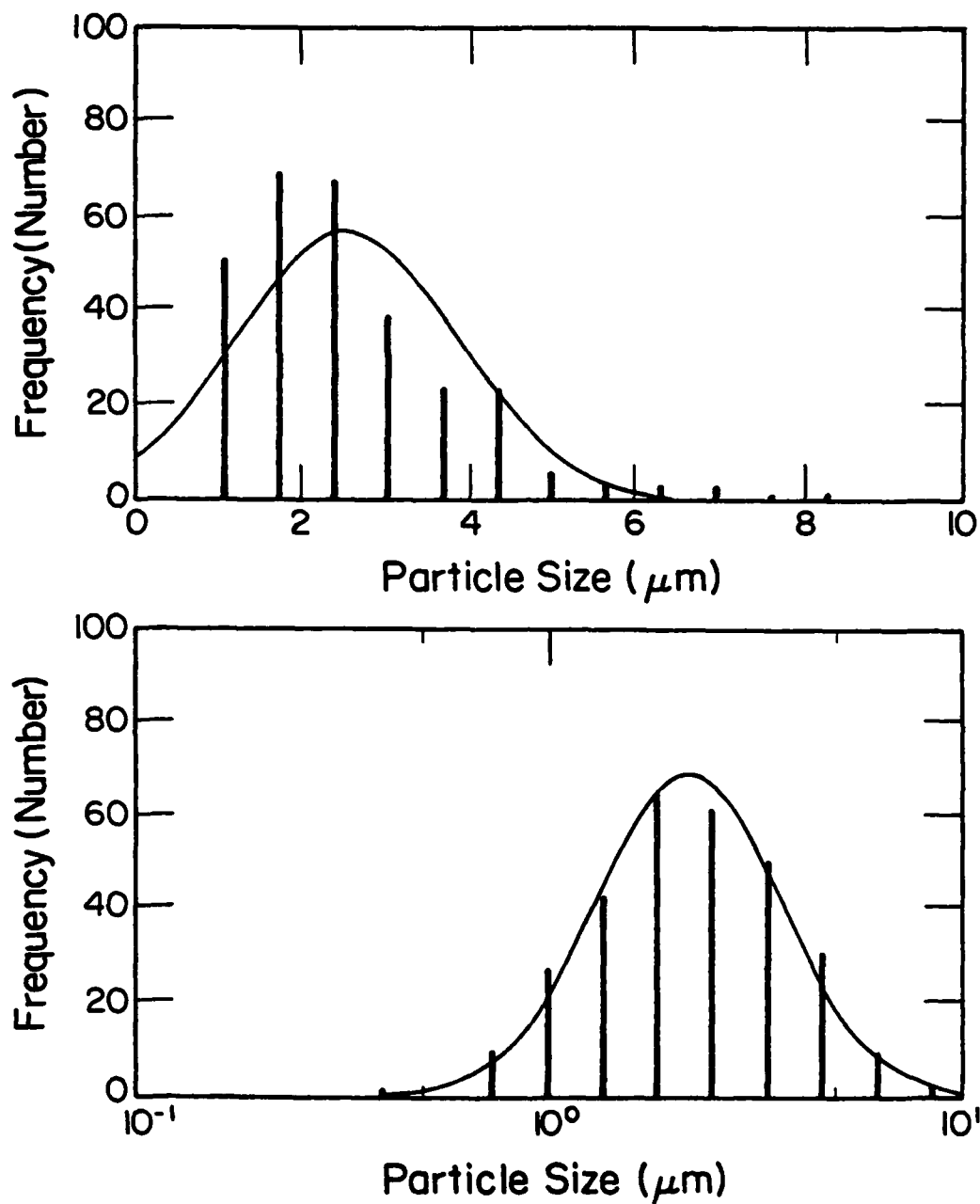


Figure 2.5 Particle size distributions. Top: data as taken, drawn curve is the best fit normal distribution to the data. Bottom: same but fit to a lognormal distribution. The run conditions were:  $T = 950^{\circ}\text{C}$ ;  $\text{NiCl}_2$  pressure = 0.1 atm.;  $\text{H}_2\text{O}$  pressure = 0.12 atm.; flow rate = 4 l/min.

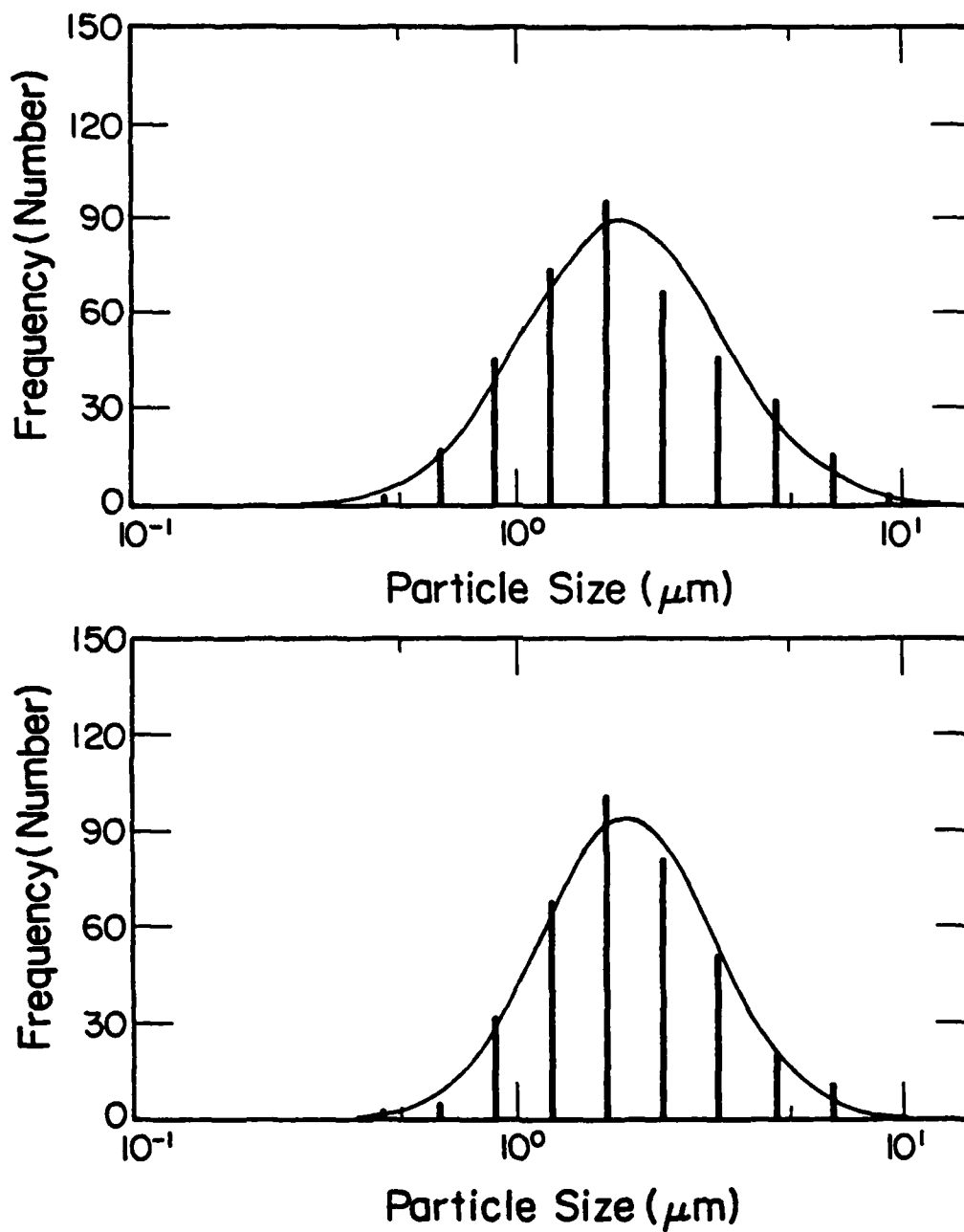


Figure 2.6 Two particle size distributions obtained from two runs under identical conditions:  $T = 1000^{\circ}\text{C}$ ;  $\text{NiCl}_2$  pressure = 0.1 atm.;  $\text{H}_2\text{O}$  pressure = 0.12 atm.; flow rate = 4 l/min.

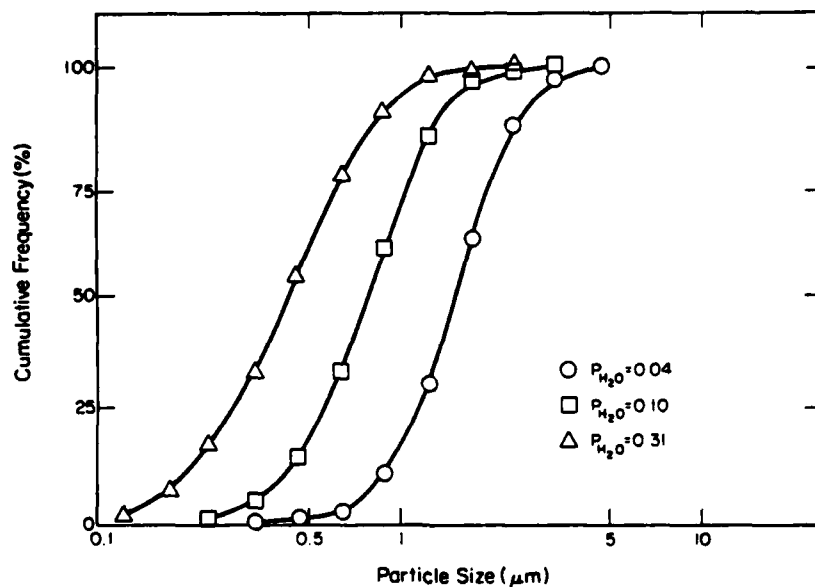


Figure 2.7 Effect of  $\text{H}_2\text{O}$  pressure on particle size distributions. Other conditions were:  $T = 900^\circ\text{C}$ ;  $\text{NiCl}_2$  pressure = 0.1 atm.; flow rate = 3 l/min.

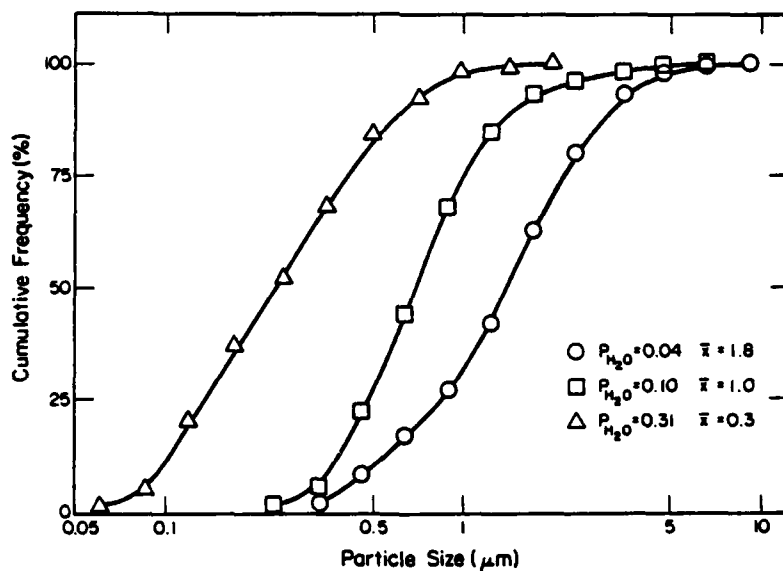


Figure 2.8 Effect of  $\text{H}_2\text{O}$  pressure on particle size distributions at a higher  $\text{NiCl}_2$  pressure. Other conditions were:  $\text{NiCl}_2$  pressure = 0.27 atm.;  $T = 950^\circ\text{C}$ ; flow rate = 3 l/min.

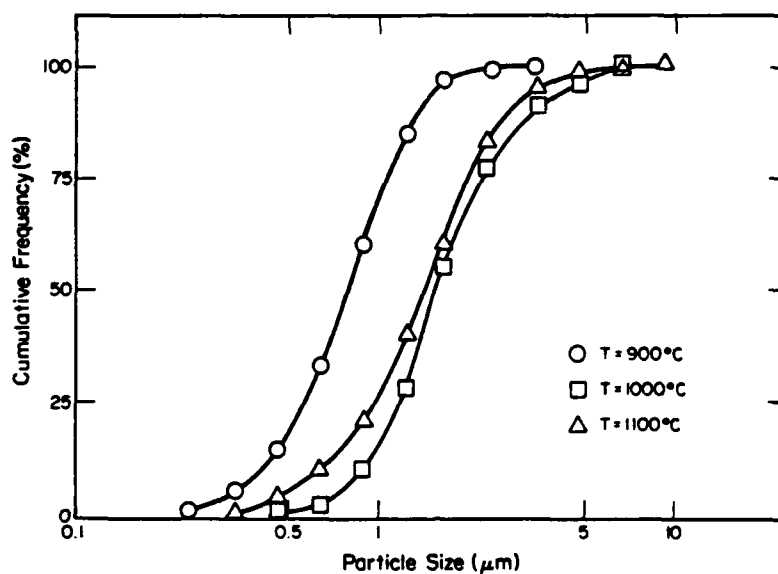


Figure 2.9 Effect of the reaction temperature on particle size distributions. Other conditions were:  $\text{NiCl}_2$  pressure = 0.1 atm.;  $\text{H}_2\text{O}$  pressure = 0.12 atm.; flow rate = 3 l/min.

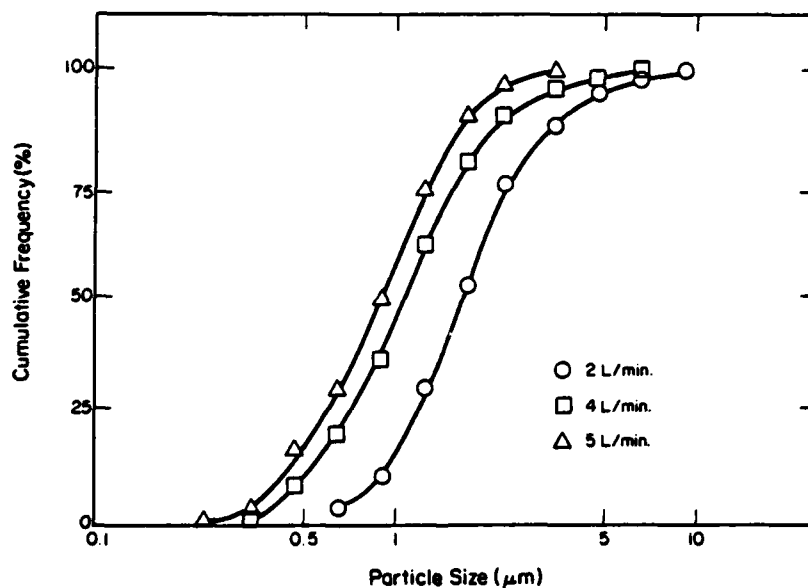


Figure 2.10 The effect of the flow rate on the particle size distributions. The other conditions were:  $T = 900^\circ\text{C}$ ;  $\text{NiCl}_2$  pressure = 0.1 atm.;  $\text{H}_2\text{O}$  pressure = 0.1 atm.



reasonably narrow and the average particle size is about the desired size for sintering of oxides, namely, about one micrometer. The effects of the variables is more or less what might be expected from classical nucleation and growth theory. Increasing the flow rate, as expected, decreases the particle size by decreasing the residence time of the growing powder particles in the furnace. Increasing the concentration of the reactant gases or increasing the temperature, both of which increase the supersaturation, lead to a smaller average particle size which is strongly suggestive of homogeneous nucleation.

## 2.6 References

1. W. H. Rhodes, J. Am. Ceram. Soc. 64 19 (1981).
2. J. D. Holmgren, J. O. Gibson, and C. Sheer, p. 129 in Ultrafine Particles, W. E. Kuhn, ed., (Wiley, N. Y.), 1968.
3. J. D. F. Ramsay and G. G. Avery, J. Mater. Sci. 9 1681 (1974).
4. T. Yoshida, et al., J. Mater. Sci. 14 1624 (1979).
5. M. L. Nielsen, P. M. Hamilton, and R. J. Walsh, pl81 of reference 2.
6. V. Suyama and A. Kato, J. Am. Ceram. Soc., 59 146 (1976).
7. V. Suyama, T. Mizobe, and A. Kato, Cer. Int. 3 141 (1977).
8. J. Tanaka and A. Kato, Yogyo-Kyoka-Shi, 81 179 (1973).
9. A. Kato, et al., Yogyo-Kyoka-Shi, 83 23 (1975).

### 3. PREPARATION OF NICKEL OXIDE POWDERS BY REACTIONS IN MOLTEN SALTS

#### 3.1 Introduction

Molten salts are an important class of nonaqueous solvents which are potentially useful for the preparation of both simple and complex oxide and nonoxide powders. The flux growth of ternary oxides in molten salts is a widely used method for the preparation of complex single crystal oxides. One variation of the molten salt technique in which ferric oxide is reacted directly with a molten alkaline earth chloride or fluoride has been used to produce  $\text{SrFe}_{12}\text{O}_{19}$  and  $\text{BaFe}_{12}\text{O}_{19}$ <sup>1</sup>. The technique resulted in some small transparent platelets approximately 50 micrometers thick and one millimeter in diameter. However, most of the product was reported as polycrystalline. The polycrystalline material probably resulted from the reaction of dissolved BaO on the surface of  $\text{Fe}_2\text{O}_3$  powder. It is interesting to note that attempts to use magnesium chloride melts were unsuccessful because MgO preferentially precipitated out of the molten salt. Many other oxides have been produced by the same technique<sup>2</sup>.

Another molten salt solvent that has been used in the preparation of oxide compounds uses ternary or binary alkali halides. A 50 m/o NaCl - 50 m/o KCl molten salt was used by Arendt for reacting  $\text{Fe}_2\text{O}_3$  and divalent metal carbonate, oxide, hydroxide, or nitrate<sup>3</sup>. The method was used for the production of  $\text{BaFe}_{12}\text{O}_{19}$  and  $\text{SrFe}_{12}\text{O}_{19}$  powders. The resulting powders

produced by this method were agglomerated. Lead zirconate-titanate powders have been produced utilizing molten salts in the KCl-NaCl system<sup>4</sup>. The desired reactants, a mixture of oxides, carbonates, and hydroxides, were mixed with the salts and reacted. The powders produced were also agglomerated.

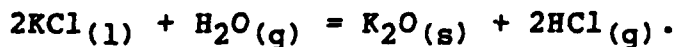
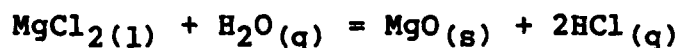
Yamaguchi<sup>5</sup> has used  $\text{Li}_2\text{SO}_4$ - $\text{Na}_2\text{SO}_4$  molten salts for the preparation of nickel ferrite powders. Nickel oxide and ferric oxide powders were reacted in varying amount of the molten salt. The salt composition was 36.5 m/o  $\text{Na}_2\text{SO}_4$ . The resulting ferrite powders were profoundly influenced by the particle size of the starting oxides. When nickel oxide of 0.03 micrometer primary crystallite size was used, the morphology of the ferrite powder resembled the morphology of the starting  $\text{Fe}_2\text{O}_3$  powder. When nickel oxide of one micrometer primary crystallite size was used, the morphology of the ferrite was small octahedra. Yamaguchi postulated that the dissolution rate of nickel oxide relative to the dissolution rate of ferric oxide is the controlling factor. The ferrite powders resemble the morphology of the starting  $\text{Fe}_2\text{O}_3$  when the dissolution rate of nickel oxide is greater than the dissolution rate of ferric oxide. It is assumed that the reaction takes place at the ferric oxide surface. Ferrite particles of octahedral habit were formed when the dissolution rates were approximately equal. In this case it is postulated that the reaction occurs between dissolved nickel oxide and dissolved ferric oxide resulting in the precipitation and growth of the ferrite.

### 3.2 Other Potential Molten Salt Powder Preparation Methods

There are several other possible techniques for powder preparation which utilize molten salts. These include precipitation from a melt, internal oxidation, and decomposition of a soluble constituent.

The fact that oxides are soluble in molten halides is well established and is, of course, the basis of electrochemical preparation of aluminum and other metals. Precipitation can be carried out in a controlled manner by either cooling of the melt or gradual evaporation of the halide solvent.

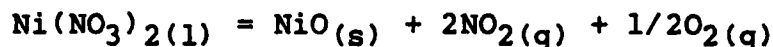
A technique for powder preparation, with apparently broad potential, is internal oxidation mixed halide melts. The process is similar to internal oxidation of metals which yields a dispersion fine oxide particles in a metal matrix. For example, consider a mixed halide melt of KCl and  $\text{MgCl}_2$  and the reactions:



At  $1000^\circ\text{K}$ , the free energy <sup>6</sup> for the first reaction is +7.3 kcal/mole and +49.5 kcal/mole for the second. Therefore, by reacting the mixed molten salts with the proper  $\text{H}_2\text{O-HCl}$  atmosphere it should be possible to preferentially oxidize the  $\text{MgCl}_2$  to  $\text{MgO}$  which will precipitate as a solid. On freezing, the solid oxide particles can be easily removed from the mixed halide by dissolving the halide in aqueous solutions. In principle, the particle size and morphology of the oxide precipitate can be

controlled by the temperature and the rate of reaction. Also, ternary oxide compounds or solid solutions should be possible by adjusting the composition of the melt so the mixed oxide is the preferred phase.

A variation on this same technique is the decomposition of a molten salt in another to form a solid oxide. For example,  $\text{Ni}(\text{NO}_3)_2$  is soluble in the alkali nitrates such as  $\text{NaNO}_3$ . Quite simply, the molten nickel nitrate dissolved in the melt decomposes by:



with the resulting NiO precipitating as solid particles. This reaction offers even greater promise of homogeneous formation of the solid powder particles.

In this research, both of these latter two techniques were briefly investigated.

### 3.3 Experimental

Anhydrous nickel chloride was prepared as previously described in section 2.3.2. Baker reagent grade NaCl, KCl, and LiCl were used for preparation of eutectic melt compositions. Fifty gram batches consisting of from one to twenty mole percent nickel chloride were placed into platinum crucibles. The melts were isothermally heated at temperatures ranging from 500 to 900°C for various time periods. The molten salts were withdrawn and air cooled after the isothermal heating period.

The NiO powder product was removed from the solidified salt by dissolving the salt with distilled water. The NiO powder was

collected by centrifuging the liquid in 250 ml polyethylene bottles. Four washing cycles were used to ensure removal of the remaining soluble salts.

Particle size size distributions were determined with an MSA particle size analyzer. A feeding solution consisting of 70 percent water, 30 percent acetone, and a few drops of Darvan #7 as a dispersant was used for the particle size sedimentation analysis. The MSA analyzer does not measure particle sizes below 0.5 micrometer so the particle size distributions begin at 0.5 micrometers.

#### 3.4 Results and Discussion

Particle size distributions of nickel oxide powders produced by 15 minute isothermal heating at temperatures from 650 to 850°C in air of one mole percent nickel chloride in eutectic alkali halide melts are shown in Figure 3.1. The particle size increases with increasing temperature and the distribution becomes narrower. Typical powders are shown in Figure 3.2. Both spherical and agglomerated powders were produced in all experiments. From observations of the melting behavior and the solidified salts after cooling, it is felt that the agglomerates form by hydrolysis reactions during the initial heating on undissolved nickel chloride particles in the melt. Similar results were obtained with higher concentrations of  $\text{NiCl}_2$  and with longer heating times.

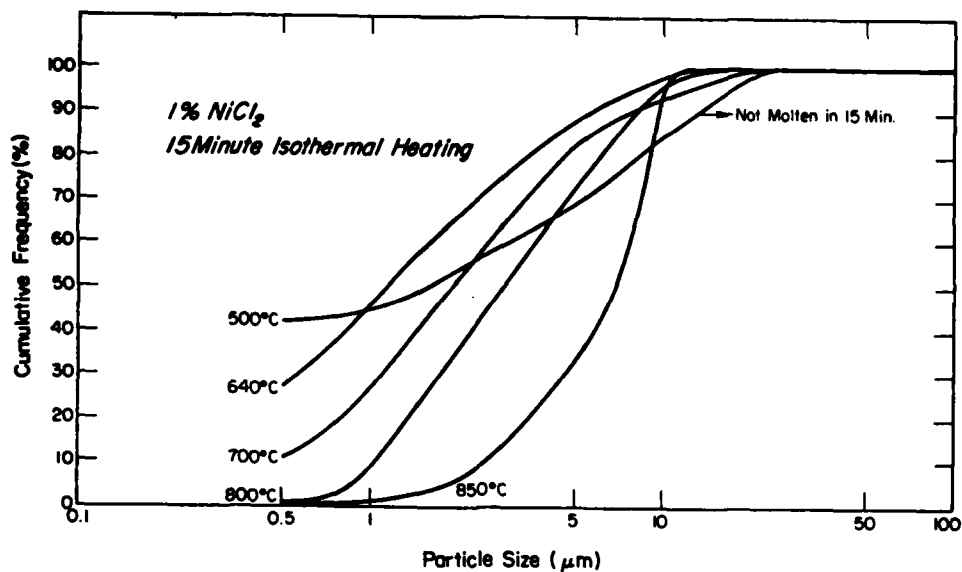


Figure 3.1 Particle size distributions of nickel oxide powders produced by 15 minute isothermal heating at temperatures from 650 to 850°C in air of one mole percent nickel chloride in eutectic alkali halide melt.

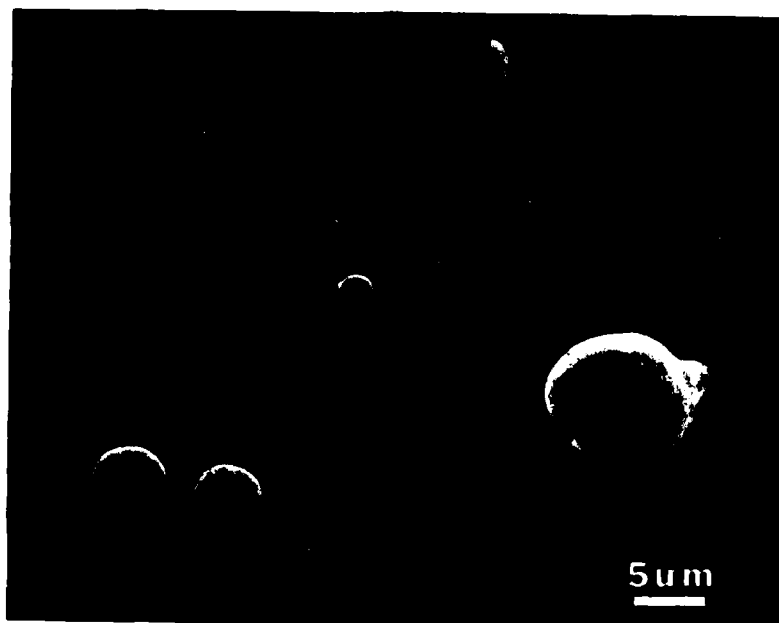


Figure 3.2 NiO powder produced by heating a one mole percent  $\text{NiCl}_2$  eutectic melt at 800°C for 15 minutes.

### 3.5 Conclusions

The experiments conducted with the one mole percent nickel chloride melts indicate that spherical powders can be produced by the oxidation of halide melts. However, it is quite clear that the nickel chloride can not be added to the initial melt in order to obtain nonagglomerated, small particles. Due to the lack of promise of this technique, it was abandoned in lieu of the more promising vapor phase hydrolysis discussed earlier.

### 3.6 References

1. L. H. Brixner, J. Am. Chem. Soc. 81 3841 (1968).
2. L. H. Brixner and K. Babcock, " Mat. Res. Bull. 3 817 (1968).
3. R. H. Arendt, J. Solid State Chem. 8 339 (1973).
4. R. H. Arendt, Mat. Res. Bull. 14 703 (1979).
5. T. Yamagucki, et al., J.Mat.Sci. 15 1491 (1980)
6. D. R. Stull and H. Prophet, et al., JANAF Thermochemical Tables, 2nd ed., (U.S. Government Printing Office, Washington DC), 1971.



## 4. CONTROLLED PRECIPITATION OF NICKEL OXIDE POWDERS

### 4.1 Introduction

Preparation of powders of controlled characteristics is one of the critical steps in controlling the microstructure of ceramics. The green density, fired density, grain size, and pore size of a fired ceramic all depend upon the treatment and characteristics of the starting powders. Thus, the importance of well-defined powders and powder production methods becomes apparent<sup>1,2</sup>.

Presently, powders are being produced in the same manner as they have been for years. They are being precipitated rather haphazardly by the method of direct mixing of solutions. Direct mixing is an uncontrolled method of precipitation from aqueous solution which leads to a powder consisting of large agglomerates of particles inhibiting densification. In order to enhance densification, it has been postulated that starting powders should have a uniform particle size and morphology in addition to being free of agglomerates<sup>2</sup>.

The only way to produce a powder with the characteristics described above is to control the precipitation processes that are used to produce the powder. There are two ways of accomplishing this both of which involve homogeneous precipitation. The first method which has been extensively studied<sup>3-5</sup> utilizes the temperature dependence of the solubility of sparingly soluble metal hydroxides. As the temperature increases the solubility of these hydroxides decreases so by

preparing solutions at room temperature and heating them to temperatures above the solubility limit precipitation occurs homogeneously throughout the solution. By heating aqueous solutions of chromium, zirconium, and aluminum salts at temperatures around 90°C for several days, precipitates having uniform particle sizes and spherical morphologies were produced. The second method<sup>6,7</sup> utilizes the decomposition of urea in water at temperatures above 70° to produce a homogeneous solution of hydroxyl ions. By decomposing urea in aluminum salt solutions at 90°C, aluminum hydroxide precipitates of uniform size (~ 1 micrometer) and spherical morphology were produced<sup>6</sup>. This method not only produced a desirable powder, but also did it in shorter times with a higher yield than the alternative method. It was also determined that these powders retained their spherical morphology after calcining<sup>6</sup>.

The purpose of this research was to extend the work on this second method to another system,  $\text{Ni}(\text{OH})_2\text{-NiO}$ , and to investigate the conditions in which uniform particles can be precipitated and characterize their morphology. One reason this system was chosen was that  $\text{Ni}(\text{OH})_2$  is highly anisotropic having the  $\text{CdI}_2$  structure<sup>8</sup> and a plate-like precipitate morphology is expected. Thus, if individual crystallites were produced, they would be highly anisotropic and not likely to form the "ideal" precursor material for the spherical powder particles thought to be desirable for powder consolidation and sintering of ceramics.

However, perhaps on calcination, such particles would tend to spherodize. On the other hand, if agglomerates resulted from the precipitation process, perhaps they would be more or less spherical. If so and they could be kept small by controlling the precipitation conditions, then calcination of the agglomerates could yield the desirable spherical oxide powders.

#### 4.2 Experimental

Solutions containing varying amounts of  $\text{NiCl}_2 \cdot 6\text{H}_2\text{O}$  between 0.005 to 0.10 moles/liter and urea,  $\text{CO}(\text{NH}_2)_2$ , between 0.1 and 2.00 moles/liter were prepared and heated in polyethylene containers at temperatures between  $70^\circ$  and  $95^\circ\text{C}$ .  $\text{HCl}$  was added to each solution to adjust the solution pH to a value of  $\text{pH} = 2.0$ . This was done to insure that precipitation would not begin before the temperature of interest was reached. After about 18 hours, each solution was removed from the oven and cooled to room temperature. The precipitate was then separated from the solution by centrifugation and then washed repeatedly with water and alcohol.

The precipitates were analyzed by scanning electron microscopy and the particle size and distribution determined quantitatively with a Zeiss Videoplan image analyzer.

#### 4.3 Results and Discussion

##### 4.3.1 Precipitate morphologies

Microscopic analysis of the powders formed under the conditions previously specified revealed five different particle

morphologies. Of the five, two were agglomerates of either small plates or small irregularly shaped crystallites and were of little interest. The remaining three were spherical agglomerates of plates, small spheres, or a combination as seen in Figure 4.1. In what follows, these will be referred to as morphologies one, two, and three, respectively.

Each of these spherical agglomerates formed under certain conditions of temperature and reactant concentrations. Precipitates with particles having morphology number one, were obtained at all temperatures only at a nickel ion concentrations of 0.01 m/l and a urea concentration of 0.01 m/l. The conditions for precipitating particles of morphology three were less stringent. At all temperatures, morphology three was observed at nickel ion concentrations of 0.001-0.01 m/l and urea concentrations of 1.0 - 2.0 m/l.

Finally, particles of morphology two were obtained at a nickel concentration of 0.10 m/l and urea concentrations greater than 1.0, at temperatures of 90° and above. As the temperature decreased, this morphology could only be obtained at the higher concentrations of urea.

All the morphology versus environment data are represented graphically in Figures 4.2, 4.3, and 4.4, in which the dashed lines indicated regions of constant supersaturation ratios. The supersaturation ratio here is defined as  $[Ni^{2+}][OH^{-}]^2/K_{sp}$  where

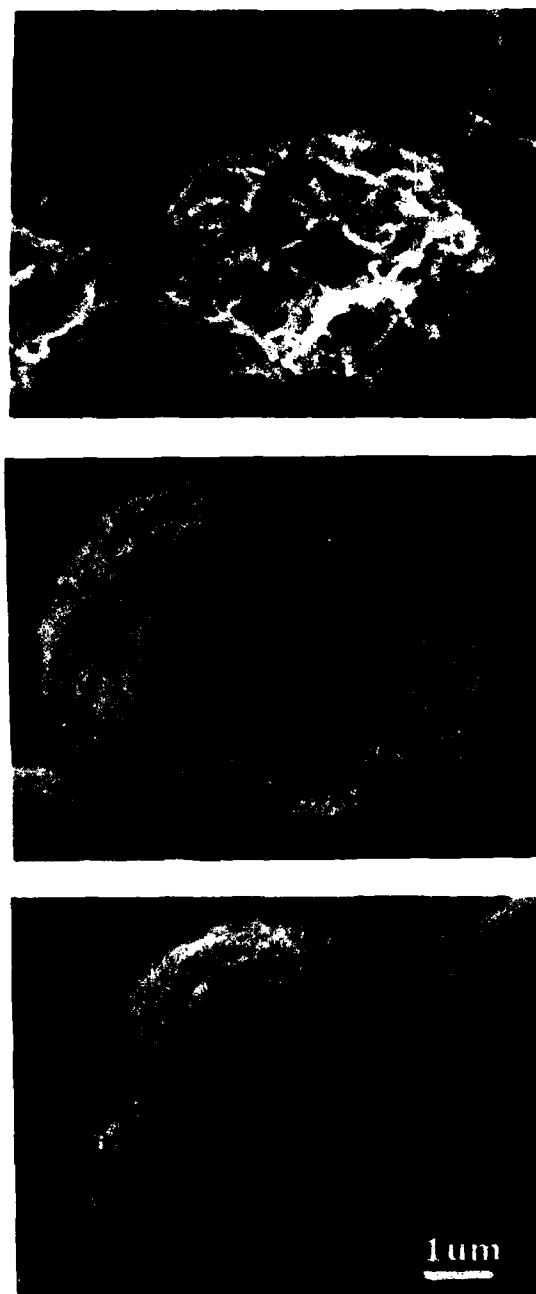


**Figure 4.1** Particle morphologies. Top: morphology one,  $T = 90^{\circ}\text{C}$ ,  $[\text{ureal}] = 0.1 \text{ m/l}$ ,  $[\text{Ni}^{++}] = 0.01 \text{ m/l}$ . Middle: morphology 2,  $[\text{ureal}] = 1.0 \text{ m/l}$ ,  $[\text{Ni}^{++}] = 0.1 \text{ m/l}$ . Bottom: morphology 3,  $[\text{ureal}] = 1.0 \text{ m/l}$ ,  $[\text{Ni}^{++}] = 0.01 \text{ m/l}$ .

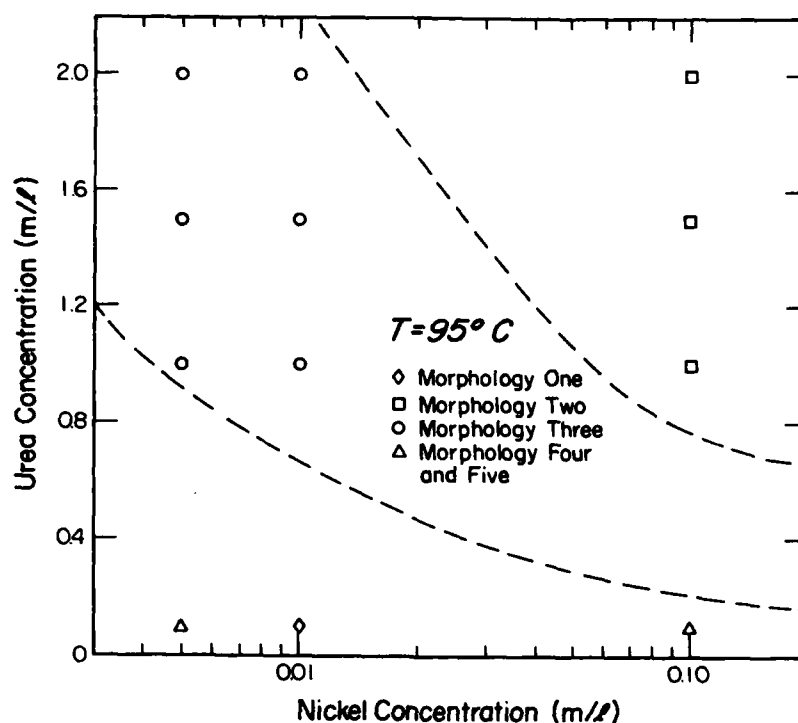


Figure 4.2 Urea versus nickel ion concentration showing dominant precipitate morphologies as a function of supersaturation ratios (dashed lines),  $T = 95^{\circ}\text{C}$ .

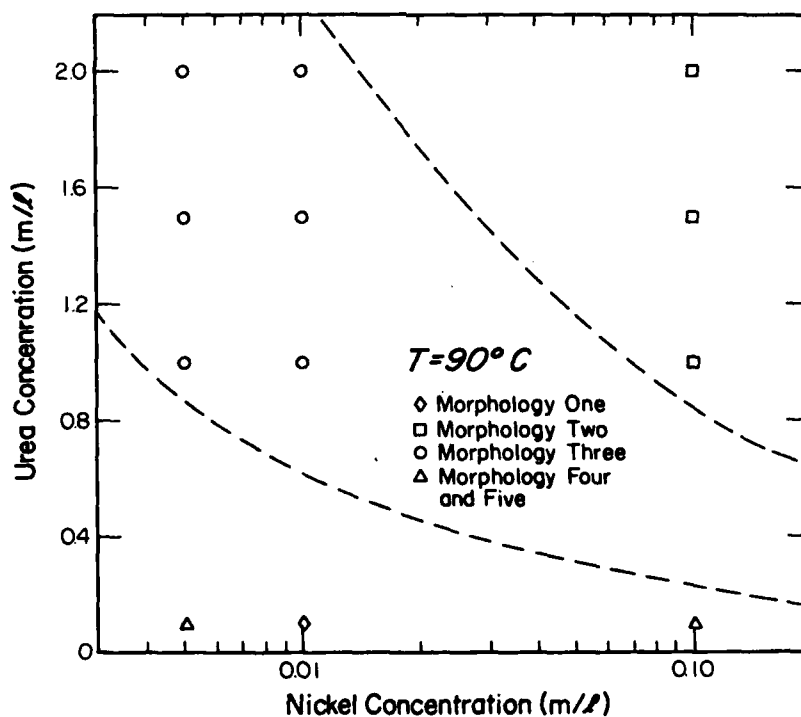


Figure 4.3 Urea versus nickel ion concentration showing dominant precipitate morphologies as a function of supersaturation ratios (dashed lines),  $T = 90^{\circ}\text{C}$ .

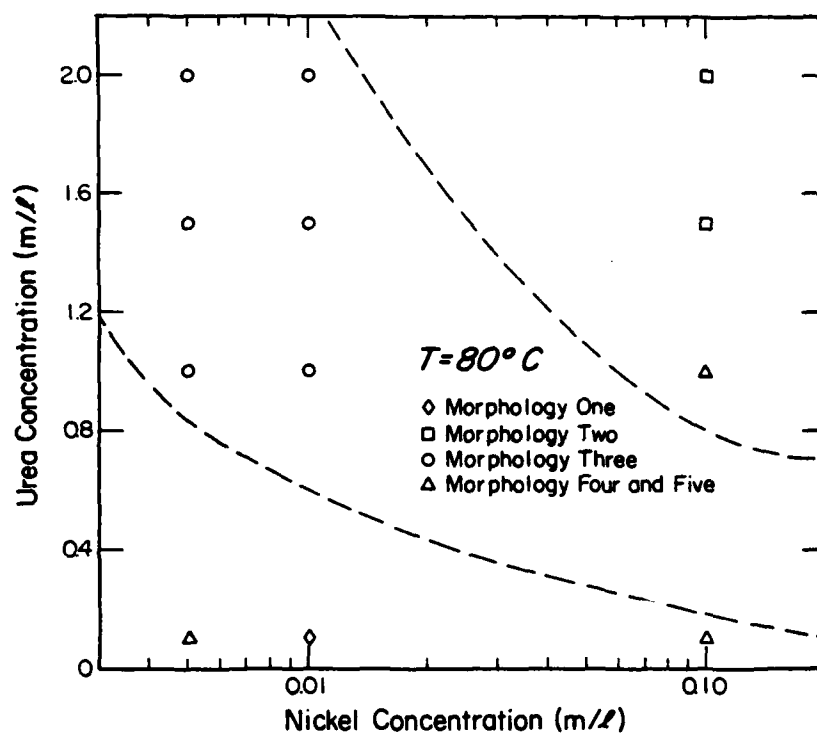


Figure 4.4 Urea versus nickel ion concentration showing dominant precipitate morphologies as a function of supersaturation ratios (dashed lines),  $T = 80^{\circ}C$ .

$K_{sp}$  is the solubility product of  $Ni(OH)_2$ . It is apparent from these Figures that morphology is dependent upon the supersaturation ratio.

#### 4.3.2 Particle size

Typical data illustrating the dependence of particle size on the three experimental parameters are shown in Figures 4.5 through 4.7. As demonstrated in these figures, the particle size is fairly independent of urea concentration and temperature, but slightly dependent upon the nickel ion concentration. For all practical purposes, it can be said that particle size is fairly independent of the environmental conditions in these experiments.

With regard to the particle size distribution, these precipitates are reasonably monodisperse as shown in the cumulative frequency distributions in Figure 4.8.

#### 4.3.3 Calcining

After calcining samples of precipitates representing each of the three spherical morphologies at  $600^{\circ}C$  for one hour in air, it was determined that the particles retained their original morphologies and decreased in size by a factor of about 50 percent. Photomicrographs of the calcined precipitates are shown in Figure 4.9.

#### 4.4.4 X-ray data

X-ray diffraction data of the precipitates indicated that the material obtained was in reality  $3Ni(OH)_2 \cdot 2H_2O$  instead of the expected  $Ni(OH)_2$ . The diffraction peaks were also quite broad



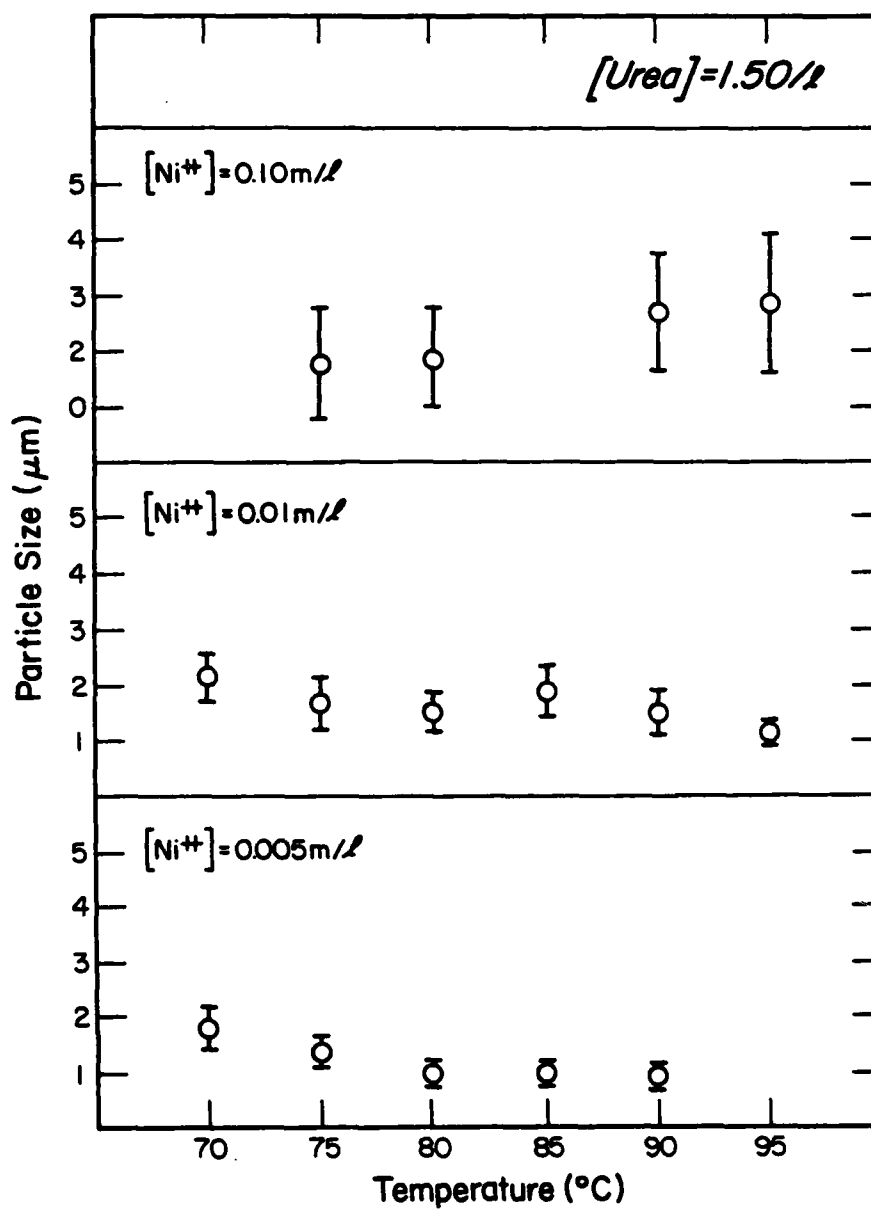


Figure 4.5 Precipitate particle size versus nickel concentration for a constant urea concentration.

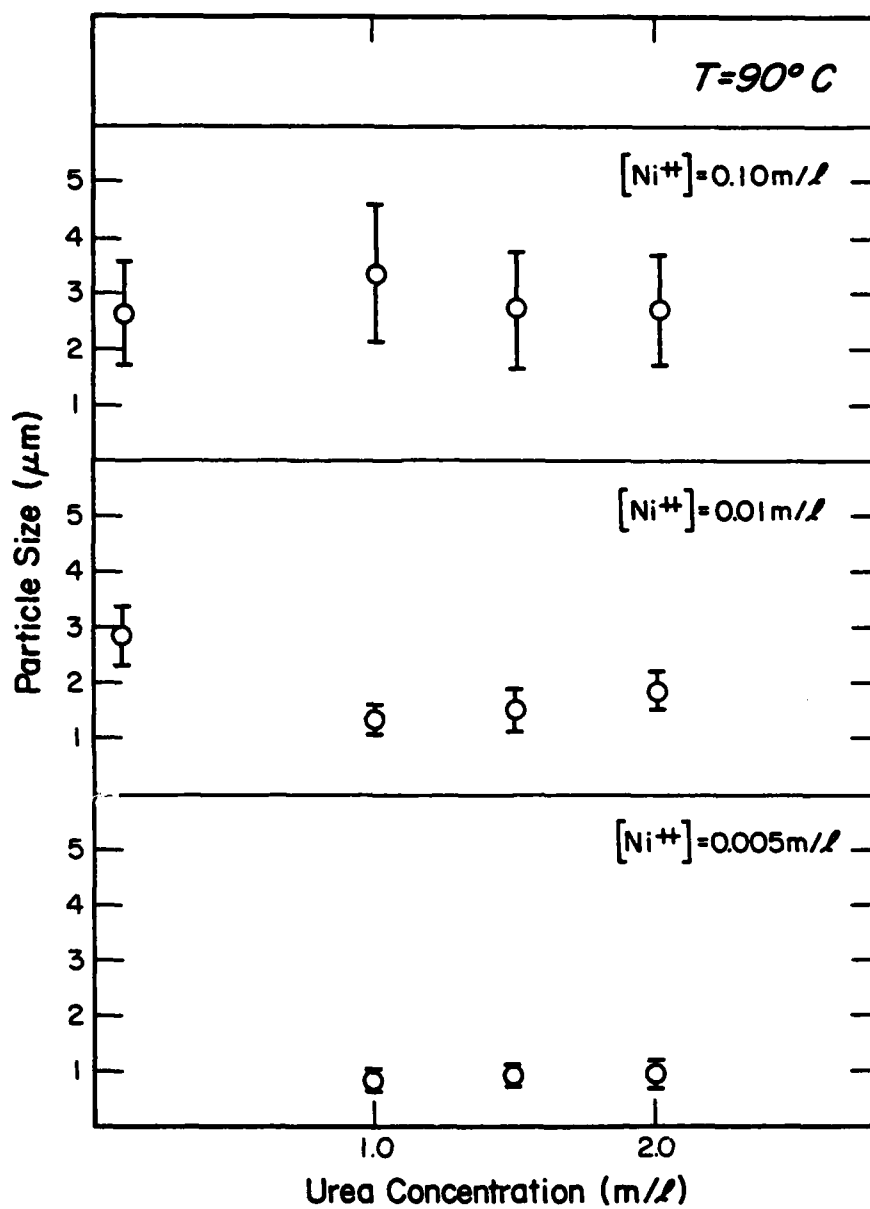


Figure 4.6 Precipitate particle size as a function of urea and nickel concentrations at a constant temperature.

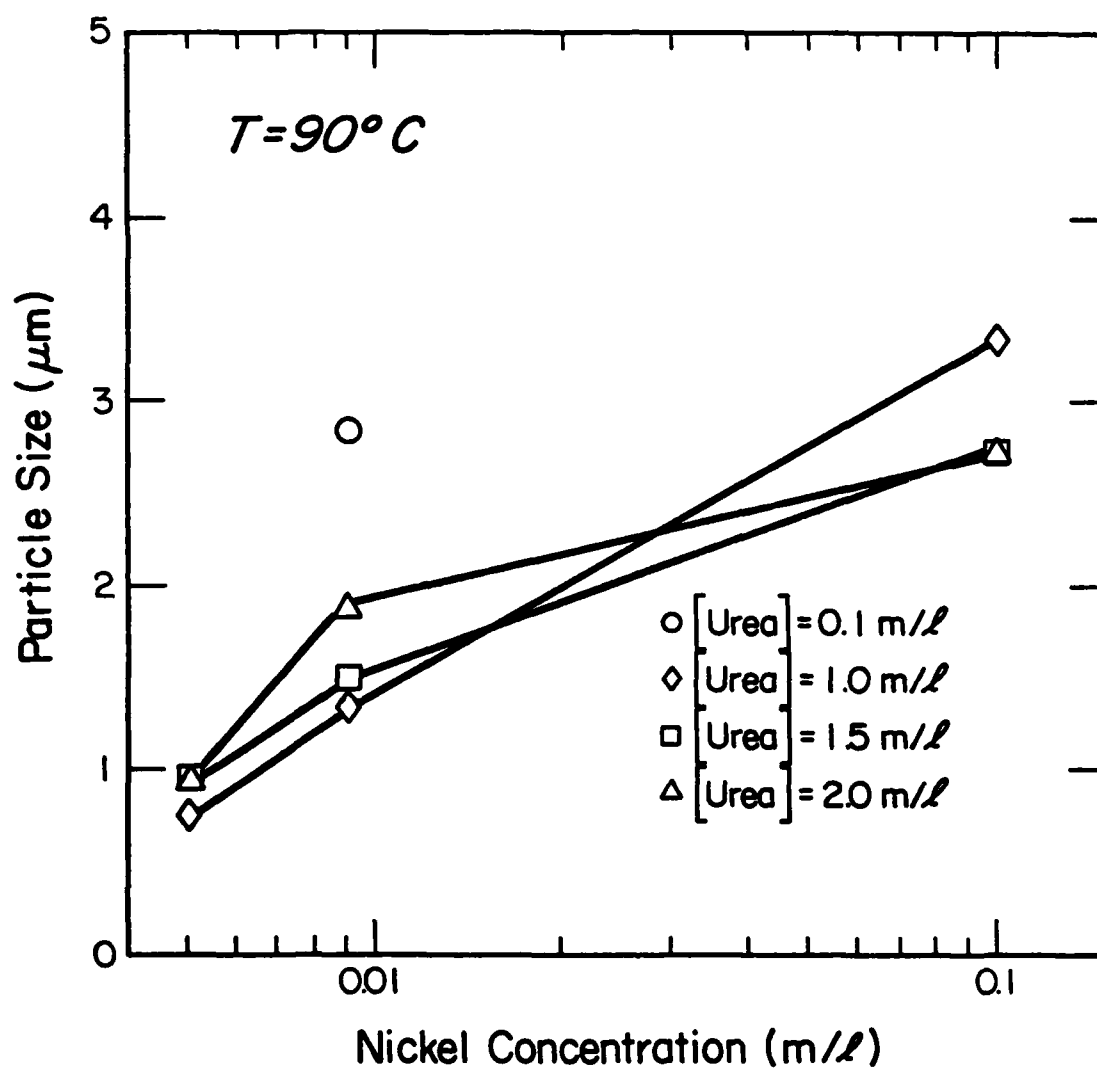


Figure 4.7 Precipitate particle size as a function of nickel and urea concentrations at a constant temperature.

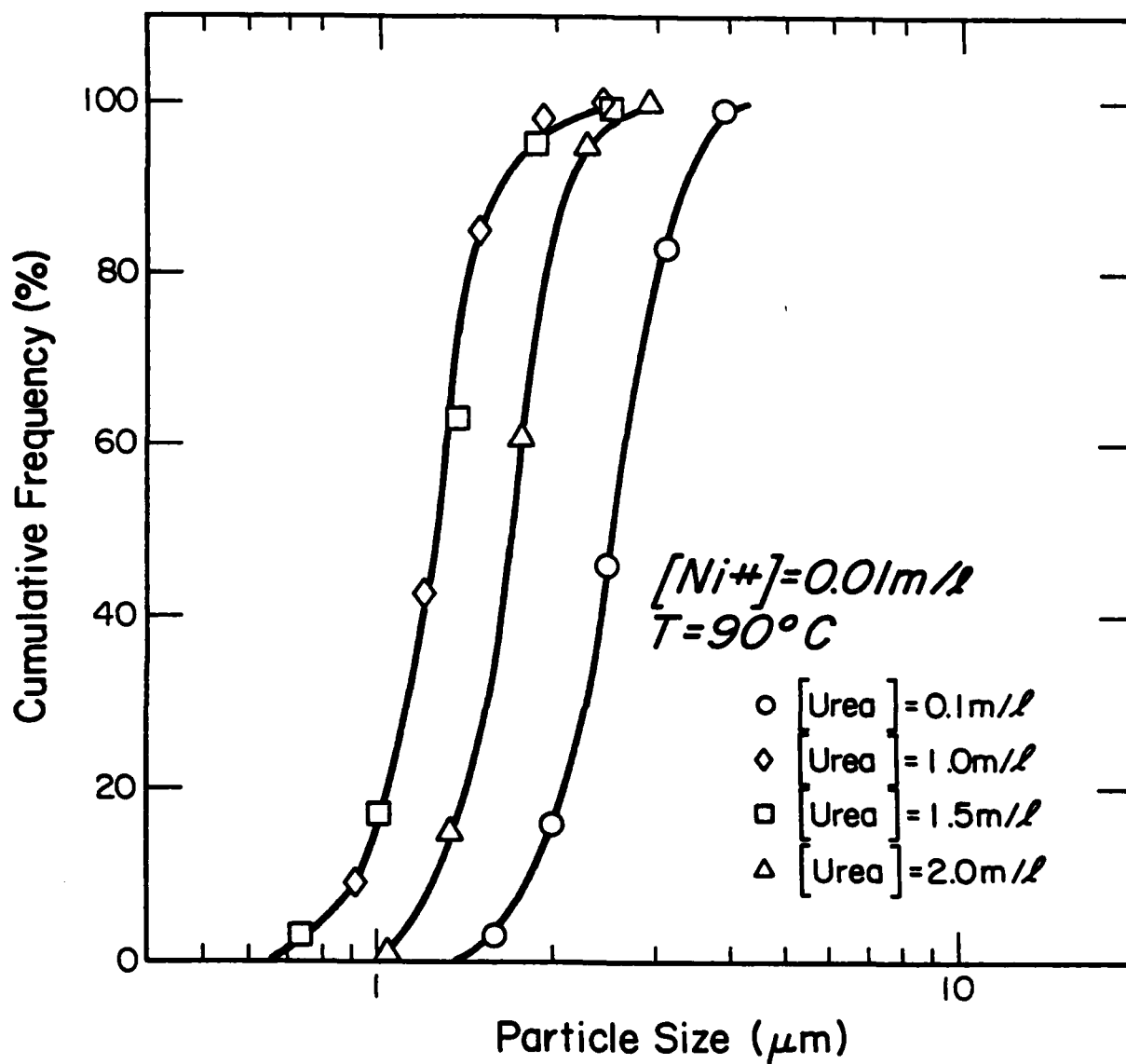


Figure 4.8 Typical precipitate particle size distributions as determined from photomicrographs.



Figure 4.9 Calcined particles calcined at 600°C in air for one hour.

being caused by the small size of the individual particles which comprise the spherical agglomerates. Diffraction patterns on the calcined material showed only the presence of NiO.

#### 4.4 Conclusions

The urea decomposition method is a desirable method for obtaining ceramic oxide powders of uniform size and shape. The particles so obtained are highly agglomerated but are nevertheless of a sufficiently small size, about one micrometer, so that their agglomerate nature is not a priori detrimental during sintering. The morphologies of the precipitate particles are dependent primarily on the reactant concentrations while the agglomerate size is virtually independent of any variable over the ranges studied in these experiments.

X-ray diffraction showed that the precipitate was  $3\text{Ni}(\text{OH})_2 \cdot 2\text{H}_2\text{O}$  and not  $\text{Ni}(\text{OH})_2$  as expected. Upon calcination, the precipitate agglomerates retain their spherical shape and shrink about 50 percent to NiO at  $600^\circ\text{C}$ .

#### 4.5 References

1. W. D. Kingery, p. 291 in Ceramic Processes Before Firing, G. Y. Onoda, Jr. and L. L. Hench, eds., (Wiley, N.Y.), 1978.
2. R. L. Coble and R. M. Cannon, p. 291 in Vol. 11 of Materials Science Research, Processing of Crystalline Ceramics, (Plenum, N.Y.), 1978.
3. E. Matijevic, et al., J. Electrochem. Soc. 120 893 (1975).
4. R. Brace and E. Matijevic, J. Inorg. Nucl. Chem. 35 3691 (1975).

5. W. B. Scott and E. Matijevic, J. Coll. Int. Sci. 66 447 (1978).
6. P. A. Curreri and G. Y. Onoda, to be published.
7. J. E. Blendell, H. K. Bowen, and R. L. Coble, Cer. Bull. 63 797 (1984)
8. Powder Diffraction File, (JCPDS, Swathmore, Pa.), p. 537, 1983.

## 5.0 VAPOR TRANSPORT AND SINTERING OF CERAMICS: THEORY

### 5.1 Introduction

There are many atmosphere effects which are important and play critical roles in the powder processing and microstructure development in high technology, single phase, ceramic materials. In this research, only the area of vapor transport during microstructure development is addressed. The primary reasons for this are that the effects of vapor transport are on good theoretical grounds and new experimental data are becoming available. On the other hand, the role of point defects on diffusional processes and microstructure development and how they are affected by the atmosphere is an important area. Unfortunately, the experimental data clearly relating point defect chemistry to changes in sintering behavior are lacking. Therefore, point defect chemistry and how it affects sintering is not covered.

### 5.2 Vapor Transport and Densification

#### 5.2.1 Observations and importance

Both vapor transport and surface diffusion can lead to neck growth without densification and are thus undesirable. However, vapor transport and its effects on the densification kinetics and microstructure development of ceramics has been probably the most neglected transport phenomenon both from an experimental and theoretical point of view. Nevertheless, it is an ideal process with which to study microstructural development in powder compacts since the transport coefficients are easily controlled, are



readily available in the literature or easily calculated. This is in contrast to the lack of control over solid, surface, and boundary diffusion coefficients for which there is also a paucity of good data. Furthermore, it is well known that many ceramic materials lose weight by sublimation during sintering which clearly implies a significant vapor pressure of the subliming species. For example, if the weight loss is by evaporation, the rate is determined by gaseous diffusion through some boundary layer of thickness "a" around the sample. The flux density,  $J$ , is then given by:

$$J = -D \frac{dC}{dx} = -D \frac{(C_i - C_o)}{a}$$

where  $C_i$  is the equilibrium concentration at the solid-gas interface,  $C_o$  is the concentration of the subliming species in the gas far from the surface, and  $D$  is the gaseous diffusion coefficient. If we consider the rate of weight loss from a spherical compact, expressing the gas phase composition in terms of pressure and assuming that  $C_o = 0$  we obtain:

$$\frac{1}{m} \frac{dm}{dt} = \frac{3DM}{radRT} p_o$$

where  $M$  = molecular weight  
 $r$  = sphere radius  
 $m$  = sphere mass  
 $d$  = solid density  
 $R$  = gas constant  
 $T$  = temperature  
 $p_o$  = equilibrium partial pressure.

For weight losses on the order of one percent per hour, the equilibrium partial pressure of the subliming solid is  $10^2$  N/m<sup>2</sup> if the other

parameters are typical for ceramic materials in the above equation. As will be discussed later, this is a relatively large vapor pressure compared to that necessary for vapor transport to contribute significantly to morphological changes within a powder compact. Many ceramic materials lose weight by sublimation during sintering<sup>1,2,3</sup> which clearly implies a significant vapor pressure of the subliming species. Therefore, certainly in those cases in pure materials in which a percent or more of weight is lost during sintering, vapor transport can play a significant role in densification and microstructure development. The presence of at least one volatile component is quite common in ceramics such as PbO in zirconate-titanates<sup>4</sup>, Cr<sub>2</sub>O<sub>3</sub> in chromites<sup>5</sup>, and Na<sub>2</sub>O in beta alumina<sup>6</sup>.

#### 5.2.2 Vapor transport and sintering models

Kuczynski<sup>7</sup> and Kingery and Berg<sup>8</sup> examined vapor transport as a mechanism of neck growth in the initial sintering model shown in Figure 5.1. In this model vapor transport and surface diffusion can only contribute to neck growth and not shrinkage. Similar considerations and conclusions can be reached with intermediate stage sintering models since only the geometry is different. Therefore, in the following discussion, only the initial stage will be discussed. These derivations<sup>7,8</sup> for vapor transport are unique among the sintering models in that they assume that the mass transport rate is rapid and that the rate-limiting step is the evaporation or condensation step at

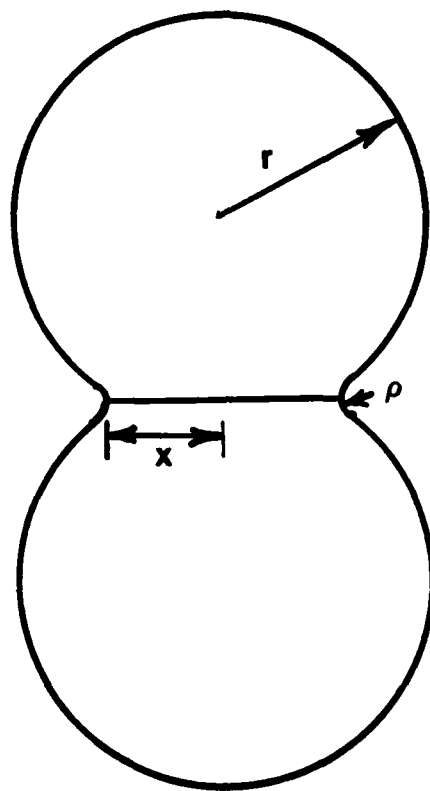


Figure 1. Two-sphere model of initial stage sintering.

the solid surface. That is, they assume that the surface reaction is rate-controlling while all the other transport models assume diffusion is rate controlling. For this case, the flux density at the neck surface (see Figure 5.1) is given by:

$$J = \frac{\alpha \gamma M}{d \rho RT} p_0 \left( \frac{M}{2\pi RT} \right)^{1/2}$$

where  $\alpha$  = sticking or accommodation coefficient  
 $\gamma$  = surface energy  
 $\rho$  = neck radius  
 $M$  = molecular weight  
 $d$  = solid density  
 $p_0$  = vapor pressure

and  $R$  and  $T$  have their usual meaning. The rate of neck growth,  $\dot{x}_v$ , in this case is given by<sup>8</sup>:

$$\dot{x}_v = \frac{\pi \gamma M}{2 \rho d^2 RT} \left( \frac{M}{2 \pi RT} \right)^{1/2} p_0$$

On the other hand, we can assume that diffusion through the gas phase is rate-limiting and obtain:

$$J = \frac{4D}{\pi \rho} \left( \frac{M}{RT} \right)^2 \frac{\gamma}{dr} p_0$$

and

$$\dot{x}_v = \frac{2D\gamma}{\pi \rho d^2 r} \frac{M^2}{RT} p_0$$

where  $D$  = gaseous diffusion coefficient  
 $r$  = sphere radius.

Equating these two fluxes we can obtain an estimate of the particle size at which gaseous diffusion becomes rate controlling:

$$r = D \frac{32M}{\pi RT}$$

For typical values of the gas diffusion coefficient ( $D \approx 1 \text{ cm}^2/\text{s}$ ), the temperatures over which sintering is important for ceramics ( $T \approx 1000 - 2000^\circ\text{C}$ ), the range of molecular weights for ceramics ( $M \approx 20-200 \text{ g/mole}$ ), and an accommodation coefficient of one, we find that  $r$  is on the order of one micrometer which is not untypical of the size particles undergoing sintering in a powder compact.

### 5.2.3 Vapor transport and volume diffusion

In order to judge the importance of vapor transport relative to the other transport processes possible during sintering, we shall compare the vapor transport contribution to neck growth with that of volume diffusion<sup>19</sup>. A significant obstacle to understanding sintering is that our knowledge of diffusive transport coefficients in ceramics is quite poor. The data are perhaps better for volume diffusion than for surface and grain boundary diffusion. Therefore, the comparison with volume diffusion is justified. For bulk diffusion, the rate of neck growth is given by<sup>7</sup>:

$$\dot{x}_D = \frac{2D_v \gamma \bar{v}}{RT \rho^2}$$

where  $D_v$  = volume or bulk diffusion coefficient  
 $\bar{v}$  = molar volume.

Therefore, the ratio of the rate of neck growth for vapor transport to that for volume diffusion, which gives a measure of the importance of vapor transport during densification, for typical sintering conditions is given by:

$$\dot{x}_v/\dot{x}_D = 2.1 \times 10^{-10} p_0/D_v (x/r)^2$$

for vapor diffusion control and

$$\dot{x}_v/\dot{x}_D = 8.1 \times 10^{-6} p_0/D_v r (x/r)^2$$

for reaction rate control where  $p_0$  is in dynes/cm<sup>2</sup> and  $D_v$  in cm<sup>2</sup>/s. As mentioned earlier, for particles larger than about one micrometer, vapor diffusion is rate controlling. For a shrinkage on the order of one percent, since  $\Delta L/L_0 \approx \rho/r = x^2/2r^2 = 0.01$ :

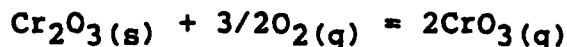
$$\dot{x}_v/\dot{x}_D = 4 \times 10^{-10} p_0/D_v$$

This implies that for systems which exhibit weight loss due to sublimation, ie.  $p_0 = 10^{-3}$  atm.  $\approx 10^2$  N/m<sup>2</sup>, vapor transport dominates unless  $D_v > 10^{-7}$  cm<sup>2</sup>/s which is a very large volume diffusion coefficient! Even for  $p_0 = 10^{-6}$  atm  $\approx 0.1$  N/m<sup>2</sup>, vapor transport will play a dominant role in neck growth for all shrinkages greater than 1% unless  $D > 4 \times 10^{-10}$  cm<sup>2</sup>/s! As shall be discussed below, there are many ways in ceramic systems to obtain partial pressures on the order of 0.1 N/m<sup>2</sup>.

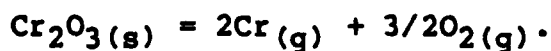
Of course, the undesirable feature of vapor transport during initial sintering is that it contributes to neck growth without shrinkage, hence, if present, will decrease the rate of sintering or densification. Since the ratio of vapor transport to diffusional neck growth is proportional to the particle size, vapor transport is more important for larger size particles. Therefore, it should be more readily observed in sintering large spheres rather than powder compacts. Because of this particle size dependence of vapor transport, it has largely been ignored

as being a significant transport process during sintering of powder compacts.

Vapor transport has been observed to contribute to neck growth but no shrinkage in sphere-to-sphere sintering experiments on  $\text{NaCl}^{8,10}$  and  $\text{ZnO}^{11}$  with calculated partial pressures on the order of  $10 \text{ N/m}^2$ . Nevertheless, both  $\text{ZnO}^{12,13}$  and  $\text{NaCl}^{14}$  powder compacts can undergo densification even though weight loss may occur during sintering indicating significant vapor transport<sup>14</sup>. One of the most interesting materials from the standpoint of the relation between densification and vapor transport is  $\text{Cr}_2\text{O}_3^{2,15,16}$  and the chromites<sup>15</sup> in which significant volatilization or weight loss occurs at all oxygen partial pressures. At high pressures, the following reaction dominates:



and at low pressures

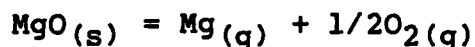


Interestingly, densification can only be achieved at low oxygen partial pressures.

#### 5.2.4 Vapor transport and atmospheres

For the present, assume that the effect of vapor transport is merely to contribute to neck growth and hence retard densification or shrinkage by volume diffusion processes. What are the possible atmospheric effects on vapor transport and densification? First there are compounds such as  $\text{NaCl}$  which have a high vapor pressure. In this case, the relative importance of

vapor transport will depend primarily on the relative temperature dependencies of the vapor pressure and the relevant solid state diffusion coefficient which controls densification. The gaseous diffusion coefficient can only be slightly changed by changing the ambient gas. However, for materials such as MgO or ZnO which vaporize as atomic species:



the equilibrium pressure,  $p_0$ , and the rate of vapor transport can be controlled by the oxygen partial pressure. For example, in hydrogen,



and at 2000°K in very dry hydrogen,  $p(\text{Mg}) \approx p(\text{H}_2\text{O}) \approx 300 \text{ N/m}^2$ <sup>17</sup> which is certainly large enough to produce significant vapor transport. On the other hand, in vacuum,  $p_0 = 0.3 \text{ N/m}^2$  and in air,  $p_0 = 10^{-3} \text{ N/m}^2$ . Therefore, the amount of vapor transport during sintering of MgO should depend critically on the atmosphere, being very important in a reducing ambient but of little consequence in air or oxygen. It has been shown that the rate of reaction of MgO and  $\text{Al}_2\text{O}_3$  to form spinel is higher in hydrogen due to rapid vapor transport of  $\text{MgO}$ <sup>18</sup>.

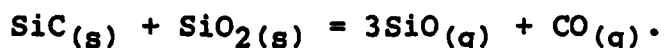
Vapor transport can be enhanced in a reducing atmosphere by the formation of volatile suboxides as in the case of alumina<sup>29</sup>:



Clearly, one of the main problems which impedes the densification of covalently-bonded ceramics is the difficulty in preventing vapor transport. The densification of silicon<sup>20</sup> and silicon-



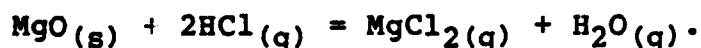
containing compounds such as SiC and Si<sub>3</sub>N<sub>4</sub> is inhibited by the formation of the volatile SiO species<sup>21</sup>:



For this reaction at 1800°C,  $p(\text{SiO}) = 10^3 \text{ N/m}^2$  so if any residual silica is present, vapor transport will clearly be important. Even with no residual silica, if the gas contains only 1 ppm of oxygen, vapor transport will be significant in these systems!

#### 5.2.5 Impurities and vapor transport

An example of one effect of impurities is vapor transport via halides. Halides are frequently present in oxide powders as impurities since precursor materials are often precipitated from halide solutions. Volatile halides are easily formed by reactions such as the following:



The free energy for this reaction is such that for halide impurity concentrations on the order of 1 ppm the partial pressure of MgCl<sub>2</sub> will be on the order of 0.1 N/m<sup>2</sup>. There have been no extensive studies performed on the effect of halide impurities on vapor transport or densification kinetics. However, it is part of the folk lore of ceramic processing that the presence of residual halide and other anion impurities is to be avoided. One qualitative piece of evidence that this mechanism is operative is that removal of chloride impurities in ZrO<sub>2</sub> lowers the temperature for densification on the order of 100°C<sup>22</sup>.

### 5.2.6 Vapor transport and particle coarsening

Another important effect of vapor transport is that it may contribute to or be responsible for the grain growth or Ostwald ripening that occurs during the initial and intermediate stages of sintering. For Ostwald ripening by diffusion in the surrounding gas phase<sup>23-27</sup>:

$$\bar{r}^3 = \frac{8}{9} \frac{D\bar{V}^2}{(RT)^2} p_o t$$

and for an interface controlled reaction:

$$\bar{r}^2 = \left(\frac{8}{9}\right)^2 \frac{K\bar{V}^2}{(RT)^2} p_o t$$

where  $\bar{r}$  = average particle radius  
 $K$  = surface reaction rate constant  
 $p_o$  = equilibrium partial pressure.

In addition, a characteristic of the classical Ostwald ripening theory is that the particle size distribution reaches a steady state distribution that is skewed to small particle sizes<sup>36</sup>. Again, in this case, if vapor transport significantly affects the rate of particle coarsening it would again decrease the rate of densification due to the reduction of surface area which, of course, is the driving force for densification.

## 5.3 Vapor Transport in Multicomponent Systems

### 5.3.1 Introduction

Vapor transport in a multicomponent system can provide a rapid transport path for one or more of the constituents during sintering. There are two distinct situations to consider in a

multicomponent system: 1. initial chemical uniformity and equilibrium between the constituents except for the surface energy driving forces; and 2. chemical heterogeneity and a nonequilibrium distribution of the constituents. The driving force for sintering is relatively small and can be completely overshadowed by nonequilibrium compositional inhomogeneities. This implies that any densification study in which additives are used, great care must be exercised to characterize the nature, distribution, and equilibrium or nonequilibrium state of the system in each stage of the sintering process in order to determine the true effect of any additive. Unfortunately, in far too many sintering studies with ceramics, additives have been used rather indiscriminantly giving results which are difficult if not impossible to analyze. In what follows we shall examine the first of these two situations, namely, an initially chemically homogeneous and equilibrium system.

### 5.3.2 Solid solution

For the sake of simplicity, consider a system of two components, A and B, which could of course be two compounds, which form an ideal solid solution. Nonideal solid solutions will not show radically different behavior. The chemical potentials of the two components are given by:

$$G_A = G_A^0 + RT \ln X_A + p\bar{v}$$

$$G_B = G_B^0 + RT \ln X_B + p\bar{v}$$

where  $X_A$  and  $X_B$  are the mole fractions, and the pressure,  $p$ , will be assumed to be produced by the surface tension force at the

neck region. Thus, the gradients in chemical potentials are:

$$\nabla G_A = \frac{RT}{X_A} \nabla X_A + \bar{v} \nabla p$$

$$\nabla G_B = \frac{RT}{X_B} \nabla X_B + \bar{v} \nabla p.$$

If one of the species, say B, moves rapidly via the vapor phase, then the gradient in chemical potential of B can approach zero and there will be a composition gradient between the neck region and the bulk of the material given by:

$$\nabla X_B = - \frac{\bar{v} X_B \nabla p}{RT}.$$

For typical values of the parameters for oxides at 2000°K and a neck radius on the order of 10 nanometers, the concentration difference,  $\Delta X_B$ , would be:

$$\Delta X_B \approx 0.08 X_B$$

or less than a ten percent increase in concentration. As the neck size becomes larger, the concentration difference of course becomes smaller. Figure 5.2 shows schematically how this increase in concentration can be explained with a free energy composition diagram. The curve for an ideal solution is lowered by the surface tension neck stress and the tangents to both curves must intersect the chemical potential of B at the same point since the gradient in the potential of B is assumed to be zero.

### 5.3.3 Multiphase system

If instead of a single phase solid solution system, the phase diagram consisted of one or more possible phases, then

rapid transport of constituent B could cause the appearance of a second phase at the neck region as depicted schematically in Figure 5.3 and has been observed experimentally in metal systems in which one constituent diffuses through the bulk more rapidly than the other<sup>28</sup>. The dashed lines in both the free energy composition diagram and the phase diagram show the effect of the surface tension stresses at the neck region. In order to have a second phase appear, the initial composition must be very near the phase boundary. Of course, a second phase could occur at the neck region without rapid transport of one of the species if the beta phase had a larger molar volume than the alpha phase. Then the free energy composition curve for beta would be lowered by the neck curvature stress more than that of alpha so that the alpha composition now lies in a two-phase region. This would be a stress-enhanced precipitation.

In any event, in principle, neck stresses alone, or in combination with rapid vapor transport, can lead to chemical inhomogeneities during sintering a powder compact. Certainly, such an inhomogeneity at the neck will affect grain boundary migration and resultant coarsening. It is interesting to speculate that some additives in solid solution which enhance densification may very well be efficacious for these reasons. The above considerations hold true, of course, regardless of the rapid transport mechanism of component B, be it vapor phase, volume, boundary or surface diffusion. These considerations are

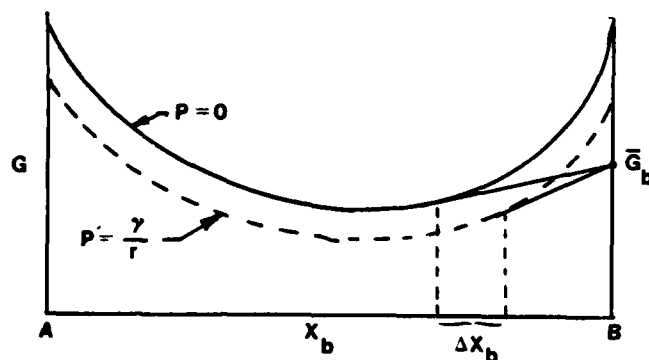


Figure 5.2 Free energy-composition diagram for an ideal solid solution in which component B is rapidly transported through the vapor phase. The dashed curve shows the free energy curve at the neck region lowered by surface energy.  $\bar{G}_b$  is the free energy of component B which is assumed to be constant.  $X_b$  is the composition difference between the neck region and the bulk.

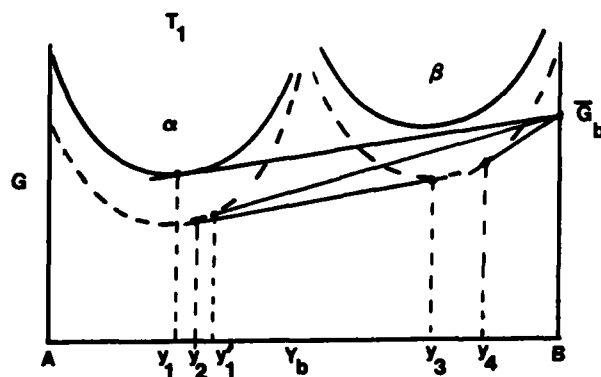


Figure 5.3 Free energy-composition diagram for a system which exhibits a two phase region. The dashed lines correspond to the change in free energy brought about by surface tension in the neck region. As a result, composition  $Y_1$ , originally in the single phase alpha solid solution region is shifted to  $Y_1'$  which is now in the two phase field, and beta will precipitate at the neck.

likely to be of importance in many ceramic systems of technical importance which contain one or more volatile component such as  $\text{LiFe}_5\text{O}_8$  and  $\text{PbZr}_x\text{Ti}_{1-x}\text{O}_3$ . Certainly, it is expected that such vapor transport effects must play a role in any multicomponent ceramic system in which the ambient vapor pressure of one of the species such as  $\text{PbO}$  must be controlled to prevent weight loss and compositional changes. However, no careful study on the precise effects of vapor transport on microstructure development in such systems has been performed.

#### 5.4 Vapor Transport and Third Stage Grain Growth

As discussed above, the mechanism of grain growth in very porous compacts in the initial and intermediate stages of sintering is widely believed to be an Ostwald ripening process via transport down the open pores rather than by grain boundary migration. The exact modeling of this important growth process has not been completely satisfactory as yet nor has it been experimentally verified. However, in the final stages of sintering, when pores are isolated, grain growth takes place by boundary migration and has been well-modeled and studied. In this case, the residual pores and their mobility can have a significant effect on the attainment of high density. As Brook has summarized<sup>29</sup>, the grain boundary velocity can be expressed as the product of a grain boundary mobility,  $M$ , and a driving force,  $F$ :

$$\frac{dG}{dt} = v_b = MF$$

For intrinsic boundary motion limited only by grain boundary diffusion under the driving force of boundary curvature, this gives:

$$G^2 - G_0^2 = K_1 t$$

where  $G$  is the grain size. Impurity segregation, second phases, and pores at grain boundaries all reduce boundary mobility and grain growth rates. As Brook<sup>30</sup> and Carpay<sup>31</sup> have shown for pores moving with a grain boundary:

$$v_b = F_b \frac{M_p M_b}{N M_b + M_p}$$

where  $v_b$  = boundary velocity  
 $F_b$  = force on the boundary  
 $M_b$  = boundary mobility  
 $M_p$  = pore mobility  
 $N$  = number of attached pores per boundary.

Depending on the relative values of the mobilities, either the pores control boundary velocity or the boundary itself does. Pore control is the more interesting case in that as grains grow and porosity decreases, pores are less effective in controlling boundary motion and the boundary may break away from the pores leading to secondary or abnormal grain growth with pores entrapped within the grains. Pore mobility is determined by volume diffusion, surface diffusion, or vapor transport<sup>32,33,34</sup>. If the assumption is made that the grain size is proportional to the pore size<sup>29</sup> then:

$$G^3 - G_0^3 = K_2 t$$

for diffusion through either the vapor or solid phases and

$$G^4 - G_0^4 = K_3 t$$



for surface diffusion. When the pores move with the boundary:

$$v_p = v_b = F_p M_p$$

and the pore mobilities are given by:

$$M_{p,v} = \frac{D_g M \bar{v} p_0}{2\pi r^3 d (RT)^2}$$

for vapor diffusion,

$$M_{p,b} = \frac{D_b \bar{v}}{\pi r^3 RT}$$

for volume diffusion,

$$M_{p,s} = \frac{D_s a \bar{v}}{\pi r^4 RT}$$

for surface diffusion,

where  $D_g$ ,  $D_b$ , and  $D_s$  = gaseous, solid, and

surface diffusion coefficients respectively, and

$a$  = the thickness of the surface diffusion layer.

The maximum force a grain boundary can exert on a pore is<sup>33</sup>  $F = \pi \gamma r$  which in combination with the mobilities leads to the expressions for boundary velocities and  $G(t)$  relations given above.

Although Brook<sup>29</sup> equates the equilibrium partial pressure with the gas pressure in the pore, variation in the equilibrium partial pressure,  $p_0$ , inside the pore can usually be neglected since  $p = p_0(1 - 2\gamma\bar{v}/rRT)$  where  $2\gamma\bar{v}/r$  is the change in free energy due to surface tension. Taking  $\gamma \approx 1000$  ergs/cm,  $\bar{v} \approx 20\text{cm}^3/\text{mole}$ , and  $r \approx 1$  micrometer, at  $T = 1500^\circ\text{C}$ ,  $p \approx p_0(1 - 3 \times 10^{-3})$ .

Clearly, as shown by the above equations, the mobility of pores can be increased by enhanced vapor transport by increasing the equilibrium product gas partial pressure. Figure 5.4, for example, shows that the region for pore-grain boundary separation can be extended to much larger grain and pore sizes in  $\text{Fe}_2\text{O}_3$  in the presence of  $\text{HCl}$  in which the vapor pressure is enhanced through:



Therefore, during the third or final stage of sintering, the tendency for pore-grain boundary separation can be decreased by enhancing pore mobility through increased vapor transport. Therefore, secondary or abnormal grain growth and the attendant pore entrapment can be avoided which allows sintering to a higher density. Thus, in the  $\text{Fe}_2\text{O}_3$  example cited above, sintering in air to about 85% of theoretical density followed by sintering in an atmosphere containing  $\text{HCl}$  can, in principle, retard secondary grain growth and lead to higher densities.

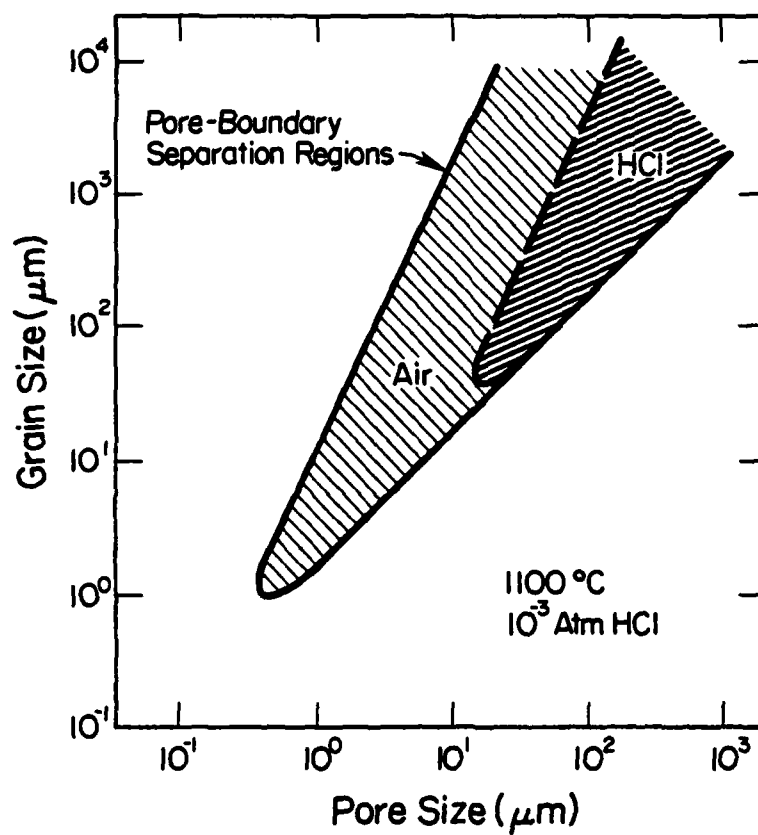


Figure 5.4 Calculated regions of pore-grain boundary separation in  $\text{Fe}_2\text{O}_3$ -air and  $\text{Fe}_2\text{O}_3$ -HCl.

## 5.5 References

1. V. J. Tennery, T. G. Godfrey, and R. A. Potter, J. Am. Ceram. Soc. 54 327 (1971).
2. P. D. Ownby and G. E. Junquist, J. Am. Ceram. Soc. 55 433 (1972).
3. H. F. Priest, G. L. Priest, and G. E. Gazza, J. Am. Ceram. Soc. 60 181 (1977).
4. J. J. Dih and R. M. Fulrath, J. Am. Ceram. Soc. 60 92 (1977).
5. H. U. Anderson, J. Am. Ceram. Soc. 57 34 (1974).
6. R. S. Gordon, p. 231 in Ceramics for Energy Applications, U. S. ERDA Report No. CONF-751194, Nov. 1975.
7. G. C. Kuczynski, Trans. AIME 185 169 (1949).
8. W. D. Kingery and M. Berg, J. Appl. Phys. 26 1205 (1955).
9. T. L. Wilson and P. G. Shewmon, Trans. AIME 236 48 (1966).
10. J. B. Moser and D. H. Whitmore, J. Appl. Phys. 31 488 (1960).
11. L. F. Norris and G. Parravano, J. Am. Ceram. Soc. 46 449 (1963).
12. T. K. Gupta and R. L. Coble, J. Am. Ceram. Soc. 51 521 (1968).
13. Y. Moriyoshi and W. Komatsu, J. Am. Ceram. Soc. 53 671 (1970).
14. A. A. Ammar and D. W. Budworth, Proc. Brit. Ceram. Soc. 12 251 (1969).
15. J. W. Halloran and H. U. Anderson, J. Am. Ceram. Soc. 57 150 (1974).
16. J. M. Neve and R. L. Coble, J. Am. Ceram. Soc. 57 274 (1974).
17. D. R. Stull and H. Prophet, et al., JANAF Thermochemical Tables, 2nd edition (U. S. Govt. Printing Office,

Washington, D. C.), 1971.

18. R. E. Carter, J. Am. Ceram. Soc. 44 116 (1961).
19. D. W. Readey and G. C. Kuczynski, J. Am. Ceram. Soc. 49 26 (1966).
20. N. J. Shaw and A. H. Heuer, Acta Met. 31 55 (1983).
21. C. Greskovich and J. H. Rosolowski, J. Am. Ceram. Soc. 59 336 (1976).
22. C. E. Scott and J. S. Reed, Bull. Am. Ceram. Soc. 58 587 (1979).
23. A. E. Nielsen, Kinetics of Precipitation, (MacMillan, N.Y.), 1964.
24. G. W. Greenwood, Acta Met. 4 243 (1956).
25. I. M. Lifshitz and V. V. Slyozov, J. Phys. Chem. Solids 19 35 (1961).
26. C. Wagner, Z. Electrochem. 65 581 (1961).
27. H. Fischmeister and G. Grimvall, Mater. Sci. Res. 6 119 (1973).
28. G. C. Kuczynski, G. Matsumura, and B. D. Cullity, Acta Met. 8 209 (1960).
29. R. J. Brook, p. 331 in Ceramic Fabrication Processes, F. F. Y. Wang, ed., Vol. 9 in Treatise on Materials Science and Technology, (Academic Press, N. Y.), 1978.
30. R. J. Brook, J. Am. Ceram. Soc. 52 56 (1969).
31. F. M. A. Carpay, J. Am. Ceram. Soc. 60 82 (1977).
32. P. G. Shewmon, Trans. AIME 230 1134 (1964).
33. F. A. Nichols, J. Nucl. Mater. 30 143 (1969).
34. T. R. Anthony and R. A. Sigsbee, Acta Met. 19 1029 (1971).

## 6.0 MICROSTRUCTURE DEVELOPMENT OF $\text{Fe}_2\text{O}_3$ IN HCL VAPOR

### 6.1 Introduction

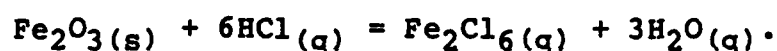
During sintering, particles and pores change size and shape to decrease the interfacial energy of the system. The pores shrink and the grains or particles grow. Since surface energy is the driving force for both processes, their comparative rates determine the densification rate and microstructure evolution. Since the goal of sintering is to obtain a desired microstructure, it is critical to understand the relationship between the two processes of pore shrinkage and grain growth.

The four mass transport mechanisms operative in sintering of crystalline materials are lattice, grain boundary, and surface diffusion, and vapor transport<sup>1,2,3</sup>. The former two produce densification and the latter morphological changes only with no densification. Among these processes, vapor transport is probably the least studied yet is the only mechanism which can be easily controlled by the experimental conditions as discussed in section 5.0 of this report. Thus, enhancing vapor transport permits the observation of controlled microstructure development with the intent of obtaining an improved fundamental understanding of the sintering process rather than an immediate improvement in densification kinetics or final density. This section reports some effects of enhanced vapor transport on microstructure development during the early stages of densification of  $\text{Fe}_2\text{O}_3$  powder compacts.

In the final stage of sintering when pores are isolated,

grain growth takes place by grain boundary migration. Ideally, pores move with grain boundaries. However, when pore mobilities are sufficiently low so that the pores can not keep pace with the moving boundaries, pore separation occurs leading to secondary grain growth and pore entrapment. Since vapor transport is one of the several possible mechanisms for pore migration, increased pore mobility is expected with enhanced vapor transport. Some preliminary results of experiments to enhance pore mobility to retard secondary grain growth by controlling vapor transport are also reported.

Vapor transport can be increased in  $\text{Fe}_2\text{O}_3$  by the introduction of HCl gas to increase the vapor pressure of the product species:



$\text{FeCl}_3$  and  $\text{FeCl}_2$  are also possible vapor species, the vapor pressure of each iron chloride depends on the temperature and water vapor content of the ambient HCl gas. For the above reaction, the equilibrium constant,  $K_e$ , is given by:

$$K_e = \frac{p(\text{Fe}_2\text{Cl}_6) p(\text{H}_2\text{O})^3}{p(\text{HCl})^6}.$$

The equilibrium constant can be calculated from thermodynamic data<sup>4</sup>. Thus, by varying the HCl pressure in the system, the product gas pressures can be calculated and the amount of vapor transport controlled.

## 6.2 Experimental

One of the reasons  $\text{Fe}_2\text{O}_3$  was chosen for investigation was

that the product gas pressures achievable at reasonable temperatures and HCl pressures are quite high ensuring significant enhancement of vapor transport. Another reason was the availability of a relatively pure, nonagglomerated commercial powder (Baker Reagent grade) having an average particle size around 0.2 micrometers.

Pellets 1.4 cm in diameter and approximately 0.3 cm thick were made by pressing in a steel die at 5000 psi to a green density of 48 per cent of theoretical. The pellets were prefired at 500°C for one hour to provide some green strength. After firing at various temperatures and times in different atmospheres, the shrinkage was measured and the microstructure examined. To avoid severe weight loss due to vaporization, samples fired in high HCl pressures were encapsulated in fused silica ampules. The resultant porous samples were impregnated with a lead-borosilicate glass in vacuum to minimize pull-outs during polishing and the polished sections were analyzed quantitatively by semiautomatic image analysis (Zeiss Videoplan). Pore sizes were determined by mercury porosimetry. Helium was used as an inert carrier gas.

For the experiments attempting to increase pore mobility by vapor transport during the final stage of sintering, pellets were first fired in air to 70 to 90 percent of theoretical density before the introduction of HCl vapor. With this procedure it was hoped to introduce the reactant gas before pore closure yet not



so early in densification to prohibit further shrinkage to the closed pore stage.

### 6.3 Results and Discussion

#### 6.3.1 Early stage microstructure development

Shrinkage versus time data are shown in Figure 6.1 as a function of the ambient HCl pressure at 900°C. As expected, as the HCl pressure and the amount of vapor transport increases, densification decreases. For HCl pressures in excess of 0.1 atm, there is no shrinkage at all. However, as Figure 6.2 dramatically shows, the reason for this decrease in densification is due to particle coarsening via vapor transport and not due to neck growth between particles. Figure 6.3 shows a typical polished section used for quantitative microstructure analysis.

Figure 6.4 demonstrates that the particle or grain size grows as the one third power of time in agreement with classical Ostwald ripening by diffusion through the gas phase<sup>5,6,7</sup>. Figure 6.5 gives the ratio of the interparticle neck size to the particle size as a function of time and shows that it remains constant during the times of measurement. This implies that the interparticle necks quickly grow to a steady state ratio and then the entire structure coarsens uniformly. This occurs apparently very rapidly, certainly within the first three minutes of the firing. Since the entire structure coarsens uniformly, it might be expected that the pore size would also coarsen as the one third power of time. Figure 6.6 shows typical pore size distributions obtained by mercury porosimetry. Note the

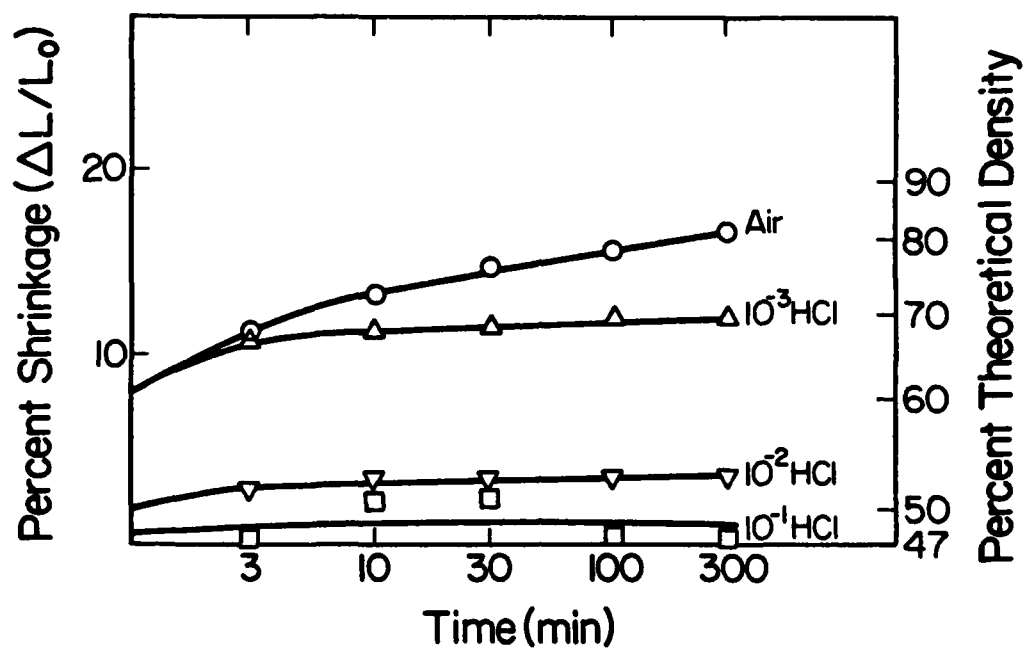


Figure 6.1 Typical shrinkage curves for  $\text{Fe}_2\text{O}_3$ ,  $900^\circ\text{C}$ .



Figure 6.2 Fracture surface of  $\text{Fe}_2\text{O}_3$  sintered at  $1200^\circ\text{C}$  for 5 hours, in air (left) and in 10 percent HCl (right).

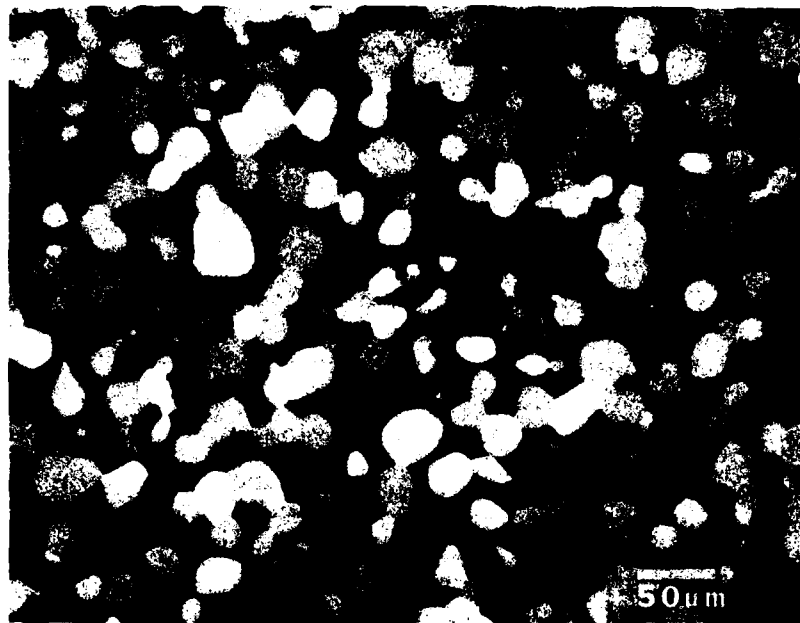


Figure 6.3 Glass encapsulated and polished sample fired at 1200°C for 5 hours in 10 percent HCl, polarized light.

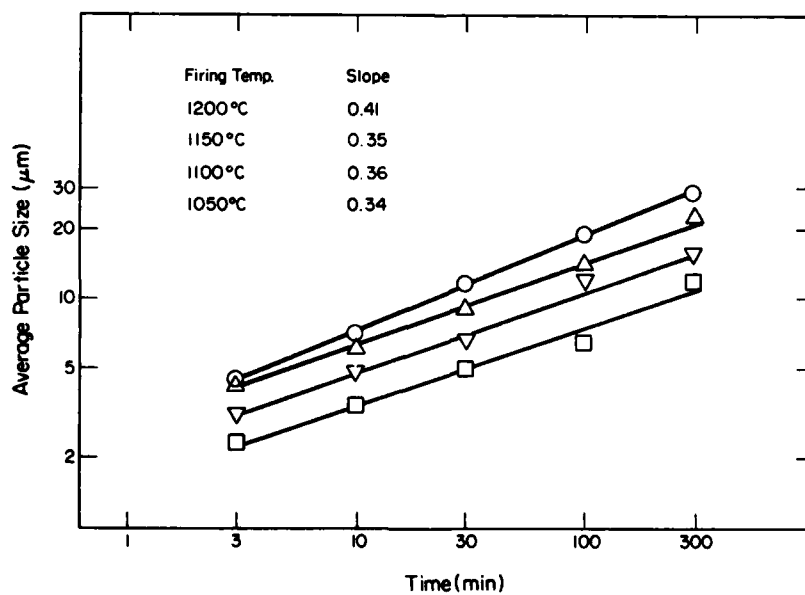


Figure 6.4 Particle size versus time for  $\text{Fe}_2\text{O}_3$  sintered in 10 percent HCl.

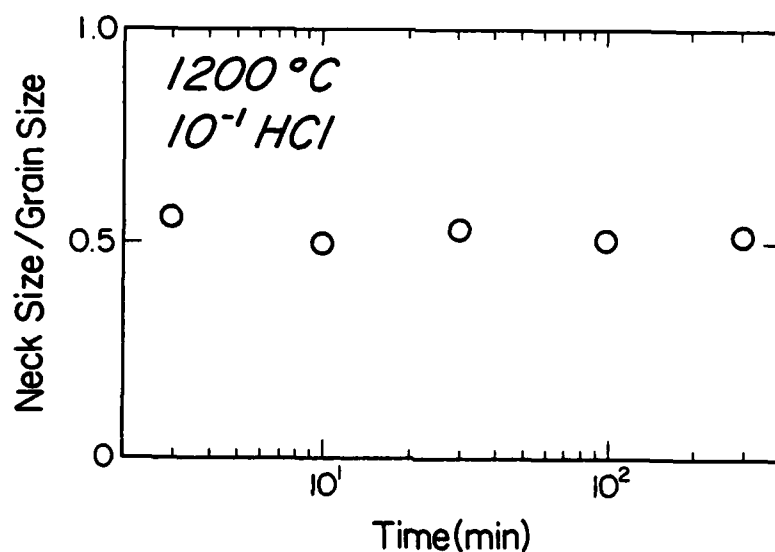


Figure 6.5 Ratio of interparticle neck size to particle size as a function of time.

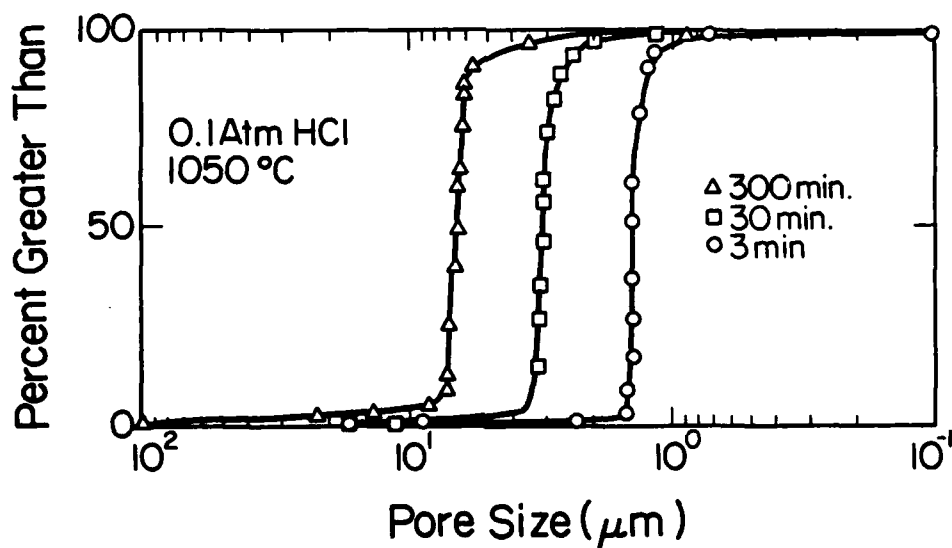


Figure 6.6 Pore size distributions for different firing times obtained by mercury porosimetry.

sharpness of the distributions and the time invariance of the shape. Figure 6.7 illustrates that the average pore size does indeed grow as the one third power of time.

As mentioned above, the one third power dependence of the particle coarsening with time is typical of Ostwald ripening via vapor phase diffusion since:

$$\bar{r}^3 = \frac{8 D \bar{V}^2}{9 (RT)^2} p_o t$$

for diffusion and for an interface controlled reaction:

$$\bar{r}^2 = \left(\frac{8}{9}\right)^2 \frac{K \bar{V}^2}{(RT)^2} p_o t$$

where  $\bar{r}$  = average particle radius  
 $K$  = surface reaction rate constant  
 $\bar{V}$  = molar volume  
 $D$  = gaseous diffusion coefficient  
 $R$  = gas constant  
 $T$  = temperature  
 $p_o$  = equilibrium partial pressure.

In the above equation for Ostwald ripening by diffusion, the only exponentially temperature dependent term is the equilibrium partial pressure of the diffusing gaseous species which in this case is  $\text{FeCl}_2$ ,  $\text{FeCl}_3$ , or  $\text{Fe}_2\text{Cl}_6$ . For the latter,

$$p(\text{Fe}_2\text{Cl}_6) \sim K_e^{-1/4} \sim \exp(-\Delta H^\circ/4RT)$$

if the ambient water vapor pressure in the  $\text{HCl}$  is much lower than that produced in the reaction. If the opposite is true, then

$$p(\text{Fe}_2\text{Cl}_6) \sim K_e \sim \exp(-\Delta H^\circ/RT).$$

This implies that the apparent activation energy for the coarsening process is either  $\Delta H^\circ/4$  or  $\Delta H^\circ$  where  $\Delta H^\circ$  is the standard enthalpy for the reaction. Taking into account all

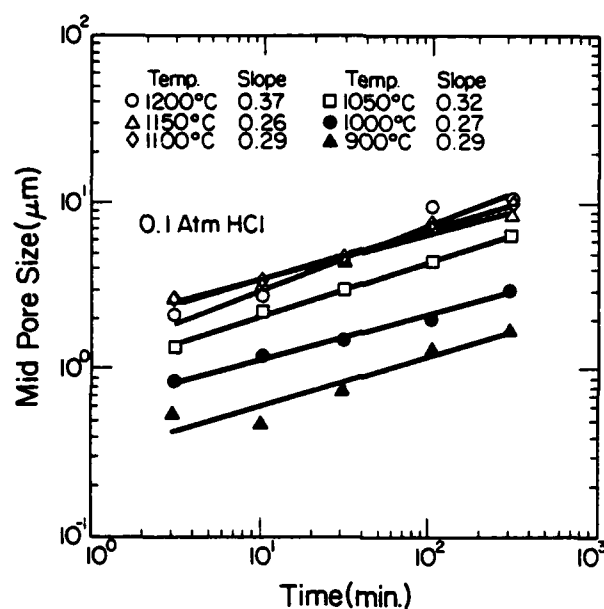


Figure 6.7 Mid pore size versus time showing a one third power dependence.

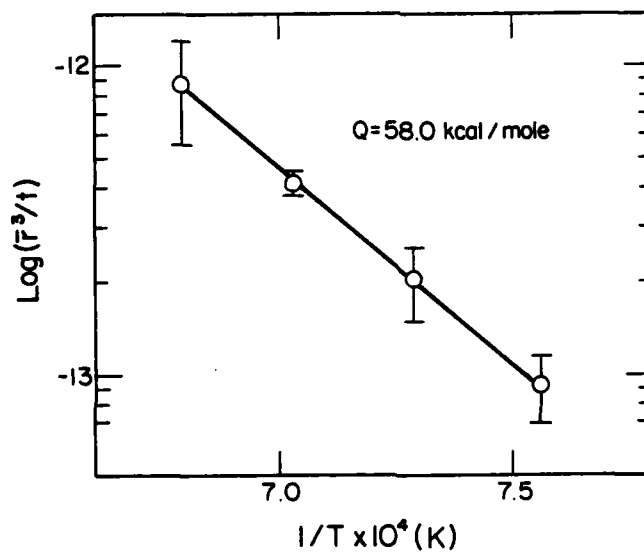


Figure 6.8 Temperature dependence of the rate of particle coarsening in 10 percent HCl with an activation energy larger than that predicted by the gas transport model.

three possible iron chloride gaseous species and both high and low ambient water vapor pressures in the HCl, the predicted activation energy lies between 6 and 24 kilocal/mole<sup>4</sup>. In Figure 6.8 is plotted the temperature dependence of the particle coarsening rate with an apparent activation energy of 58.0 kilocal/mole which is much larger than that expected from tabulated thermodynamic data. As a result, the classical Ostwald ripening model of this coarsening must be questioned. Furthermore, the observed particle size distributions, as shown in Figure 6.9, are strongly skewed to large particles which is completely opposite to that expected from Ostwald ripening theory<sup>5,6,7</sup>. Thus, it must be concluded that some other process with a higher activation energy is controlling particle growth. Specifically, the data tend to indicate that coarsening may be controlled by grain boundary migration even though the major mass transport is via the vapor phase. This is the Greskovich-Lay<sup>8</sup> mechanism which has been proposed to explain grain growth in porous compacts.

One of the advantages of vapor phase transport processes is that all of the parameters of the system, such as the gaseous diffusion coefficient, should be either available in the literature or calculable. This is quite different than transport by solid state diffusion processes for which there is a paucity of reliable diffusion coefficient data for ceramic materials and those which do exist may vary by several orders of magnitude from investigator to investigator. As a result, experimental results

of vapor transport can be quantitatively compared with the models as a further evidence for a rate controlling mechanism far more easily than can solid state diffusion processes. In this case for example, taking  $\gamma \approx 500 \text{ erg/cm}^2$ , and  $D \approx 1 \text{ cm}^2/\text{s}$  the calculated particle size at  $1200^\circ\text{C}$  in pure HCl after 10 minutes is 11 micrometers and that measured, 6 micrometers. This is extremely good agreement considering the approximate values of  $\gamma$  and  $D$  used and the uncertainties in the model. Nevertheless, it reinforces the argument that gaseous diffusion is the major mass transport process leading to particle growth while grain boundary migration may be rate controlling.

### 6.3.2 Final stage sintering

When the pores move with the boundary, the pore velocity,  $v_p$ , and the grain boundary velocity,  $v_b$ , are the same<sup>9,10,11</sup> and are determined by the force on the pore,  $F_p$ , caused by the boundary curvature and the pore mobility,  $M_p$ <sup>12,13,14</sup>:

$$v_p = v_b = F_p M_p.$$

The pore mobilities are given by:

$$M_{p,v} = \frac{D_g M \bar{v} p_0}{2\pi r^3 d (RT)^2}$$

for vapor diffusion,

$$M_{p,b} = \frac{D_b \bar{v}}{\pi r^3 RT}$$

for volume diffusion,



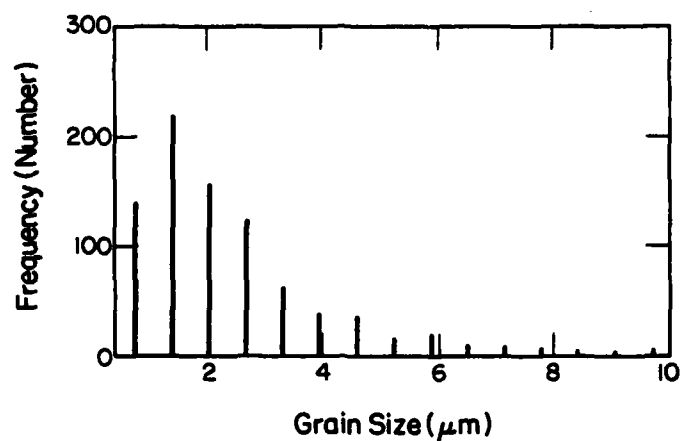


Figure 6.9 Typical particle size distribution, 5 hours at 1050°C in 10 percent HCl.

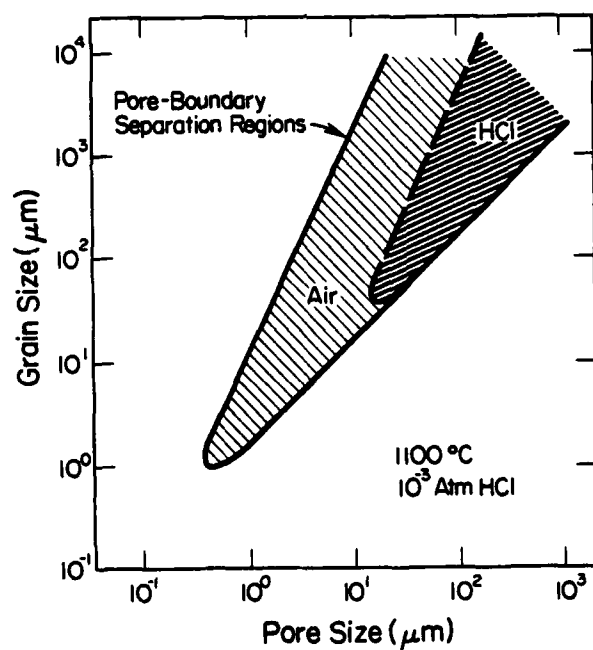


Figure 6.10 Calculated grain-pore size plot showing pore, grain boundary separation in both air and HCl.

$$M_{p,s} = \frac{D_s a \bar{v}}{\pi r^4 RT}$$

for surface diffusion where  $D_g$ ,  $D_b$ , and  $D_s$  = gaseous, solid, and surface diffusion coefficients respectively,  $a$  = the thickness of the surface diffusion layer,  $r$  = the pore radius, and  $M$  = the molecular weight.

Comparing pore mobilities for vapor transport and volume diffusion at 1400°C by taking  $D_b = 1.5 \times 10^{-10} \text{ cm}^2/\text{s}$ <sup>17</sup> and  $D_g = 1 \text{ cm}^2/\text{s}$ ,  $M_{p,v}/M_{p,b} = 4.4$  for an HCl pressure of  $10^{-4}$  atm. Therefore, for any HCl pressure greater than this, pore mobility should be greatly enhanced and secondary grain growth retarded. Figure 6.10 is the calculated pore-grain boundary stability diagram after Brook<sup>9</sup> in  $10^{-3}$  atm. HCl showing that secondary grain growth should be retarded by enhanced vapor transport.

However, the theoretical prediction was not verified by experiment. Secondary grain growth could not be retarded with HCl pressures up to  $10^{-2}$  atm if it were added at fired densities between 70 and 90 percent of theoretical. The reason for the lack of grain growth retardation is not clear at present.

Two very interesting observations were made however. First,  $10^{-3}$  and  $10^{-2}$  atm HCl pressures had no affect on retarding densification when added at 85 percent of theoretical density as shown in Figure 6.11 which should be contrasted with the data in Figure 6.1 which shows that these HCl pressures inhibited densification if added at the start of sintering. Second, the major factor affecting the occurrence of secondary grain growth,

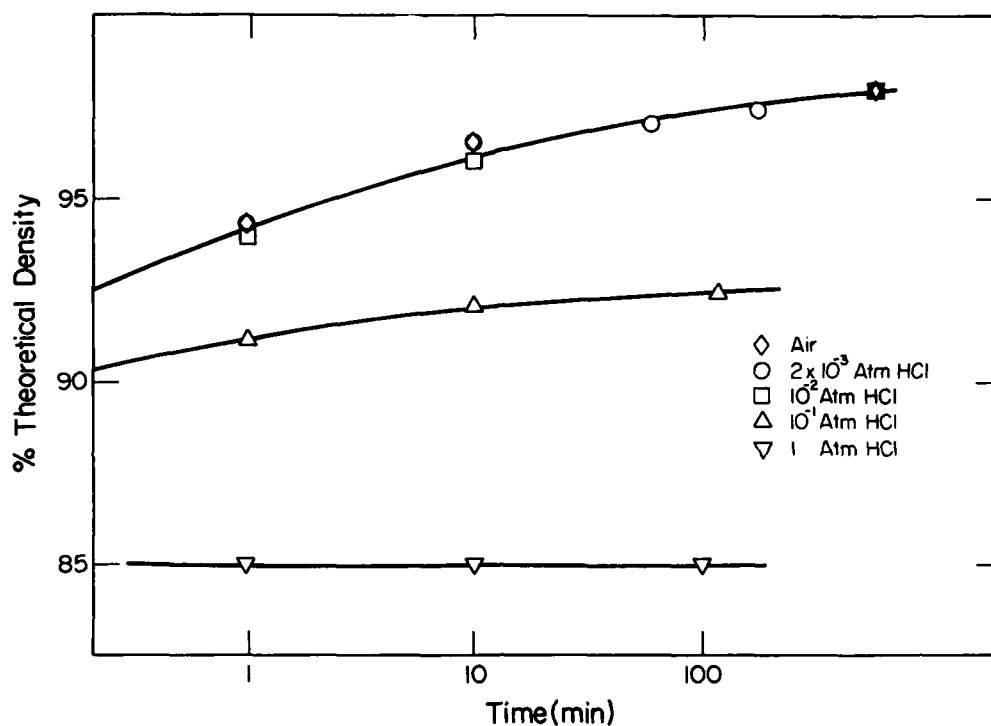


Figure 6.11 Density versus time plots after initially firing in air to 85 percent density at 1050°C for one hour.

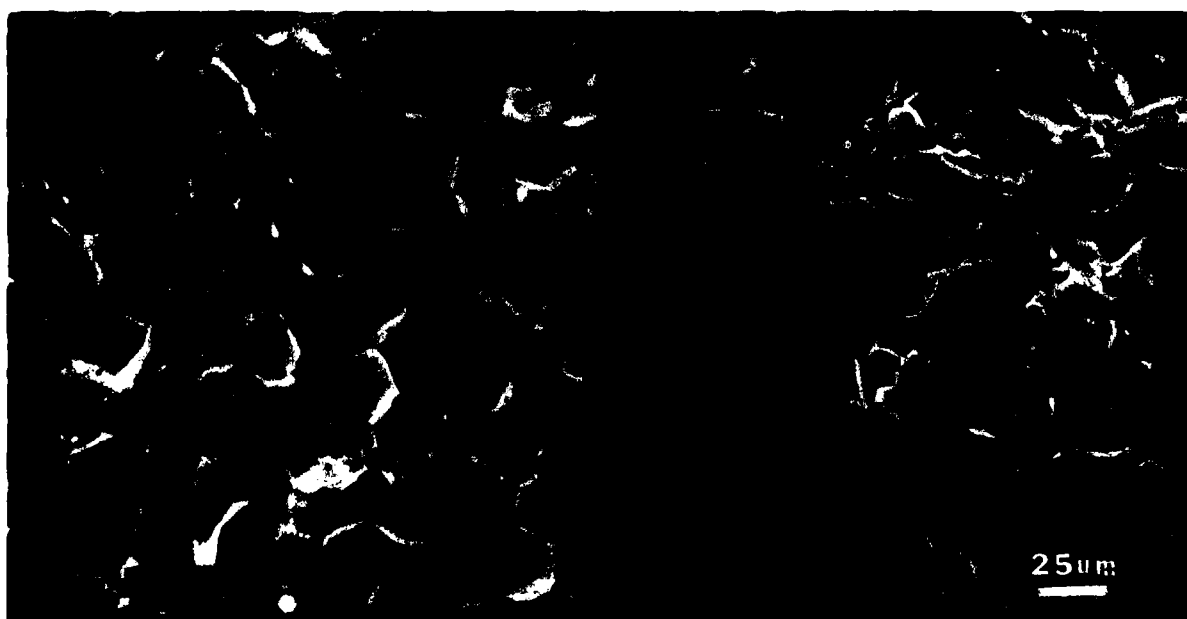


Figure 6.12  $\text{Fe}_2\text{O}_3$  samples fired in air for 15 hours at 1200°C, left 51 percent and right 48 percent green density.

regardless of the atmosphere, was the green density of the compact. Figure 6.12 shows a micrograph of a sample with a green density of 48 percent exhibiting secondary grain growth in contrast with a sample of 51 percent green density showing no secondary grain growth. Fifty percent seemed to be about the critical green density below which secondary grain growth always occurred. Why the initial green density is so critical is not known but certainly must be related to the densification path in grain size-density space.

#### 6.4 Summary and Conclusions

1. Vapor phase transport of  $\text{Fe}_2\text{O}_3$  is enhanced in HCl vapor.
2. Vapor transport of  $\text{Fe}_2\text{O}_3$  retards sintering primarily by particle coarsening.
3. The entire microstructure coarsens uniformly.
4. Both the particle size and the pore size follow a one third power dependence on time.
5. Pore size distributions are very narrow.
6. Grain boundary motion controls the rate of particle coarsening.
7. Secondary grain growth could not be eliminated by enhancing vapor transport during the final stage of sintering.
8. Enhanced vapor transport was far less effective in limiting densification kinetics during the later stages of sintering.
9. Green density has a significant effect on the final microstructure with green densities less than 50 percent of theoretical leading to secondary grain growth.

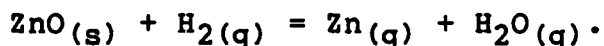
## 6.5 References

1. G. C. Kuczynski, Trans. AIME 105 169 (1949).
2. W. D. Kingery and M. Berg, J. Appl. Phys. 26 1205 (1955).
3. R. L. Coble and R. M. Cannon, p. 291 in Vol.11 of Materials Science Research Processing of Crystalline Ceramics, (Plenum, N. Y.), 1978.
4. D. R. Stull and H. Prophet, et al., JANF Thermochemical Tables, 2nd edition (U. S. Govt. Printing Office, Washington, D. C.), 1971.
5. G. W. Greenwood, Acta Met. 4 243 (1956).
6. I. M. Lifshitz and V. V. Slyozov, J. Phys. Chem. Solids 19 35 (1961).
7. C. Wagner, Z Electrochem. 65 581 (1961).
8. C. Greskovich and K. W. Lay, J. Am. Ceram. Soc. 55 142 (1972).
9. R. J. Brook, p. 331 in Ceramic Fabrication Processes, F. F. Y. Wang, ed., Vol. 9 in Treatise on Materials Science and Technology, (Academic Press, N. Y.), 1978.
10. R. J. Brook, J. Am. Ceram. Soc. 52 56 (1969).
11. F. M. A. Carpay, J. Am. Ceram. Soc. 60 82 (1977).
12. P. G. Shewmon, Trans. AIME 230 1134 (1964).
13. F. A. Nichols, J. Nucl. Maters. 30 143 (1969).
14. T. R. Anthony and R. A. Sigsbee, Acta Met. 19 1029 (1971).
15. V. I. Izvekov, et al, Phys. Metals and Metallog. 14 30 (1962).

## 7. MICROSTRUCTURE DEVELOPMENT OF ZnO IN HYDROGEN

### 7.1 Introduction

As discussed earlier, vapor transport can be significantly enhanced by the sintering atmosphere. Zinc oxide in hydrogen was chosen as a model system to study because rather significant vapor pressures of the product gas species can be generated by the following reaction:



Furthermore, the thermodynamic data are reasonably well-documented<sup>1</sup> and give for the above reaction,

$\Delta H^\circ = 113 \text{ kJ/mole}$  ( $27 \text{ kcal/mole}$ ). The equilibrium constant is given by:

$$K_e = \frac{P(\text{Zn}) P(\text{H}_2\text{O})}{P(\text{H}_2) a(\text{ZnO})}.$$

In dry hydrogen, in which  $P(\text{H}_2\text{O})$  from the reaction is significantly greater than the water vapor in the ambient gas, for unit activity of ZnO ( $a(\text{ZnO}) = 1$ ), then  $P(\text{ZnO}) \approx P(\text{H}_2\text{O})$  and:

$$P(\text{Zn}) = P(\text{H}_2)^{1/2} K_1 \exp(-\Delta H^\circ/2RT)$$

where  $K_1$  is the entropy term. On the other hand, if the ambient water vapor content is high, then  $P(\text{Zn}) \ll P(\text{H}_2\text{O})$  and:

$$P(\text{Zn}) = P(\text{H}_2\text{O})^{-1/2} P(\text{H}_2)^{1/2} K_1^2 \exp(-\Delta H^\circ/RT).$$

In the experiments reported here, the calculated zinc pressures were in the range of 0.01 MPa to 0.03 MPa (0.1 to 0.3 atm) and much larger than the ambient water vapor pressures in the gas stream.

## 7.2 Experimental

### 7.2.1 Powder preparation

Mallinckrodt reagent grade zinc oxide powder was used for this study. The powder was badly agglomerated as observed by microscopy and as seen in Figure 7.1. The particle size distribution of the untreated powder as determined by semiautomatic image analysis with a Zeiss "Videoplan"<sup>2</sup> is shown in Figure 7.2. This zinc oxide was centrifugally sedimented to produce a narrow and small particle (agglomerate) size range suitable for sintering studies. A solution of 70% water and 30% acetone was used as the sedimentation fluid. Darvon C was used to disperse the powder in the solution. Stokes law was used to calculate the time for the maximum desired particle size to settle. The slurry was well-dispersed with a blender and allowed to stand until the largest size should have settled from the top of the vessel. The remaining slurry was syphoned off and centrifuged in a Beckman J2-21 centrifuge to settle the powder. The powder was again dispersed and washed twice in double distilled water and dried. The resulting particle size is shown in Figure 7.3. As can be seen, there is a considerable decrease in the average particle size and the distribution is reasonably narrow.

The zinc oxide plus alumina samples were prepared by mixing previously sedimented alumina (Alcoa A-16) to give a small

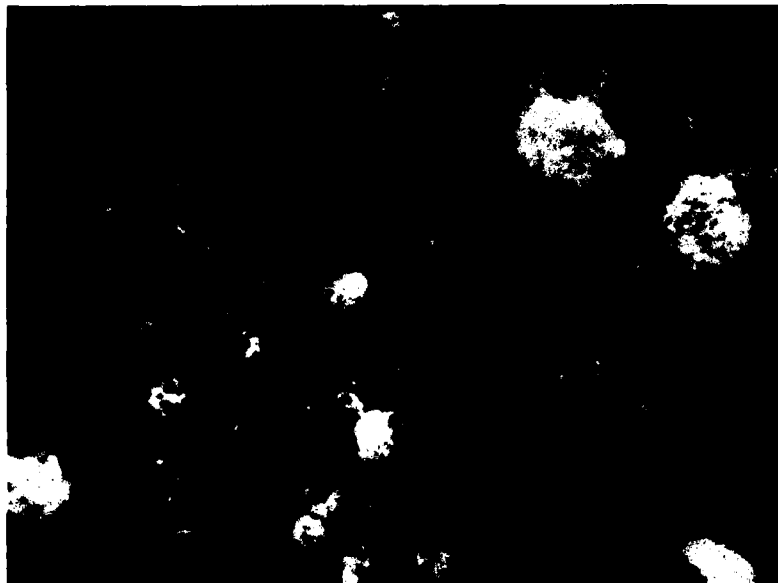


Figure 7.1 As-recieved agglomerated ZnO Powder. 1000X

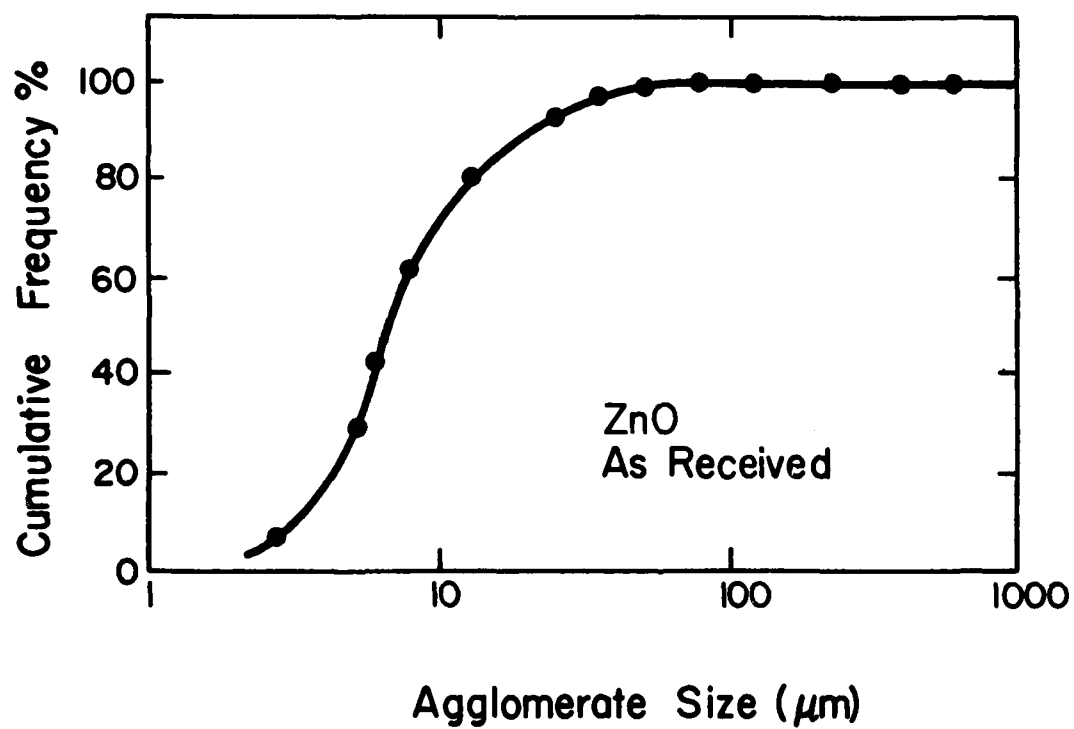


Figure 7.2 Agglomerate size distribution of as-received ZnO powder.



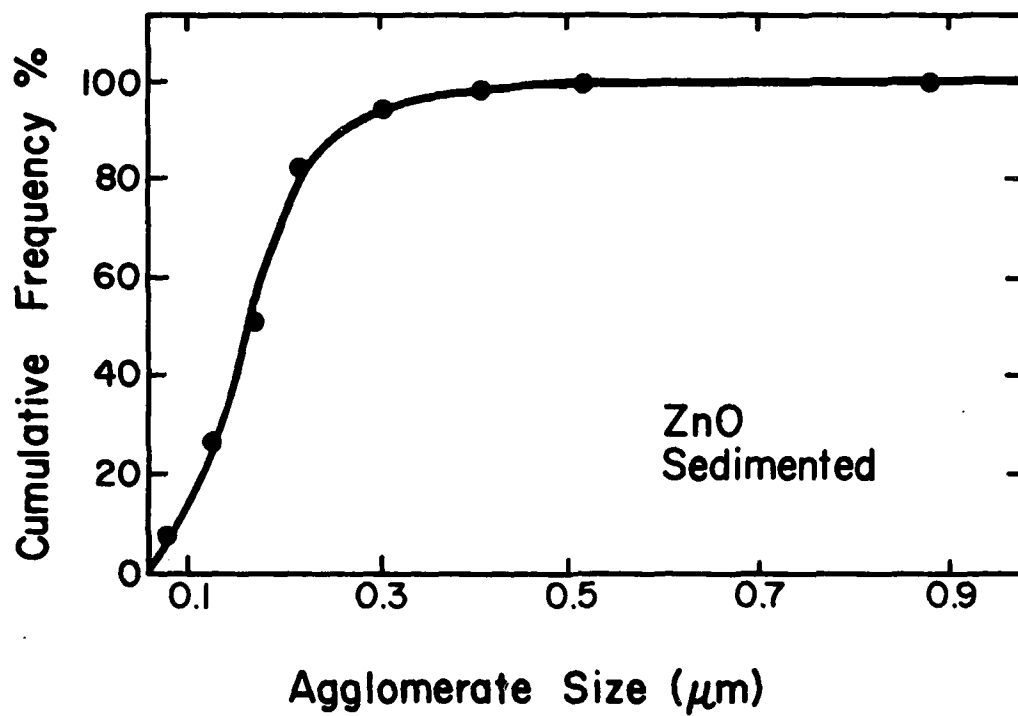


Figure 7.3 Agglomerate size distribution of ZnO powder after centrifuging and typical of that used in this study.

particle size (~0.1 micrometer) and then adding it to the previously sedimented zinc oxide in the acetone/water solution and allowing the slurry to dry.

#### 7.2.2 Sample preparation

Pellets 1.4 cm in diameter were pressed at 70 MN/m<sup>2</sup> (10,000 psi) in a steel die to 61 percent of theoretical density. The pellets were then prefired in air at about 500°C for 1 1/2 hours to burn off the oil used to lubricate the steel pressing die. The pellet dimensions were measured with a micrometer and used for calculating the green density and for subsequent shrinkage measurements. After preparation, all pellets were kept in a drier at 150°C to minimize moisture pickup.

Pellets were placed into fused silica ampules for controlled-atmosphere heat treatment. The ampules had an inside diameter of 2.54 cm and typically were 13.4 cm long. The pellets rested on a piece of platinum foil inside the ampules to minimize reaction between the ZnO and the fused silica. The ampule was then evacuated and dried by heating to about 175°C until a dew point in the neighborhood of -30°C ( $p(\text{H}_2\text{O}) = 3.8 \times 10^{-4}$  atm or 38 Pa) was reached as determined with a Panametrics 700 electronic hygrometer. Dry hydrogen-helium mixtures were then let into the tube at about one third of an atmosphere. The hydrogen/helium ratio was determined by the relative flow rates of the two gases. The dew point in the gas-filled ampule never exceeded -30°C. The filled ampule was then sealed with a torch.

AD-A145 753

CERAMIC MICROSTRUCTURE DEVELOPMENT(U) OHIO STATE UNIV  
COLUMBUS DEPT OF CERAMIC ENGINEERING D W READEY AUG 84  
N00014-80-C-0523

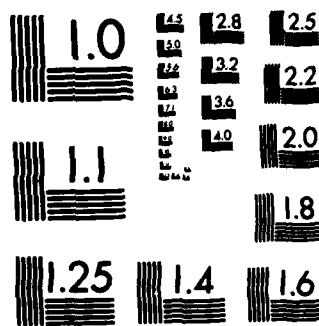
2/2

UNCLASSIFIED

F/G 11/2

NL


END  
FILMED  
DTIC



MICROCOPY RESOLUTION TEST CHART

### 7.2.3 Sintering and microstructure analysis

The ampules were fired between 950°C and 1200°C for varying times. After firing, each ampule was removed and the sample dimensions measured to determine the shrinkage. The amount of hydrogen that could diffuse out of the ampules was calculated from literature data<sup>3</sup> to be no more than 1.8 percent.

The fracture surfaces of the pellets were examined with scanning electron micrographs and the microstructures analyzed quantitatively with the image analyzer. At least two representative areas in the sample were selected for photomicrographs. A minimum of 250-300 grains or particles per sample were measured to obtain a mean grain size and grain size distribution. It should be noted that polished and thermally-etched samples gave misleading results in that ZnO is apparently sufficiently plastic that all surface porosity is filled during polishing and the surface "recrystallizes" upon thermal etching.

## 7.3 Results and Discussion

### 7.3.1 General

Figures 7.4, 7.5, and 7.6 clearly show that enhancing vapor transport with hydrogen decreases the densification and its rate as predicted by theory<sup>4,5</sup> which predicts enhanced neck growth via vapor transport. However Figure 7.7 dramatically demonstrates that the major microstructural change with the enhanced vapor transport is particle or grain coarsening and not simply neck growth. The rate of coarsening increases with increasing hydrogen pressure and correlates with the decrease in

sintering rate and final density. Thus, rapid particle coarsening is the principal factor in reducing densification. Figure 7.8 shows the same effect at 1150°C and the dramatic difference in particle size between the samples fired in air and hydrogen.

### 7.3.2 Rate of particle growth

Figure 7.9 gives the rate of particle growth as a function of time. The average slope of all the log grain size-log time plots is very close to one third as predicted by classical Ostwald ripening theory<sup>6,7,8</sup>. For the case in which particle growth is being controlled by gaseous diffusion, the theory<sup>8</sup> predicts that the average particle size,  $\bar{r}$ , should vary as:

$$\bar{r}^3 - \bar{r}_0^3 = \frac{8}{9} \frac{D_g \gamma}{d^2} \left( \frac{M}{RT} \right)^2 P(Zn) t$$

where  $D_g$  = gaseous diffusion coefficient  
 $d$  = solid density  
 $M$  = molecular weight  
 $\gamma$  = surface energy  
 $t$  = time  
 and  $R$  and  $T$  have their usual meaning.

or the particle size should increase as the one third power of time as observed experimentally. Furthermore, since the particle size varies as  $P(Zn)^{1/3}$  and  $P(Zn)$  varies as  $P(H_2)^{1/2}$  in very dry hydrogen, as shown above, the average particle size at any given time and temperature should vary as  $P(H_2)^{1/6}$ . Figure 7.10 gives an exponent of  $0.1 \pm 0.07$  which is close to the expected value.

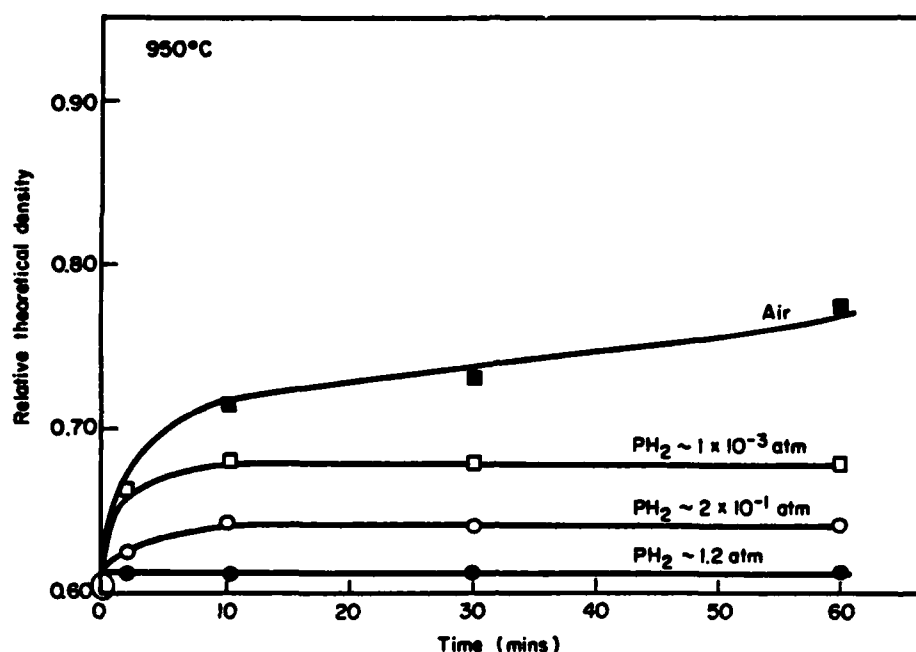


Figure 7.4 Effect of hydrogen content of the atmosphere on the relative density versus time for ZnO sintered at 950°C.

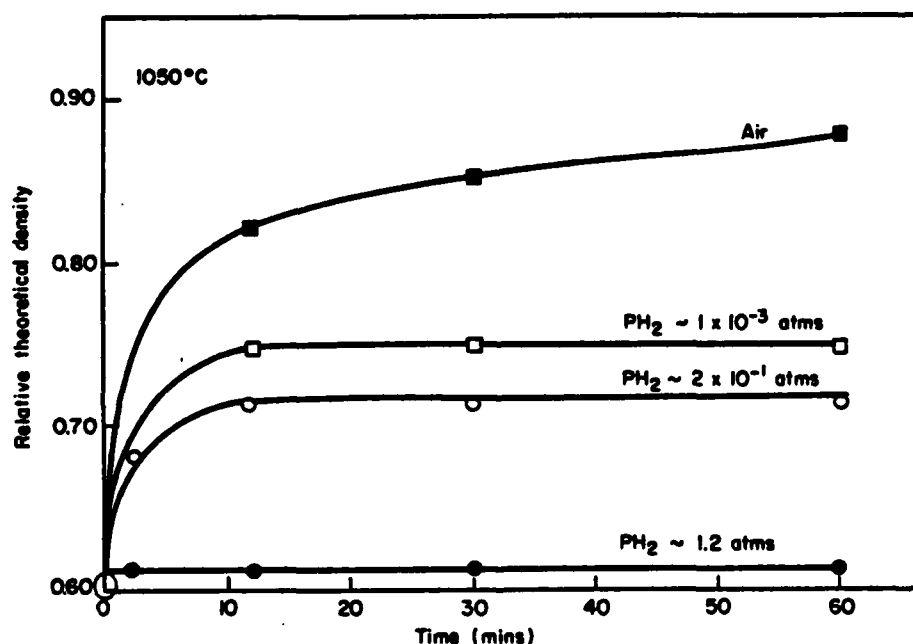


Figure 7.5 Effect of hydrogen content of the atmosphere on the relative density versus time for ZnO sintered at 1050°C.

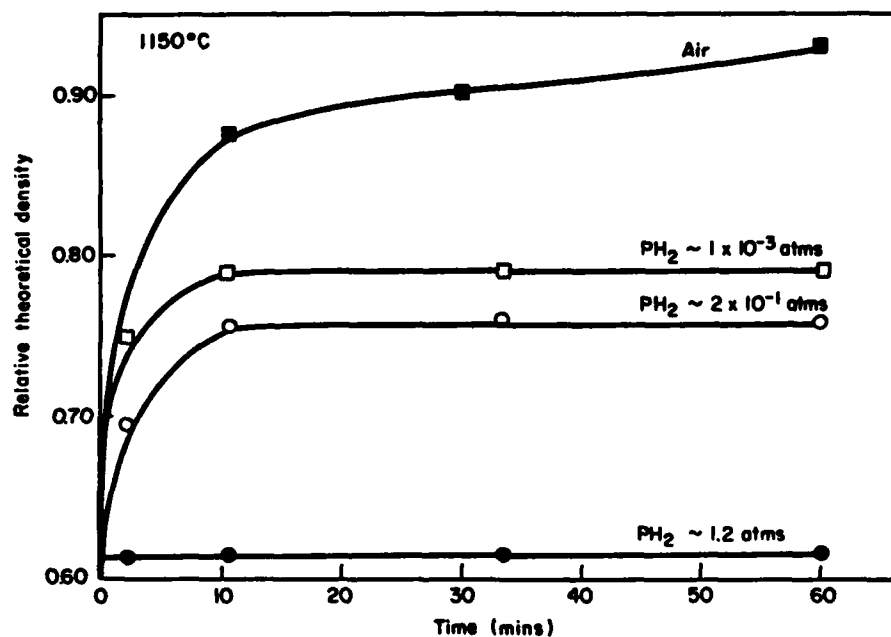


Figure 7.6 Effect of hydrogen content of the atmosphere on the relative density versus time for ZnO sintered at 1150°C.

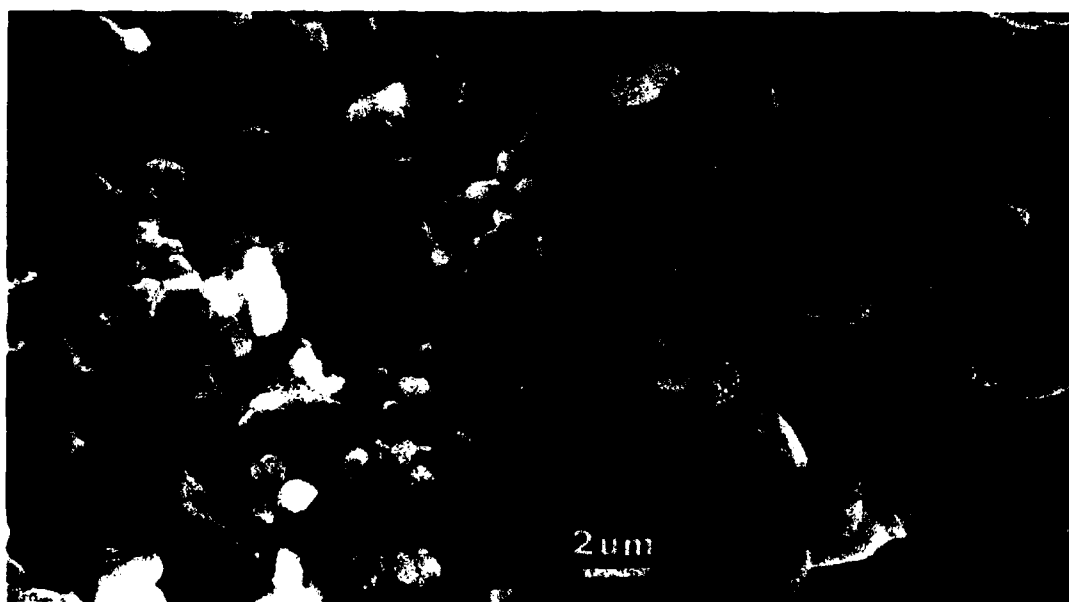


Figure 7.7 Effect of hydrogen pressure on grain size of ZnO sintered at 1040°C for 60 minutes. Left: air. Right: one atmosphere hydrogen.





Figure 7.8 Effect of hydrogen pressure on grain size of ZnO sintered at 1150°C for 6 minutes. Left: air. Right: one atmosphere hydrogen.

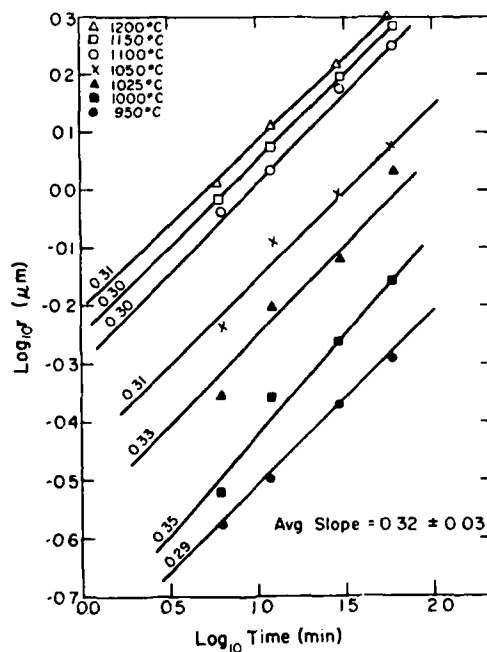


Figure 7.9 Log-log plot of the average particle size versus time for all the temperatures studied showing a  $t^{1/3}$  dependence.

As discussed earlier,  $P(\text{Zn}) \sim \exp(-\Delta H^0/2RT)$  in dry hydrogen and  $P(\text{Zn}) \sim \exp(-\Delta H^0/RT)$  in wet hydrogen. In the above equation for particle coarsening, the only strongly temperature dependent term is  $P(\text{Zn})$ . Therefore, since  $\bar{r} \sim P(\text{Zn})^{1/3}$ , the apparent activation energy for particle growth should be  $\Delta H^0/6$  or  $\Delta H^0/3$  in dry and wet hydrogen respectively, ie. 18.8 kJ/mole (4.5 kcal/mole) and 37.6 kJ/mole (9 kcal/mole). As Figure 7.11 shows, above about 1100°C, the apparent activation energy is indeed 18.8 kJ/mole (4.5 kcal/mole) as predicted for the dry hydrogen used in these experiments. However, at lower temperatures, an apparent activation energy of 109 kJ/mole (26 kcal/mole) is observed which is much higher than that predicted by theory strongly suggesting that another mechanism of particle growth is rate-controlling. The classical theory of ripening predicts that  $\bar{r}$  should be proportional to  $t^{1/2}$  if a surface reaction is rate controlling<sup>8</sup>. However, the data indicate a  $t^{1/3}$  dependence at all temperatures. If the rate-limiting step at low temperatures is grain boundary motion between the particles, however, then:

$$\bar{r}^3 \sim \exp(-Q/RT)$$

where  $Q$  is the activation energy for grain boundary motion. The experimental value of 326 kJ/mole (78 kcal/mole) is close to that obtained for grain growth in dense polycrystalline  $\text{ZnO}$ <sup>9,10,11</sup>.

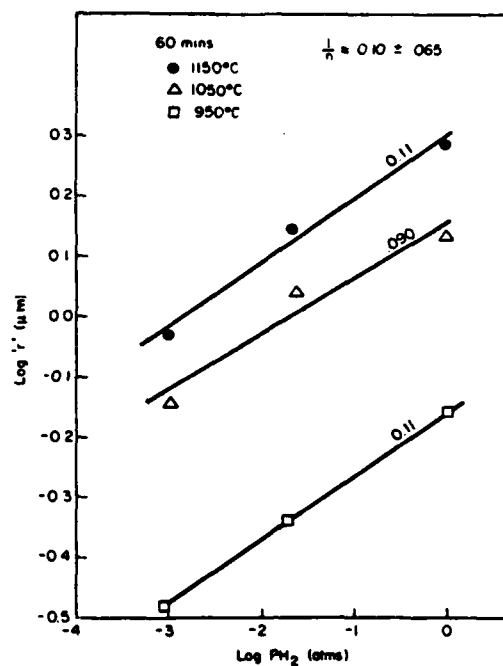


Figure 7.10 Log-log plot of average particle size versus the hydrogen pressure.

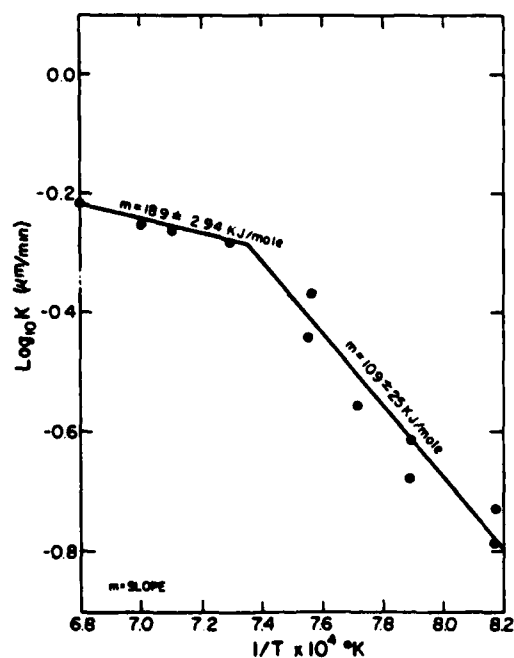


Figure 7.11 Temperature dependence of the rate of particle growth showing two different activation energies.

### 7.3.3 Grain growth in dense zinc oxide in air

In order to ensure that grain growth rates in both the porous and dense zinc oxide were being compared on the same material, grain growth studies were carried out on dense ZnO in air. Grain growth was carried out on samples previously fired to 96 percent of theoretical density at 1000°C for 2 1/2 hours in air. Figure 7.12 shows a typical microstructure used for grain size measurement and Figure 7.13 shows a typical grain size distribution. Figure 7.14 shows that the observed grain size dependence on time was a one third dependence; namely,

$$D^3 - D_0^3 = K e^{-Q/RT} t$$

where D = grain diameter at time t,

$D_0$  = initial grain diameter

Q = activation energy for grain growth.

The activation energy as obtained from the temperature dependence of the slopes of the plots in Figure 7.14 and determined from Figure 7.15 is 284 (±11) kJ/mole (68 kcal/mole). This agrees well with the activation energy for grain growth in ZnO as determined by others<sup>9,10,11</sup>. Furthermore, it agrees extremely well with the activation energy determined from the vapor transport experiments. Typical particle size distributions in Figure 7.13 are skewed to smaller particle sizes and are nearly lognormal which is typical for grain growth in dense materials. It should be noted that the distributions have reached steady state since their shapes do not change with time and are essentially constant after 30 minutes.

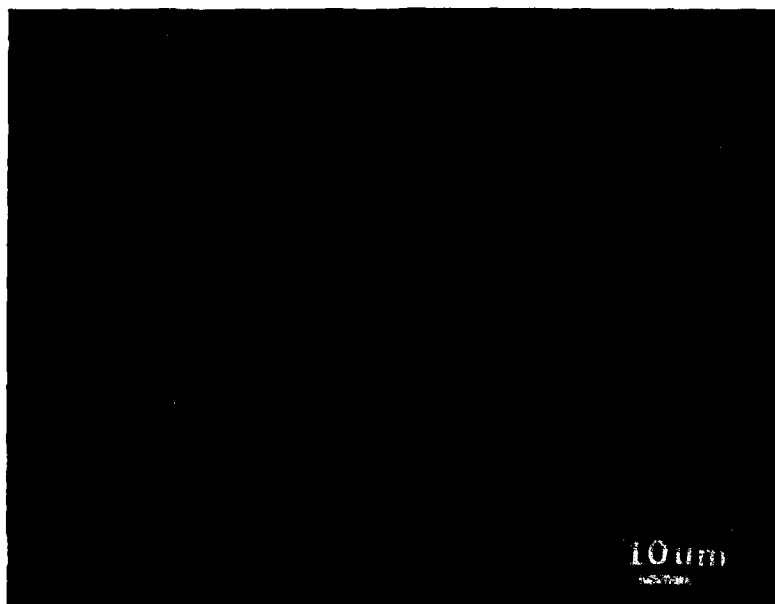


Figure 7.12 Typical microstructure of dense ZnO used for grain growth studies in air.

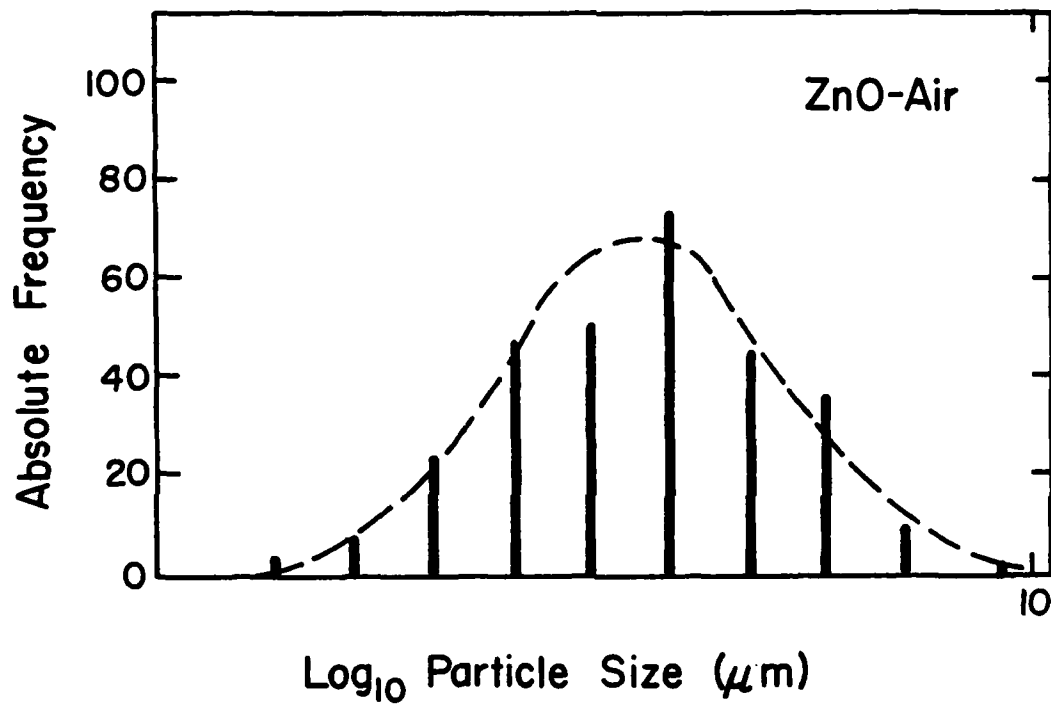


Figure 7.13 Grain size distribution in dense polycrystalline ZnO used for grain growth experiments in air, 1000°C.

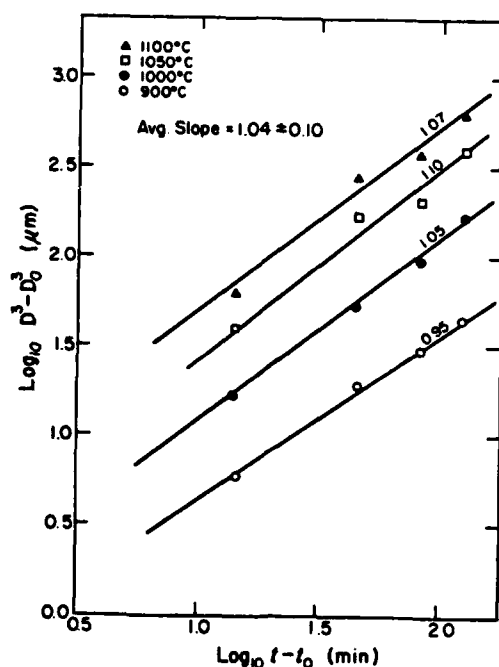


Figure 7.14 Log-log plot of  $D^3 - D_0^3$  versus time showing an essentially linear relation.

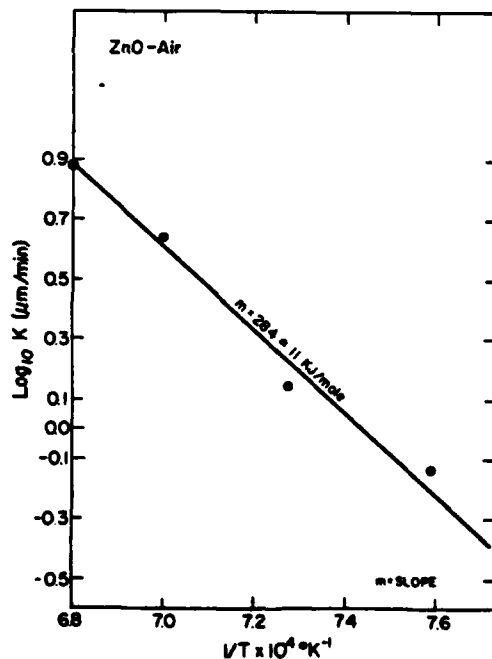


Figure 7.15 Temperature dependence of the grain growth rate in air in dense ZnO giving an activation energy of 284 kJ/mole (68 kcal/mole).

Although the skewness of these grain growth curves are similar to those for the modified LSW theories<sup>12,13</sup>, these theories are really valid neither for particles in contact nor at one hundred percent volume fraction. On the other hand, such distributions are typical of those obtained in grain growth studies<sup>14</sup>.

These results reinforce the concept that the rate of grain growth is determined by the rate of grain boundary motion in the porous samples as well. This suggests that the Greskovich-Lay<sup>15</sup> mechanism of particle coarsening is operative in ZnO in hydrogen. The model of this mechanism is sketched in Figure 7.16. More specifically, in hydrogen, the major mass transport mechanism for particle growth is doubtlessly vapor transport which produces the exaggerated particle growth rates. However, vapor transport is the fast process. In order for particle growth to occur, grain boundaries between the particles must move. It is this boundary movement that limits grain growth. The major evidence for this is: 1.) the particle size at any given time is smaller than that predicted by Ostwald ripening via vapor transport alone; 2.) the particle size distributions tend to be lognormal or skewed just the opposite to those predicted by ripening theory, similar to that observed in normal grain growth; and most important, 3.) the activation energy for particle coarsening in the porous compacts is much higher than that expected from vapor transport and very similar to that obtained in grain growth studies with dense ZnO in air.



#### 7.3.4 Effect of alumina on coarsening

Since the evidence strongly suggested that the Greskovich-Lay<sup>15</sup> mechanism of particle coarsening was operative in the ZnO fired in hydrogen with the rate of grain boundary migration determining the rate of particle coarsening, the effect of Al<sub>2</sub>O<sub>3</sub> additions was studied. It was expected that the added alumina would form ZnAl<sub>2</sub>O<sub>4</sub> as a second phase<sup>16</sup> which would retard particle coarsening if grain boundary motion is indeed rate controlling. Additions of 0.5 m/o, 1.0 m/o, and 5 m/o alumina were made to ZnO powders as described earlier. These compositions were chosen since the phase diagram in the literature indicated that they were in the two-phase field of ZnO and ZnAl<sub>2</sub>O<sub>4</sub><sup>16</sup>.

Figure 7.17 shows a fracture surface which shows the presence of second phase particles at grain boundaries. These were thought to be ZnAl<sub>2</sub>O<sub>4</sub> particles since x-ray diffraction patterns taken on the 5 m/o ZnO samples clearly show the presence of the spinel phase as shown in Figure 7.18.

Figure 7.19 shows the grain size as a function of time for 1 m/o Al<sub>2</sub>O<sub>3</sub>. The particle size time dependence remains one third as in the case of the pure ZnO. Furthermore, the grain size distributions at 1150°C shown in Figure 7.20 have reached steady state at thirty minutes and the shape is the same as that for the pure ZnO distributions (Figure 7.13). Similarly, the material with the 5 m/o alumina shows the same behavior as seen in Figure

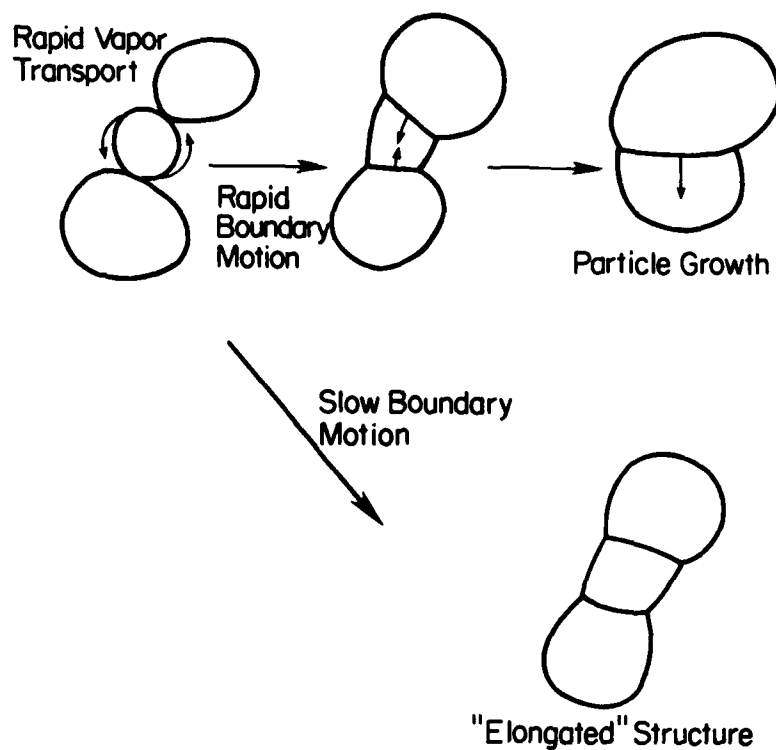


Figure 7.16 Schematic representation of the Greskovich-Lay mechanism of particle coarsening in a porous powder compact<sup>15</sup>.



Figure 7.17 Fracture surface of  $\text{ZnO}$  with 1 m/o  $\text{Al}_2\text{O}_3$  addition fired in hydrogen at  $1100^\circ\text{C}$  for 60 minutes showing second phase of  $\text{ZnAl}_2\text{O}_4$  at grain boundaries (arrow).

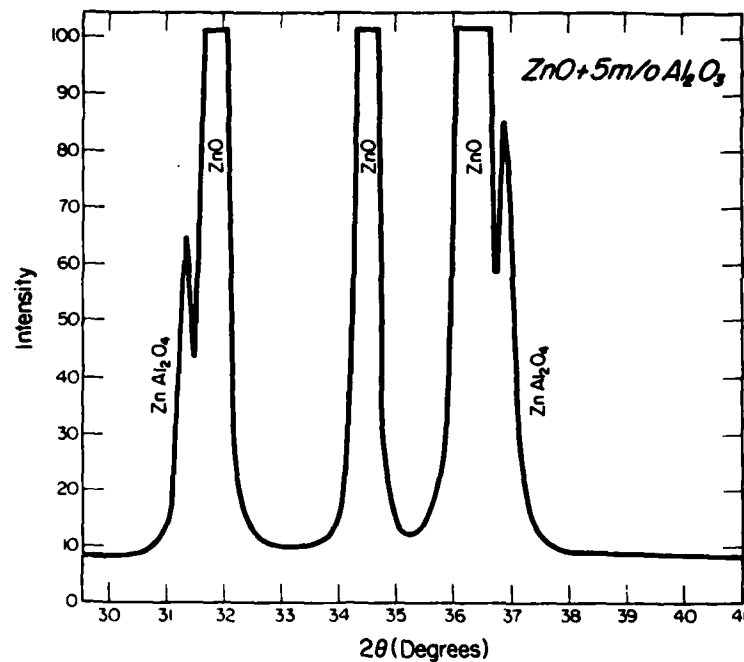


Figure 7.18 Part of the x-ray diffraction pattern of the 5 m/o  $Al_2O_3$  sample showing the presence of  $ZnAl_2O_4$  as a second phase.

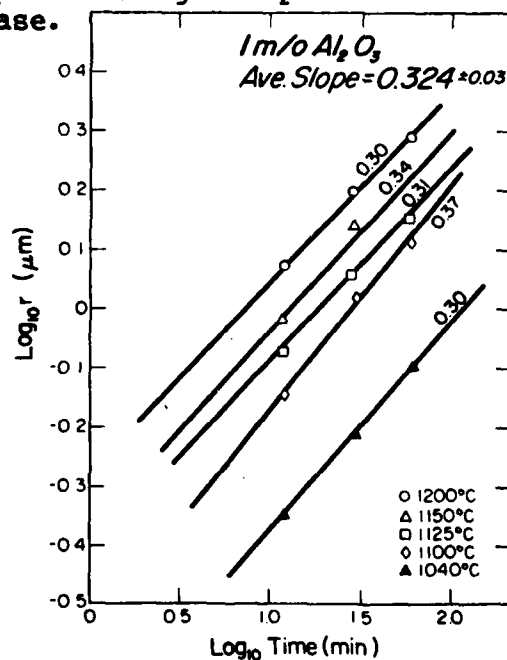


Figure 7.19 Log-log plot of the particle size versus time for the 1 m/o  $Al_2O_3$  samples fired in one atmosphere hydrogen at various temperatures showing a  $t^{1/3}$  dependence.

7.21 again retaining the one third time dependence of the particle size. However, as Figure 7.22 shows, at any time, the higher the alumina content, the smaller the particle size. Note the similarity in the shapes of the distributions. In Figure 7.23 are plotted the temperature dependencies of the rate of coarsening of both the pure and the alumina-doped ZnO. As can be easily seen, the alumina additions clearly retard particle growth. Even more significant however, is that the activation energy for grain growth in the alumina-doped materials is identical with that for the pure ZnO at lower temperatures, 109 kJ/mole (26 kcal/mole).

#### 7.4 Conclusions

Vapor transport in ZnO can indeed be enhanced by sintering in a reactive gas such as hydrogen which produces high vapor pressures of the product gas species. The enhancement of vapor transport leads to a decrease in sintering rate and densification as predicted by the sintering models. However, the major microstructural effect that is observed and which greatly affects the densification rate is rapid particle coarsening. The rate of coarsening increases with the hydrogen pressure and temperature and the particle size follows a one third time dependence as expected from classical coarsening models. However, the observed activation energy agrees with the classical models of Ostwald ripening only at the highest temperatures. At lower temperatures, a much higher activation energy is observed. As a result, it is postulated that the Greskovich-Lay<sup>15</sup> coarsening

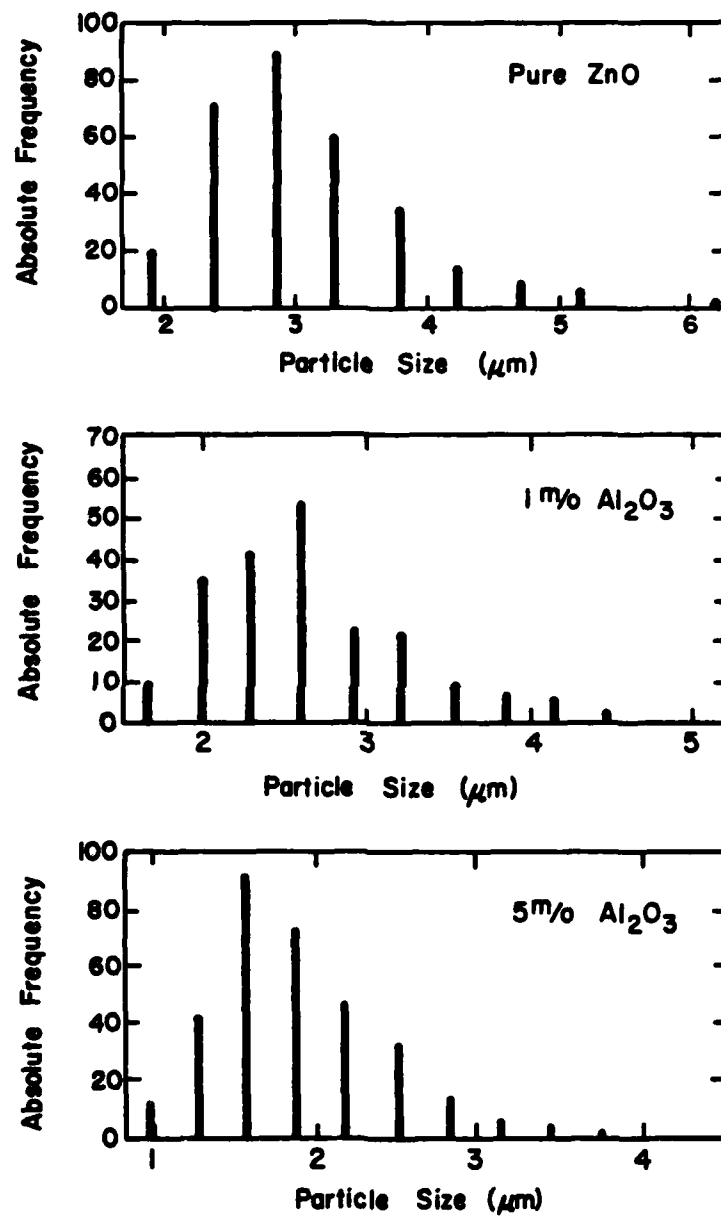


Figure 7.20 Particle size distributions of the 5 m/o Al<sub>2</sub>O<sub>3</sub> samples fired in pure hydrogen at 1150°C. Top: 30 minutes. Bottom: 120 minutes.

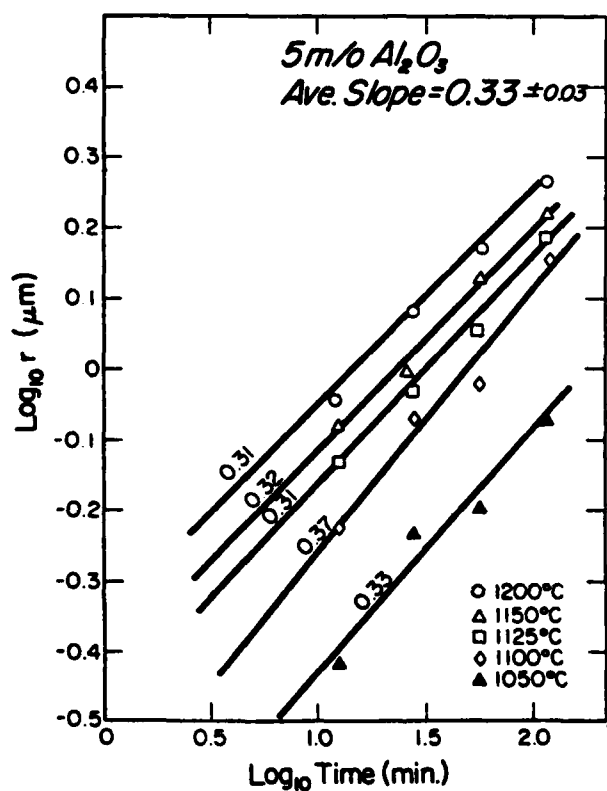


Figure 7.21 Log-log plot of the particle size versus time for the 5 m/o  $\text{Al}_2\text{O}_3$  samples fired in one atmosphere hydrogen at various temperatures showing a  $t^{1/3}$  dependence.

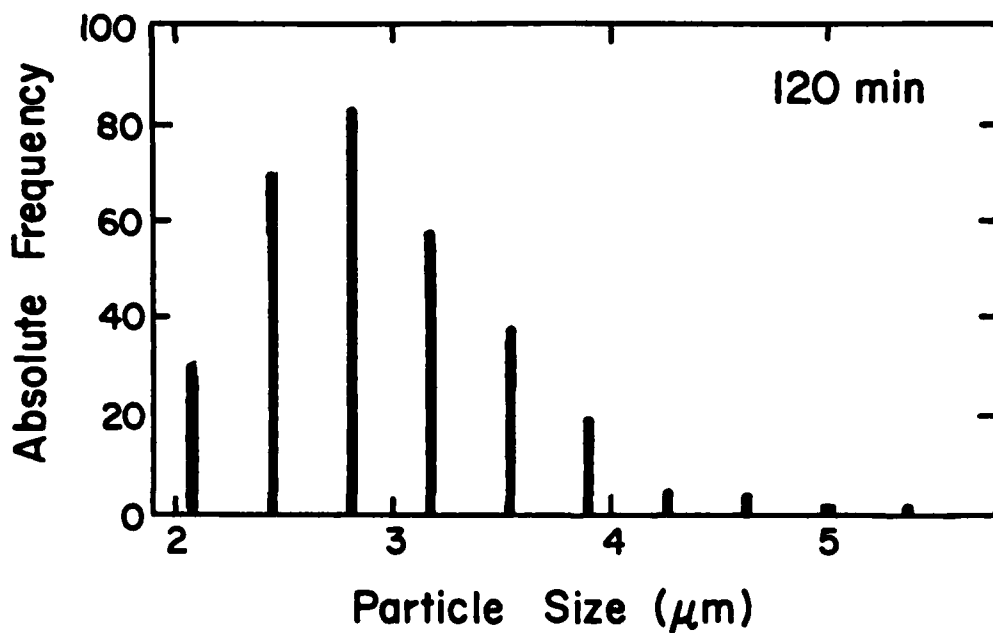
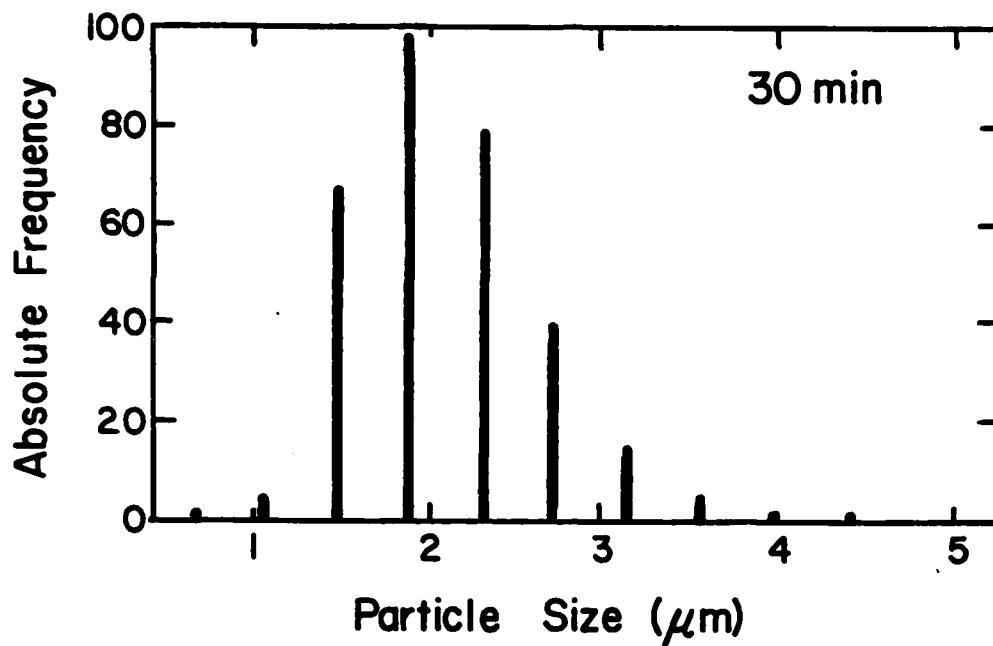


Figure 7.22 Comparison of the particle size distributions with varying additions of  $\text{Al}_2\text{O}_3$  fired at  $1150^\circ\text{C}$  for 60 minutes. Top: pure  $\text{ZnO}$ . Middle: 1.0 m/o  $\text{Al}_2\text{O}_3$ . Bottom: 5.0 m/o  $\text{Al}_2\text{O}_3$ .

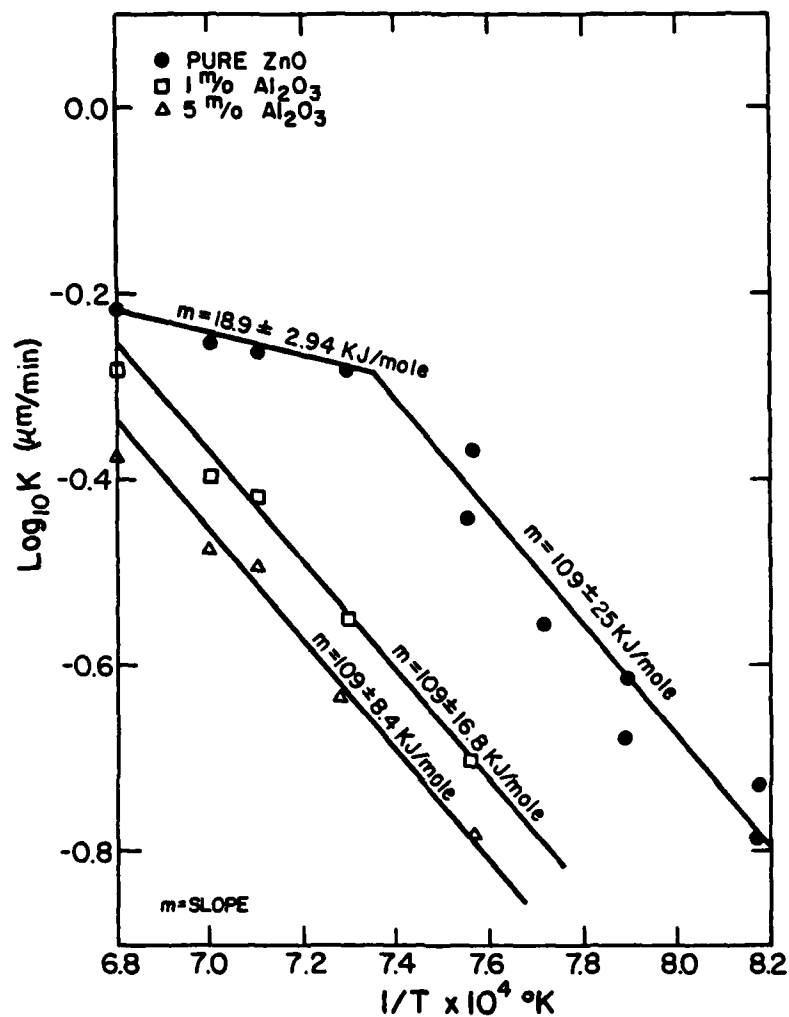


Figure 7.23 Temperature dependence of the rate of particle coarsening with different additions of Al<sub>2</sub>O<sub>3</sub> showing the lower rate with increasing alumina addition and the same activation energy as pure ZnO at the lower temperature at which grain boundary motion is thought to be rate controlling.



mechanism is operative with the rate of grain boundary motion controlling the coarsening rate. The activation energy for low temperature coarsening is very close to that obtained from grain growth data in air on dense samples. Furthermore, the addition of  $\text{ZnAl}_2\text{O}_4$  as a second phase decreases the rate of particle coarsening without changing the activation energy as expected if grain boundary motion were controlling the rate of particle coarsening. These results emphasize the importance of controlling grain growth not only during the final stages of sintering but also during the early stages so that the grain size-density plots will be such that a small grain size is obtained when the density becomes high to minimize secondary grain growth.

#### 7.5 References

1. D. R. Stull and H. Prophet, et al., JANAF Thermochemical Tables, 2nd edition, (U. S. Government Printing Office, Washington, D. C.), 1971.
2. D. W. Readey, et al., p. 387 in Advances in Materials Characterization, D. R. Rossington, R. A. Condrate, and R. L. Snyder, eds., (Plenum, N. Y.), 1983.
3. R. M. Barrer, Diffusion in and Through Solids, (Cambridge Univ. Press, Cambridge), p. 177, 1941.
4. G. C. Kuczynski, Trans. AIME 105 169 (1949).
5. W. D. Kingery and M. Berg, J. Appl. Phys. 26 1205 (1955).
6. G. W. Greenwood, Acta Met. 4 243 (1956).
7. I. M. Lifshitz and V. V. Slyozov, J. Phys. Chem. Solids 19 35 (1961).

8. C. Wagner, Z. Electrochem. 65 581 (1961).
9. T. K. Gupta and R. L. Coble, J. Am. Ceram. Soc. 51 521 (1968).
10. Y. Moriyoshi and W. Komatsu, J. Am. Ceram. Soc. 53 671 (1971).
11. R. M. Spriggs and S. Dutta, J. Am. Ceram. Soc. 53 61 (1970).
12. A. J. Ardell, Acta Met. 20 61 (1972).
13. C. K. L. Davies, P. Nash, and R. S. Steven, Acta Met. 28 179 (1980).
14. R. Watanabe and Y. Masuda, p. 83 in Sintering Processes, Vol. 13 in Materials Science Research, (Plenum, N. Y.), 1980.
15. C. Greskovich and K. W. Lay, J. Am. Ceram. Soc. 55 142 (1972).
16. E. M. Levin, C. R. Robbins, and H. F. McMurdie, Phase Diagrams for Ceramists, (Am. Ceramic Soc., Columbus), p.119, 1964.

## 8.0 MICROSTRUCTURE EVOLUTION IN $\text{SnO}_2$ AND $\text{CdO}$ IN REDUCING ATMOSPHERES

### 8.1 Introduction

In the research reported here, the microstructure evolution during the sintering of  $\text{CdO}$  and  $\text{SnO}_2$  powder compacts was studied with vapor transport enhanced in reducing atmospheres containing hydrogen.  $\text{CdO}$  and  $\text{SnO}_2$  were chosen for study because of the high vapor pressures which could be generated at relatively low temperatures thus ensuring the dominance of vapor transport over other mass transport processes.

### 8.2 Experimental

Relatively nonagglomerated reagent grade (Baker)  $\text{CdO}$  and  $\text{SnO}_2$  powders having average particle sizes on the order of a few tenths of a micrometer were pressed at 10,000 psi into pellets 1.4 cm in diameter. A green density of 61 percent of theoretical was obtained with  $\text{CdO}$  and 55 percent with  $\text{SnO}_2$ . The pellets were fired in air at temperatures below  $500^\circ\text{C}$  to provide some green strength. Pellets were placed into fused silica ampules which were then evacuated and dried until a dew point of  $-32^\circ\text{C}$  or less was achieved. The ampules were then filled with dry hydrogen at an appropriate pressure so that the pressure at the firing temperature would be in the neighborhood of one atmosphere. The pellets were fired for different times at various temperatures. After firing, samples were removed and their dimensions measured to determine shrinkage and their fracture surfaces examined by scanning electron microscopy.

Quantitative microstructure determinations were made with a semi-automatic image analyzer (Zeiss Videoplan). At least 60 particles or grains were measured for each data point and over 300 measured to obtain particle size distributions.

### 8.3 Results and Discussion

#### 8.3.1 Cadmium oxide

The densification rates of CdO in air and hydrogen are compared in Figure 8.1. Note that significant densification was observed in air at 700°C while no shrinkage occurred in hydrogen. It might be noted that densification was observed as low as 300°C in air. Results at other temperatures were similar except that at the highest temperatures studied, some densification occurred even in the pure hydrogen atmosphere. As can be seen in Figure 8.2 the reason that densification does not occur in hydrogen is due to particle coarsening similar to that observed for ZnO in hydrogen and Fe<sub>2</sub>O<sub>3</sub> in HCl presented earlier in this report. Figure 8.3 demonstrates that the particle or grain size follows a time to the one third power dependence as observed in the other systems studied. This is predicted by the classical Ostwald ripening models of coarsening by diffusion through the surrounding fluid phase<sup>1,2,3</sup>, namely:

$$\bar{r}^3 = \frac{8 D \gamma \bar{v}^2}{9 (RT)^2} P_0 t$$

for diffusion and for an interface controlled reaction:

$$\bar{r}^2 = \left(\frac{8}{9}\right)^2 \frac{K \gamma \bar{v}^2}{(RT)^2} P_0 t$$

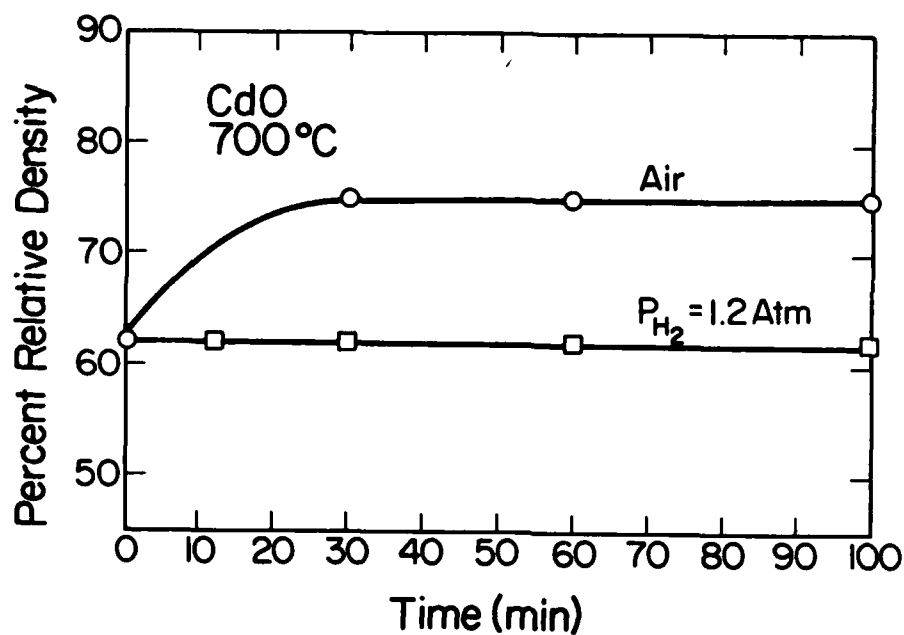


Figure 8.1 Density versus time for CdO fired in air and hydrogen.



Figure 8.2 CdO fired at 700°C for 100 minutes in air(left) and hydrogen(right).

where  $\bar{r}$  = average particle radius  
 $K$  = surface reaction rate constant  
 $\bar{v}$  = molar volume  
 $D$  = gaseous diffusion coefficient  
 $R$  = gas constant  
 $T$  = temperature  
 $p_0$  = equilibrium partial pressure.

In the above equation for Ostwald ripening by diffusion, the only exponentially temperature dependent term is the equilibrium partial pressure of the diffusing gaseous species. The reaction of importance for CdO in  $H_2$  is:



which gives for the equilibrium constant,  $K_e$ :

$$K_e = \frac{p(Cd) p(H_2O)}{p(H_2)}$$

If the ambient hydrogen gas is very dry, as it is believed to be in these experiments, then the only water vapor in the system is a product of the reaction so  $p(H_2O) \approx p(Cd)$ . This leads to the following temperature dependence of the equilibrium partial pressure of the diffusing gaseous species:

$$p_0 = p(Cd) \approx p(H_2O) \sim K_e^{1/2} \sim \exp(-\Delta H^0/2RT)$$

where  $\Delta H^0$  is the standard enthalpy for the above reaction. On the other hand, if the ambient water vapor pressure in the system were much larger than that produced from the reaction, then  $p(H_2O) \gg p(Cd)$  and,

$$p_0 = p(Cd) \sim K_e \sim \exp(-\Delta H^0/RT).$$

From above, the rate of particle coarsening can be written as:

$$r = Kt^{1/3}.$$

Since  $K \sim p_0^{1/3}$ , if the log of the intercepts in Figure 8.3 are

plotted versus  $1/T$ , the apparent activation energies are  $\Delta H^0/6$  and  $\Delta H^0/3$  for the low and high ambient water vapor pressures. Figure 8.4 shows the temperature dependence of the rate of coarsening with an apparent activation energy on 8 kilocal/mole. The standard enthalpy for the reduction of CdO in  $H_2$  is 5 kilocal/mole<sup>4</sup>. Thus the observed activation energy is much larger than is predicted by the gaseous diffusion model of coarsening. These results are similar to those obtained in other the systems studied which have been explained by the Greskovich-Lay model of particle coarsening in porous compacts<sup>5</sup>. The major mass transport is by gaseous diffusion, but the actual rate control is by migration of the grain boundary. Unfortunately, there are no grain growth data for CdO available in the literature with which to compare the observed activation energy for grain growth obtained here.

Furthermore, as Figure 8.5 shows, the measured particle or grain size distributions are strongly skewed to large particles which is just the opposite to the predictions of the classical Ostwald ripening models<sup>1,2,3</sup>. These results are again similar to those observed with ZnO and  $Fe_2O_3$  and give further support to the postulate of grain boundary migration rather than gaseous diffusion being the rate controlling step in the coarsening process.

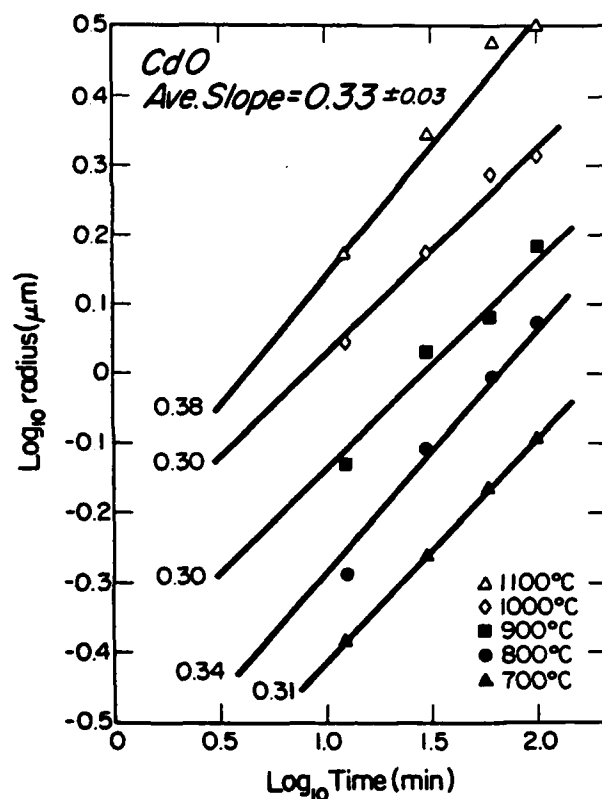


Figure 8.3 Particle radius versus time for CdO fired in hydrogen.

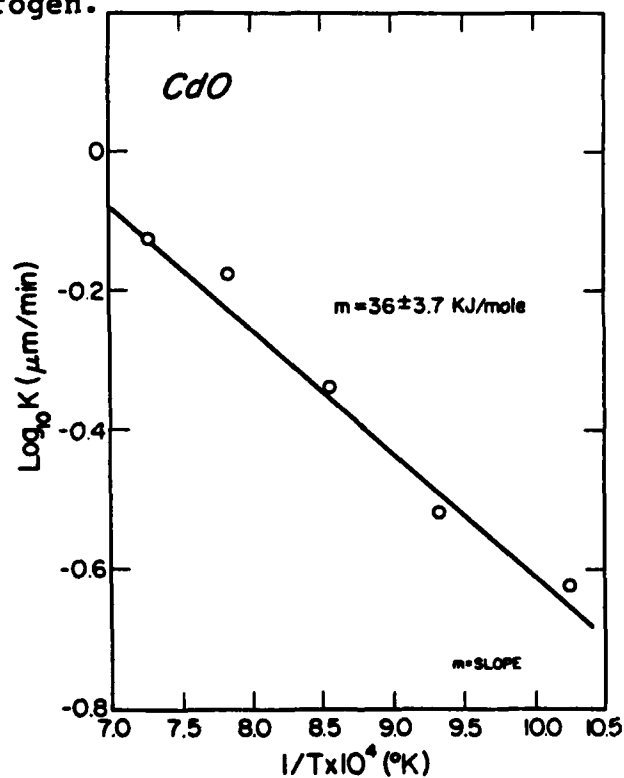


Figure 8.4 Temperature dependence of the rate of coarsening for CdO fired in hydrogen.



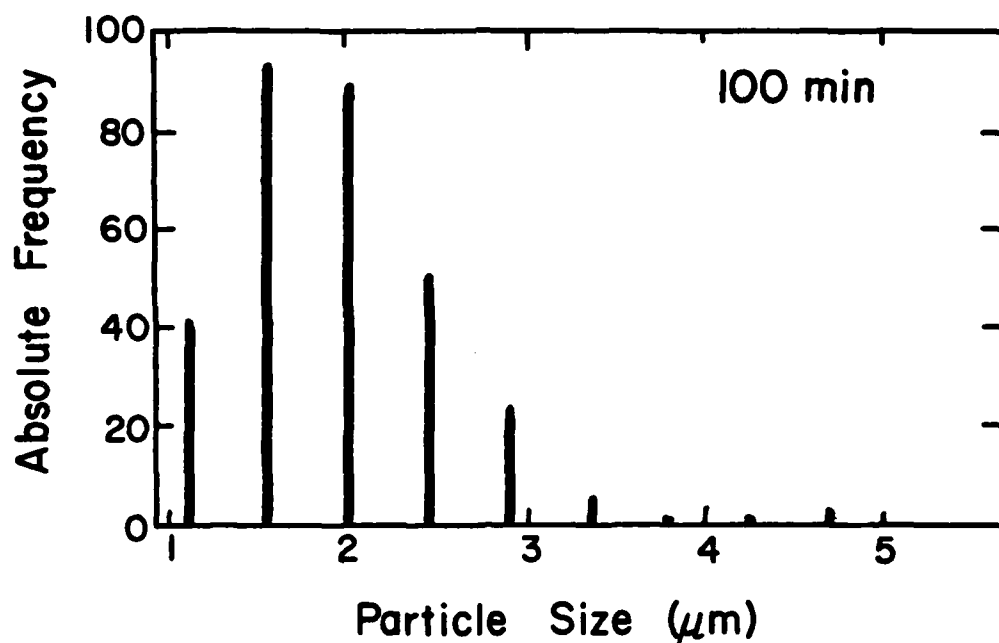


Figure 8.5 Particle diameter distribution (micrometers) for CdO fired at 700°C for 100 minutes in hydrogen.

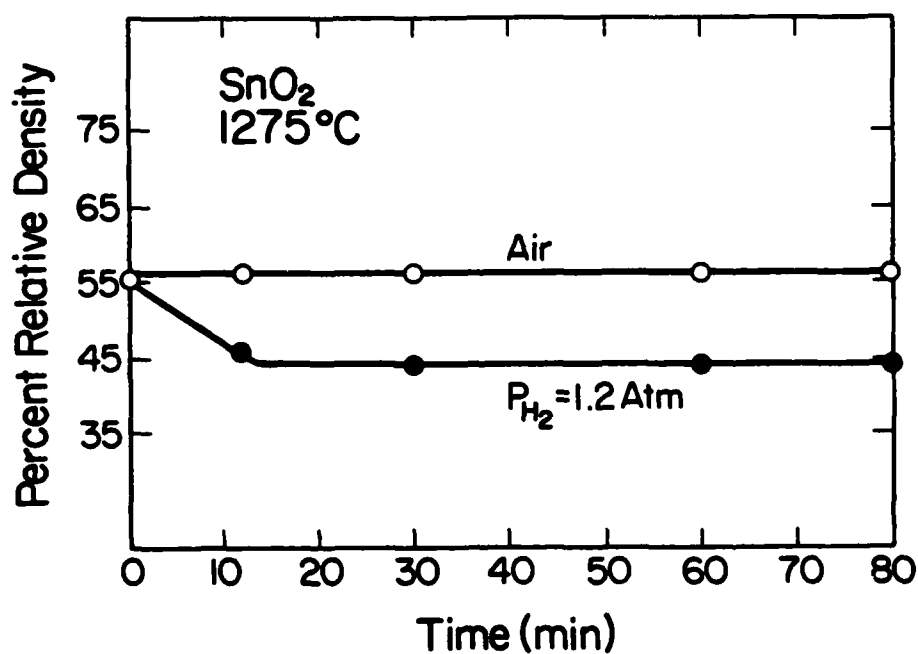


Figure 8.6 Density versus time for SnO<sub>2</sub> fired in air and hydrogen.

### 8.3.2 Tin oxide

The  $\text{SnO}_2$  exhibited rather unusual behavior in that even in air no shrinkage was observed over the temperature range studied while in pure hydrogen the samples actually expanded as shown in Figure 8.6. Again, the major microstructural effect of the enhanced vapor transport was particle coarsening as can be seen in Figure 8.7. Also, the  $\text{SnO}_2$  particles exhibited a great deal of faceting even at the highest temperatures studied. That the  $\text{SnO}_2$  expands might be explained by the fact that the particle growth or coarsening is probably not isotropic since tin oxide is tetragonal. As a result, the particles become somewhat elongated leading to expansion.

Figure 8.8 demonstrates that the  $\text{SnO}_2$  grains also grow as the one third power of time as predicted by the Ostwald ripening models<sup>1,2,3</sup>. In this case, the reaction is thought to be<sup>6</sup>:



As in the case of  $\text{CdO}$ , since there are only the two product gases the same considerations hold, namely:

$$p_{\text{O}} = p(\text{SnO}) \cong p(\text{H}_2\text{O}) \sim K_e^{1/2} \sim \exp(-\Delta H^\circ/2RT)$$

in very dry hydrogen and,

$$p_{\text{O}} = p(\text{SnO}) \sim K_e \sim \exp(-\Delta H^\circ/RT)$$

in wet hydrogen. Again,  $\Delta H^\circ$  is the standard enthalpy for the reaction which in this case is 43 kilocal/mole<sup>4</sup>. The expected apparent activation energy of the rate of coarsening for this system should likewise be  $\Delta H^\circ/6$  or  $\Delta H^\circ/3$  for dry and wet

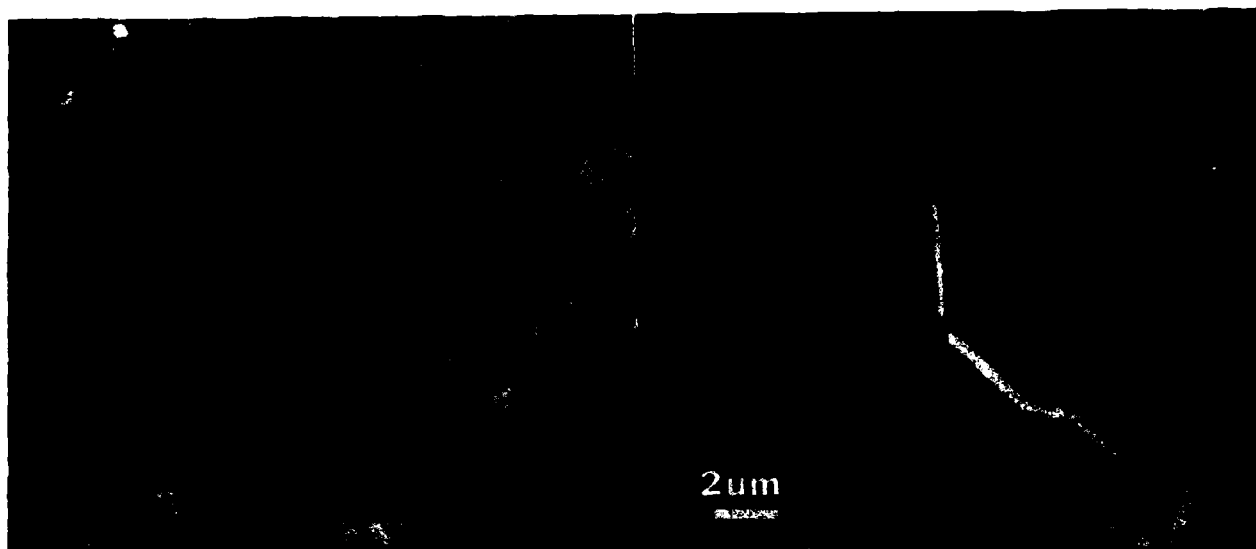


Figure 8.7 SnO<sub>2</sub> fired at 1275°C for 80 minutes in air (left) and hydrogen (right).

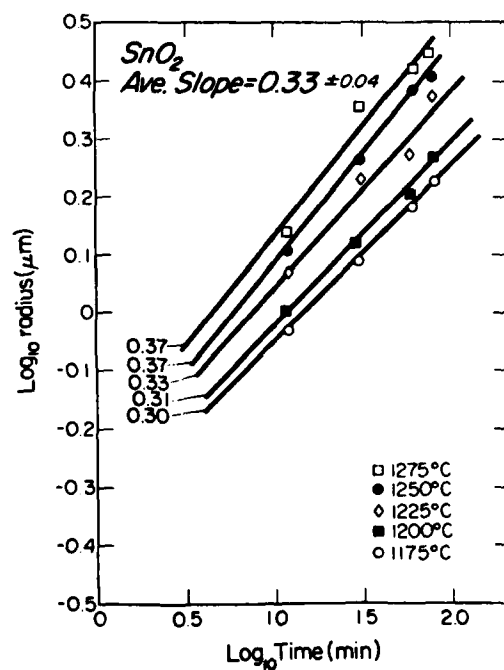


Figure 8.8 Particle radius versus time for SnO<sub>2</sub> fired in hydrogen.

hydrogen respectively. From the data in Figure 8.9, an apparent activation energy of 10 kilocal/mole is obtained which lies directly between the two expected activation energies. Thus, in this case it is more difficult to conclude that the rate of coarsening is not controlled by gaseous diffusion but rather by grain boundary migration. In fact, the particle size distributions observed for the  $\text{SnO}_2$  do not seem to be as strongly skewed to the larger particle sizes as in the case of  $\text{CdO}$  as seen in Figure 8.10. However, the particle size distributions still do not fit those expected from the Ostwald ripening models. There have been modifications of these models for the case when the volume fraction of the growing particles is large<sup>7,8</sup> which do lead to distributions more similar to those commonly observed in other systems exhibiting coarsening<sup>9</sup>. However, these models do not completely explain the observed distributions and are not even valid when the coarsening particles are in contact as they are in a powder compact. Thus, the rate-controlling step in the case of  $\text{SnO}_2$  is perhaps somewhat more uncertain than in the case of  $\text{CdO}$ .

#### 8.4 Conclusions

Enhanced vapor transport in the  $\text{CdO-H}_2$  and  $\text{SnO}_2\text{-H}_2$  systems leads to reduced shrinkage and exaggerated particle coarsening as in the  $\text{ZnO-H}_2$  and  $\text{Fe}_2\text{O}_3\text{-HCl}$  systems. In the case of  $\text{SnO}_2$ , the powder compacts actually expand which could be due to nonisotropic particle growth. Also, as observed in the other systems, the particles coarsen as the one third power of time

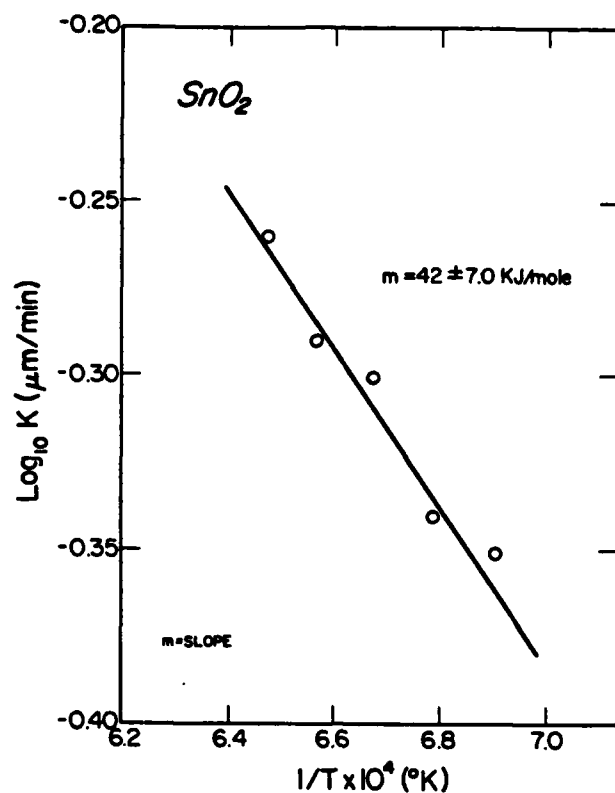


Figure 8.9 Temperature dependence of the rate of coarsening of  $\text{SnO}_2$  fired in hydrogen.

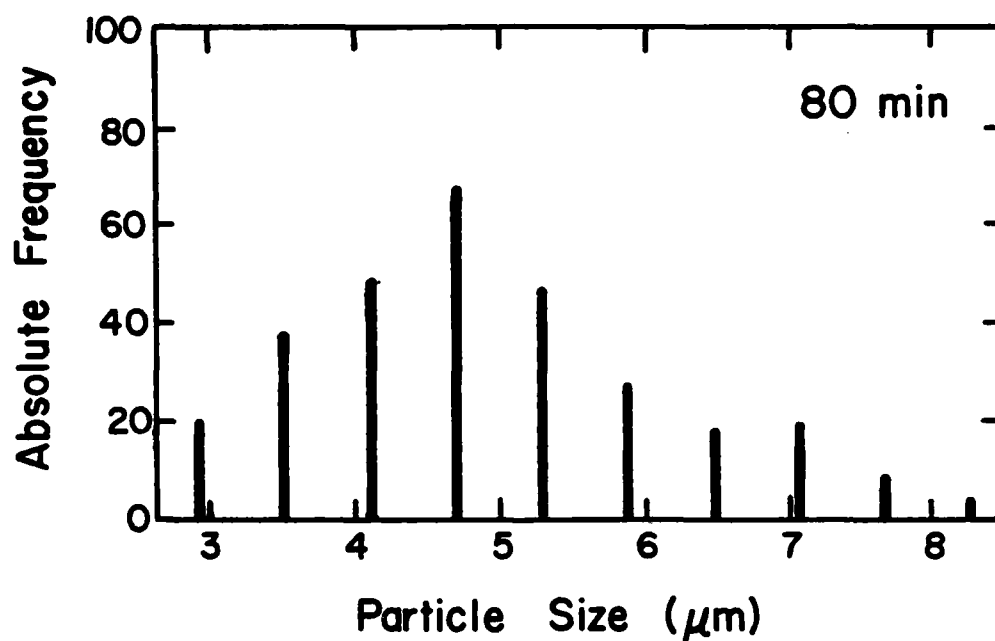


Figure 8.10 Particle diameter, micrometers, distribution for  $\text{SnO}_2$  fired at  $1275^\circ\text{C}$  for 60 minutes in hydrogen.

following time dependence for the classical Ostwald ripening models of particle growth controlled by diffusion through the surrounding fluid phase. However, neither do the particle size distributions fit the models nor do the observed activation energies, particularly for CdO. Unfortunately, really no quantitative coarsening model exists for the case in which the particles or grains are in contact as they are in a powder compact. However, given the generally larger activation energy observed than expected, it is tentatively concluded that the Greskovich-Lay<sup>5</sup> model is operative in CdO. That is, the rate of grain boundary migration is controlling the rate of grain or particle coarsening. For SnO<sub>2</sub>, the evidence is less convincing.

#### 8.5 References

1. G. W. Greenwood, *Acta Met.* 4 243 (1956).
2. I. M. Lifshitz and V. V. Slyozov, *J. Phys. Chem. Solids* 19 35 (1961).
3. C. Wagner, *Z. Electrochem.* 65 581 (1961).
4. O. Kubaschewski and C. B. Alcock, Metallurgical Thermochemistry, 5th ed., (Pergamon, N. Y.) p. 267, 1979.
5. C. Greskovich and K. W. Lay, *J. Am. Ceram. Soc.* 55 142 (1972).
6. H. H. Kellogg, *Trans AIME* 236 602 (1966)
7. A. J. Ardell, *Acta Met.* 20 61 (1972).
8. C. K. L. Davies, et al., *Acta Met.* 28 179 (1980).
9. Y. Masuda and R. Watanabe, p. 3 in Vol. 13 of *Materials Science Research, Sintering Processes*, (Plenum, N. Y.), 1980.

**END**

**FILMED**

**10-84**

**DTIC**